COEXISTENCE OF BOGOLIUBOV QUASIPARTICLES AND ELECTRONIC CLUSTER DOMAINS IN LIGHTLY HOLE-DOPED CUPRATE SUPERCONDUCTORS

A Dissertation

Presented to the Faculty of the Graduate School

of Cornell University

in Partial Fulfillment of the Requirements for the Degree of

Doctor of Philosophy

by

Curry Bachman Taylor

January 2008

COEXISTENCE OF BOGOLIUBOV QUASIPARTICLES AND ELECTRONIC CLUSTER DOMAINS IN LIGHTLY HOLE-DOPED CUPRATE SUPERCONDUCTORS

Curry Bachman Taylor, Ph.D.

Cornell University 2008

It is only now becoming clear that scanning tunneling microscopy and spectroscopy serve a vital purpose in probing not only the electronic structure of quantum mechanical states in real space, but also in momentum space. In studies of the underdoped high-T_C cuprate superconductors, spectroscopy reveals two energetic gap-like features. The investigations described in this dissertation reveal that the higher energy spectral feature contributes to a disordered glass of electronic domains. These objects break long-range translational and rotational symmetry, but are nevertheless ordered on the atomic scale, consisting internally of bond-centered Cu-O-Cu objects. Such features were discovered in two lightly hole-doped cuprate compounds, $Bi_2Sr_2Dy_xCa_{1-x}Cu_2O_{8+\delta}$ and $Ca_{2-x}Na_xCuO_2Cl_2$, which share no common lattice chemistry except for at least one CuO_2 plane. Furthermore, it is possible to utilize Bogoliubov quasiparticle interference to probe the spectral weight of cuprate samples in $\vec{k}$-space. These calculations produce the so-called "bananas", or Fermi arcs, at low ($\sim$6-30mV) energies. The octet model of quasiparticle scattering analysis reveals energetic dispersion which increases in intensity as doping is decreased from optimal percentages. In addition, fits to a model for the angular dependence of a d-wave order parameter suggest a relationship between the higher-energy gap and the model parameters found via quasiparticle interference. Disappearance of quasiparticle intensity occurs quite near a $\sqrt{2} \times \sqrt{2}$ zone boundary, a curious observation considering that the samples studied are not antiferromagnets per se. Since low-energy Bogoliubov states are well-defined in $\vec{k}$-space

and the higher-energy electronic domain glass states are well-defined in $\vec{r}$-space, an energetic phase separation of two types of quantum eigenstate are proposed. Further, the growth of spectral gaps from the optimally doped to the underdoped regimes suggests that the disordered patterns of the electronic domain glass measured via tunneling asymmetry studies are actually real-space measurements of the electronic excitations within the pseudogap regime. This picture eludes to a d-wave superconductor which, with falling doping, relents its superconducting order to quasiparticle scattering within the pseudogap domain, while the pseudogap order splits away and gradually concedes to the antiferromagnetic Mott insulator parent state.

BIOGRAPHICAL SKETCH

Curry Taylor was born and raised in Cleburne, Texas. He attended Cleburne High School (CHS), graduating third in his class. He attended Southern Methodist University (SMU) in Dallas, Texas as an undergraduate for several years, studying electrical engineering, computer engineering, physics, computer science, and mathematics. At this time, he also took employment with Hewlett-Packard as a Co-Op student and computer engineer. Curry later transferred to the University of Illinois at Urbana-Champaign (UIUC) and graduated from there in 2002 with a bachelor's of science (B.S.) in electrical engineering, a B.S. in engineering physics, and minors in mathematics and computer science.

Curry then joined the physics department at Cornell University as a graduate student in condensed matter physics. His first year, he took graduate coursework in physics and taught an undergraduate course, an introduction to classical mechanics and motion for engineers, as a teaching assistant (TA). He then joined the laboratory of Dr. J. C. "Séamus" Davis to investigate the microscopic, quantum mechanical theory of high-T_C superconductivity. Since that time, Curry has performed experiments using a highly sensitive, low-noise scanning tunneling microscope (STM), and has performed a wide variety of numerical and mathematical analyses on acquired research data.

Curry is musically inclined, having played trombone for over a decade in high school and university marching bands, jazz ensembles, wind ensembles, and concert bands, and serving as drum major for three years in high school. He holds an extra class amateur radio license with the FCC and is an active ham radio operator. Curry also has strong interests in philosophy, politics, and economics, and is a liberty-oriented individual.

Dedicated to the future. May it be brighter than today.

ACKNOWLEDGEMENTS

First and foremost, I would like to thank my advisor, Dr. J. C. "Séamus" Davis, whose tireless enthusiasm and dedication to understanding nature proved extraordinarily contagious. Dr. Erich Mueller spent countless hours helping me to understand second-quantized Bogoliubov de Gennes computations and other condensed matter tricks. I also thank Dr. Rob Thorne for his moral support and positive reinforcement of my work. I further acknowledge Dr. Ali Yazdani, Dr. Richard Martin, and Dr. Keh-Yung Cheng at UIUC for the opportunities to work and learn in their laboratories as an undergraduate.

I would also like to thank my fellow colleagues and researchers at Cornell and other places around the world. The postdocs sharing my project were indispensable: I thank Dr. Christian Lupien, Dr. Yuhki Kohsaka, and Dr. Peter Wahl; for our very lengthy discussions about physics, technical details about our and other experiments, and for their confident ability to answer all kinds of questions. Other postdocs who aided me were Dr. Jhinhwan Lee, Dr. Kyle McElroy, and Dr. Jinho Lee. Dr. Tetsuo Hanaguri, a visiting Professor from RIKEN, also gave me good advice. And of course, I thank the fellow graduate students who worked with me closely on STM research in the Davis group: Andrew Schmidt, Jacob Alldredge, and Alfred Wang.

I would like to thank the following researchers, who preceded me, for their useful work which enabled much of the research performed during my graduate tenure: Dr. Eric Hudson, Dr. Ray Simmonds, Dr. Kyle McElroy, Dr. Jenny Hoffman, Dr. Kristine Lang, and Dr. S. H. Pan. Of course, scanning tunneling microscopy research itself would not be possible without its development by Binnig and Rohrer at IBM in Zürich, Switzerland, and the discovery of high-T_C superconductivity by Bednorz and Müller, also at IBM, Zurich.

I would like to thank the Laboratory of Atomic and Solid State Physics (LASSP) and the Physics Department itself for the opportunity to come to a unique and rich environment in which to study physics, and Cornell University as a whole for its aggressive role in research of all kinds. I would like to thank all of my lecture professors for my very challenging graduate physics courses, and the 2002-2003 teaching staff of PHYS 112: "Introductory Mechanics for Engineers" for familiarizing me, as a teaching assistant, with the taxing role of an educator.

There are many supporting groups and individuals in Ithaca who were essential to the creation of this dissertation. The Cornell Center for Materials Research (CCMR) is a well-staffed and well-stocked location beneath Clark Hall to perform physics research. In particular, the machine shop staff is extremely talented and indispensable. I would like to thank Stan Carpenter, shop manager, and all the machinists who worked with me in the professional or graduate machine shops: Bob Snedeker, Nathan Ellis, Chris Cowulich, Stan McFall, Jeff Koski, and Rodney Bowman. Not only did these people create amazing things I could use in my experiments, but they also taught me how to create amazing things on my own. Dr. Eric Smith, the veteran Cornell graduate and ^4He helium liquifier guru, also provided invaluable expertise in cryostat operation, helium processing, and general experiment design practices. I also recognize Nick Brown, who happily toiled over all of our myriad orders, finances, and special accounting needs over the years.

And finally, of course, I would like to thank my parents, Jan and Dan Taylor, who have supported me in a great number of ways in my life no matter which path I have chosen to take at any given moment. I thank my brother, Zach Taylor, for our stress-relieving conversations during my graduate study, and Marielle Newsome, my girlfriend, for her companionship.

The following taxpayer-funded grant sources provided the funding used to support this experimental research: The Office of Naval Research (ONR); Cornell University; The Department of Energy (DOE); Institute for Complex Adaptive Matter (I2CAM); Japan Society for the Promotion of Science (JSPS); and The Army Research Office (ARO).

The following companies sold us essential instruments or provided technical support for products which were used in preparation of this experimental research: Oxford Instruments; Kadel Engineering Corporation; ETS-Lindgren; Standford Research Systems; Axiden Instruments; Metal Flex Welded Bellows, Inc.; Adixen by Alcatel Vacuum Technology; Hewlett-Packard Corporation; Airgas; McMaster-Carr; Fischer Scientific.

The following software packages and instruments were used in operations or analysis related to this research, or in preparation of this dissertation: National Instruments LabView 7.1; gnuplot v4.2 patchlevel 2; ActivePerl v5.8.7; MiKTeX v2.4; LaTeX2e; WinEdt v5.5; Mathematica v5.1 for Students; IDL v6.0; TI-83 and TI-85 calculators; SolidWorks 2006-2007 Student Edition; AutoCAD 2000; Ghostscript v8.14; GSview v4.8; FireFox v2.0; XML; and javascript.

TABLE OF CONTENTS

LIST OF FIGURES

LIST OF TABLES

Chapter 1
Scanning Tunneling Microscopy: Theoretical and Experimental Basics

Although the scanning tunneling microscope (STM) was developed over 25 years ago at IBM, Zürich by Binnig and Rohrer,[3] to date, it remains unmatched for the investigation of atomic-scale lattice and electronic phenomena in real-space. In addition, the technique has expanded to include different types of automated spectroscopic measurement and analyses which now, as is the aim of this dissertation to convince the reader, provide considerable precision in quasimomentum space. I have little doubt that the STM will continue to serve as an essential tool for material investigation in the future, and its uses will continue to branch into multidisciplinary fields, perhaps including the hard sciences, engineering, biology, and medicine. In this chapter I review, with some modifications, what an STM junction actually measures.

1.1 Model of Tunneling

The model of tunneling commonly used in scanning tunneling microscopy (STM) research stems from embellishments made to the original formulation of Bardeen[2] in combination with ideas from Tersoff[9–13] and others. With a few modifications and additions, this is the precedent I have followed, similarly to other colleagues.[6]

We may calculate the total current which will flow between two Fermi metals (e.g. the tip and a sample) due to tunneling by determining what the contributions to the current will be for particles and anti-particles tunneling from the first to the second metal, and vice-versa. Suppose that we have two such Fermi metals, labeled 1 and 2, each with its own distinct Fermi level, E_{F1} and E_{F2}, respectively. The

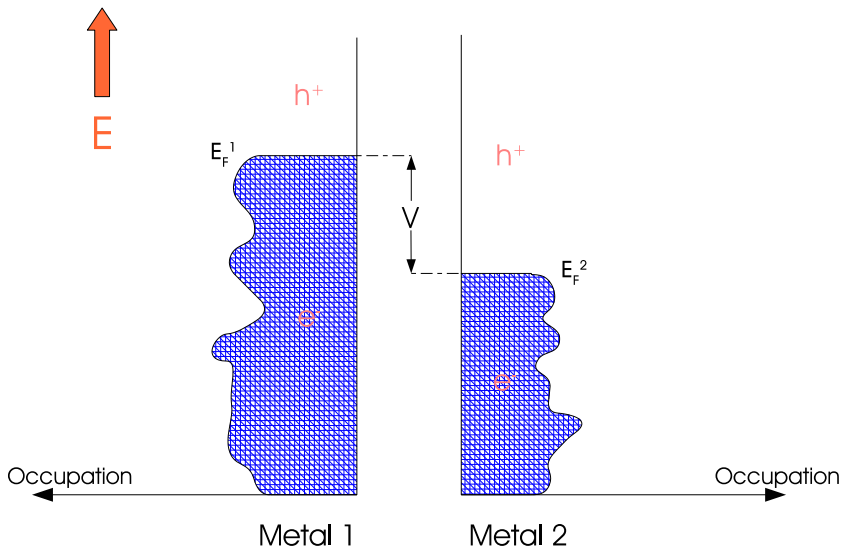

Figure 1.1: The densities of state of two metals separated by a vacuum through which electrons may tunnel. A bias voltage is applied, which raises the Fermi energy of Metal 1 (E_{F1}) with respect to the Fermi energy of Metal 2 (E_{F2}).

Fermi level denotes the boundary in energy between filled (particle) and unfilled (antiparticle) energy states. As long as the two systems are independent, one may measure the energies in each metal relative to their respective Fermi energies. This is a convenient point of reference because particles and antiparticles will then be found in states with positive (+) or negative (-) energy, respectively. Further suppose that the two metals are held at a constant potential difference with respect to each other and that the potential of metal 1 is higher than that of metal 2 (see Figure 1.1). With this convention, any current flowing from metal 1 to metal 2 will be positive, and any current flowing from metal 2 to metal 1 will be negative. More explicitly, the total tunneling current will be

$$I = I_{1\to 2} \; - \; I_{2\to 1} \tag{1.1}$$

In order for a current to flow from metal 1 to metal 2, there must be a supply of electrons (or holes, depending the prior chosen sign convention for the potential difference) in metal 1 but a supply of holes (electrons) in metal 2. The sign

convention chosen above for current flow (+ or -) does not matter because the final result for the total current will be modified only by an overall minus sign if the convention is chosen oppositely.

For a particular energy (E), the number of electrons present in a given metal will be given by the density of states (ρ) of that metal at the energy of interest weighted by the Fermi function ($f = (e^{\beta(E-E_F)} + 1)^{-1}$) at that energy. ρ gives the number of states available owing to electronic structure, but Fermi statistics dictates that not all of those states will be filled. The density of filled states in a metal at energy E is

$$n_e(E) = f(E)\rho(E) \tag{1.2}$$

This combination of factors represents the electron population at energy E, keeping in mind that $\rho(E)$ is a *continuous distribution* which should be integrated over to make statistical, quantitative sense. The above expression, however, accounts only for the electrons at energy E which can take part in conduction; we must also think about the *holes* at energy E which may also take part in conduction. The fraction of holes (also fermions) which are filled at a particular energy (E) is $1 - f(E)$. Thus, correspondingly to Equation 1.2 above, the number of empty states (holes) in a metal at energy E is

$$n_h(E) = (1 - f(E))\rho(E) \tag{1.3}$$

Now we must ask, what is the total number of carriers which contribute to a steady current from metal 1 to metal 2? First, we must choose a "global" reference energy E via which we can refer to the corresponding energies in both metals. This is done by choosing a level for $E = 0$. The zero energy can be chosen anywhere because we are interested only in relative energies. However, I choose $E = 0$ at the Fermi level of metal 2, because I believe the resulting mathematics is nicer,

and also because metal 2 will later represent an STM tip which is connected to a virtual ground (see Section 2.1.1). This means that the "global" energy scale E and the independent energy scale of metal 2 are one in the same if E_{F2} is defined to be zero, according to my choice.

With this choice, one may approximate the current flowing due to particles (electrons) flowing from occupied states in metal 1 to empty states in metal 2 is given by

$$I_{1\to 2} = \frac{4\pi e}{\hbar}\int_{-\infty}^{\infty} |M|^2 \Big[\rho_1(E-eV)f(E-eV)\Big]\Big[\rho_2(E)\big(1-f(E)\big)\Big]dE \qquad (1.4)$$

where the first term in brackets is the density of electrons $n_e(E)$ in metal 1 and the second term in brackets is the density of holes $n_h(E)$ in metal 2. We integrate our occupation density from $-\infty$ to ∞ to obtain the total current over all defined energies. Notice that the first term in brackets ([]) is offset by eV, the energy corresponding to the potential difference V, so that it will conform to our "global" energy choice E. The second bracketed term, which represents hole occupation in metal 2, requires no such adjustment because we chose $E = 0$ at the Fermi level for metal 2. Fur

The additional factor $\frac{4\pi e}{\hbar}$ comes from Fermi's Golden Rule. A more sophisticated analysis would produce this factor. In actuality, such a rigorous tunneling calculation takes a quantum mechanical form involving the probabilities, or rates, of tunneling from all occupied quantum states in metal 1 to all occupied quantum states in metal 2. Each tunneling rate is represented by a matrix element, which have cofactors which are collectively indicated in Equation 1.4 by the factor $|M|^2$. In general, the full many-body calculation of quantum tunneling is an intractable problem, due to unknown variables and dependencies in the matrix element factors M and the geometrical particularities of the tunnel junction. However, several very good approximations can be made using many-body statistics and Green's

functions for geometrical considerations to arrive at a form like Equation 1.4.[1, 4, 8]

In addition, there also exists a current from the flow of the hole states in metal 2 to the occupied states in metal 1. Note that this is a descriptive process only, and in modern quantum physical formulations, holes do not actually move through a vacuum to arrive in another metal. It is actually the electrons themselves which cause the effect of the empty states and the resulting current contributions. However, for all mathematical purposes, the holes act as if they are moving just like electrons, but with a charge of +e (and thus a transport flow in the opposite direction as that of the electrons). Then, the contribution of the hole "motion" to the current is, analogously to the above,

$$I_{2\to 1} = \frac{4\pi e}{\hbar}\int_{-\infty}^{\infty} |M|^2 \Big[\rho_1(E-eV)\big(1-f(E-eV)\big)\Big]\Big[\rho_2(E)f(E)\Big]dE \qquad (1.5)$$

Combining these two currents (with a minus sign for the opposing hole flow), we obtain a total current of

$$\begin{aligned} I &= I_{1\to 2} \; - \; I_{2\to 1} \\ &= \frac{4\pi e}{\hbar}\int_{-\infty}^{\infty} |M|^2 \Big[\rho_1(E-eV)f(E-eV)\rho_2(E)\big(1-f(E)\big) \\ &\quad - \rho_1(E-eV)\big(1-f(E-eV)\big)\rho_2(E)f(E)\Big]dE \end{aligned} \qquad (1.6)$$

After distributing the Fermi function terms in the above with multiplication, two of the terms cancel. The remaining expression is

$$I = \frac{4\pi e}{\hbar}\int_{-\infty}^{\infty} |M|^2 \rho_1(E-eV)\rho_2(E)\Big[f(E-eV)-f(E)\Big]dE \qquad (1.7)$$

Note once again that the location of eV, and the relative signs in front of both eV and the Fermi functions, depend on my original choice for $E = 0$. Now, the populations of fermions in each metal will be affected by both the energy relative to the Fermi level (E_F) and the temperature (T). The experiments to be described in this dissertation were carried out at 4.2 Kelvin, liquid helium temperatures, or

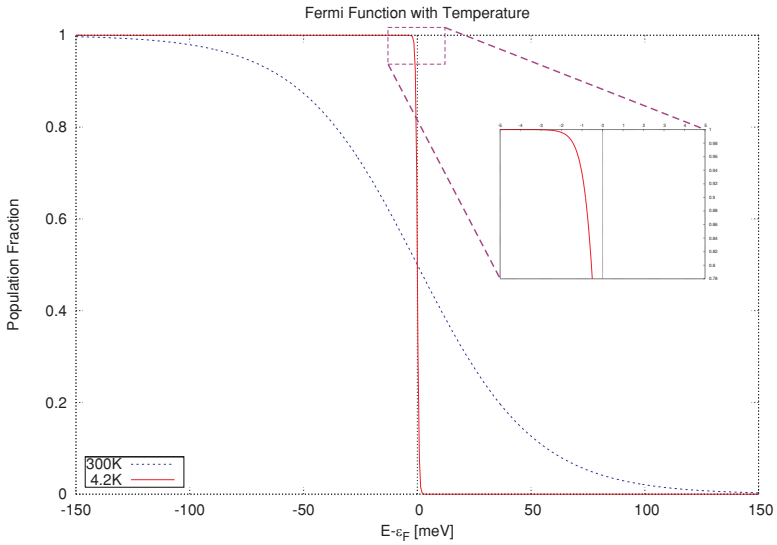

Figure 1.2: Fermi Population for Room and LHe Bath Temperatures. The inset shows that the approximation $f(E) \approx \Theta(-E)$ is very good for energies 3meV above or below the Fermi energy at LHe temperature.

lower, for a variety of reasons. One of these reasons is to allow a distinct separation between particle and hole states across E_F. In Fig. 1.2, it can be seen that the Fermi population of available states is quite sharp about E_F at 4.2K (and at lower temperatures). In the energy range of interest for an experiment (3meV→1eV on either side of the Fermi level), states will have either an extremely high probability or an extremely low probability of being filled, with little mixing between the two.

Noting this narrow behavior at low temperatures, I make an assumption to consider the Fermi Function at experimental temperatures as a Heaviside unit step function ($f(E) \approx \Theta(-E)$). Hence, the infinite integral bounds in Equation 1.7 are truncated, resulting in an integration over only a finite interval:

$$I = \frac{4\pi e}{\hbar} \int_0^{eV} |M|^2 \, \rho_1(E - eV)\rho_2(E) dE \tag{1.8}$$

This derivation assumes that metal 1 and metal 2 can be treated as two separate systems with mostly independent densities of states that weakly overlap. Further, it is also assumed that tunneling is an elastic process (i.e. that energy is conserved

during tunneling).

We may further assume a form for the matrix elements $|M|^2$. We model M as quantum mechanical tunneling through an energy barrier of height ϕ and width z. If $V \ll \phi$, where ϕ is the "convoluted workfunction" of the tip and sample, then we can presume the matrix elements to be independent of energy (E). In such a case, we can write

$$|M|^2 \propto exp(-2\frac{\sqrt{2m\phi}}{\hbar}z(V)) \tag{1.9}$$

where z in this case is the separation of the tip to the sample, and m is the mass of a single (tunneling) electron. Notice that $|M|^2$ is still dependent, in general, on bias V through its z dependence. The approximation that $V \ll \phi$ limits the applicability of the explicit $|M|^2$ dependence of the tunneling equation to lower biases, but in practice, this limit is generally not noticeable. In Section 1.3.3 of this thesis I will discuss direct measurements of the workfunction and how they are independent of choice of bias for most relevant biases less than 1eV.

With the prior form for the matrix elements, the tunneling equation now becomes:

$$I = \kappa\, e^{-\frac{z(V)}{z_\phi}} \int_0^{eV} \rho_t(E - eV)\rho_s(E)dE \tag{1.10}$$

where κ is a proportionality constant into which all the prior proportionality constants have been absorbed, and $z_\phi \equiv \frac{\frac{\hbar}{\sqrt{8m}}}{\sqrt{\phi}}$ is a parameter dependent on the convoluted workfunction (ϕ). I have also (finally) assigned metal 1 the role of my STM tip and metal 2 the role of my sample, an arbitrary choice, but one made with no loss of generality.

Finally, it is often assumed that the density of states of the tip is a constant in energy. While this is not necessarily the case, the material chosen for an STM tip is most often metallic, so a constant density of states for the energy ranges of

interest is to be expected. If we then pull $\rho_t(E)$ out of the integral and absorb it too into κ, the tunneling equation becomes

$$\boxed{I(\vec{r},z,V) = \kappa\, e^{-\frac{z(\vec{r},V)}{z_\phi}} \int_0^{eV} \rho_s(\vec{r},E)dE} \tag{1.11}$$

where $\vec{r}$ is the lateral (xy-plane) position, which will be very important soon. I have added explicit dependence on $\vec{r}$, z, and V to various quantities in the equation for explicitness.

Note that, although the workfunction (ϕ) is a mild function of z (and hence $\vec{r}$), I implictly assume that it is independent of $\vec{r}$. Although it is possible to create workfunction images, or maps, variations of workfunction are typically on the order of only a few percent on most surfaces, and the $\vec{r}$ dependence can be ignored in comparison to other effects, such as the density of states itself.

Equation 1.11 above is the usual starting point for thinking about experiments we can perform with STM. This "master tunneling equation" is the canonical tunneling equation used by many experimental STM researchers, reduced with assumptions for simplicity, as described above. We can manipulate it to produce theoretical expectations for, and relations between, different quantities to aid in understanding new measurements, as I will do in subsequent chapters. Thus, it is important to explicitly note the assumptions which are made in order to arrive at this equation. We will do this in the next section.

1.2 Various Assumptions

Let us review the various assumptions used to obtain Equation 1.11. For STM experimentation in general, not all of them may be applicable for every given case, so they should be noted and remembered.

1. *$E = qV$ and $q = ne$, with $n = 1$.* While it is generally expected that charge

carriers, at least in the normal state, have charge $q = e$, it is possible for this to not be the case. In particular, superconducting pairs are expected to have $n = 2$, and it is not obvious what the value of n is for charge carriers in the pseudogap regime (see Section 3.8) or near any of the phase transitions into the superconducting state. Until this is known, however, it is reasonable to assume an electron-like charge for normal state carriers.

2. ρ_t *is a constant.* It is very often assumed that the density of states of the tip (ρ_t) is a constant for almost all practical energies. This is because Fermi liquid theory, for all intents and purposes, gives a constant for ρ in conventional metals such as tungsten (or just about any metal). I therefore make this assumption wholeheartedly.

3. z *is a constant.* During these types of experiments, the tip-sample separation is theoretically held at a constant. This is a fairly naive assumption in various contexts which I will explore later.

4. $V/\phi << 1$. If we assume a small sample bias (V), then the ratio ϕ/V is large, and the matrix elements (M) of the quantum tunneling calculation may be considered to be energy (E) independent. Although this assumption seems somewhat arbitrary at first, evidence (see Section 4.2.2) will demonstrate that it is very plausible.

5. *The workfunction* ϕ *is independent of* r *and* z. Typically, although we tend to think of workfunctions as bulk properties of materials, they may vary on the atomic scale. However, these variations as measured by STM are only a few percent of the average workfunction measured on the surface, and do not contribute in comparison to larger variations of ρ_s and the integrated density of states.

6. $f(E) = \Theta(-E)$. Many STM experiments (and all of the ones discussed in

this thesis) are performed at low temperatures. "Low" temperatures are defined as being much less than 20K, usually around 4.2K, or for our dilution refrigerator, around 100mK or less. For low temperatures, it is a good approximation to replace the Fermi functions with Heaviside step functions ($\Theta(E)$), as demonstrated previously.

7. *Weak overlap of densities of state.* The density of states of both metals are assumed to be almost completely independent, with only a weak overlap.

8. *All tunneling is elastic.* For each quantum mechanical quasiparticle undergoing tunneling, its energy is assumed to remain constant before and after the tunneling process. Although inelastic tunneling processes are theoretically possible, and there are several experiments which observe and quantify these processes,[7] we should keep in mind that the tunneling equation does not, in its present form, describe such processes. The dependence of quantum mechanical theory on a Hamiltonian formulation necessarily requires conservation of energy, and the general tunneling equation does not account for energy losses (for example, to phonon or spin degrees of freedom).

Many of these assumptions are often quite valid; some, however, are valid only in certain situations and need careful consideration. In Section 4.2.2, we will see how one of these assumptions in particular, that z is a constant, breaks down, and how we can solve this implicit problem.

1.3 Types of Experimental Measurement

There are many types of experiment possible with an STM, and new measurement types are also in development. Here are just a few of the most common type of measurement performed in today's STM's.

1.3.1 Constant Current Topography

Commonly in STM experiments, an electronic feedback loop is used to keep a constant tunneling current above the sample. At a given, constantly applied bias V_0, piezoelectrics move the tip across the sample surface (varying $\vec{r}$). The feedback loop makes rapid, fine adjustments to z, the theoretical separation of the tip from the sample, in order to facilitate the constant current over the sample surface. In such a case, the current (I) in the tunneling equation 1.11 is (by feedback design) a constant in $\vec{r}$ and z; however, z, the tip-sample separation, is still dependent on both $\vec{r}$, the x-y position on the surface of the sample, and V_0, the sample bias. Explicitly,

$$I_0(V_0) = \kappa\, e^{-\frac{z(\vec{r},V_0)}{z_\phi}} \int_0^{eV_0} \rho_s(\vec{r},E)dE \tag{1.12}$$

The subscripts '$_0$' indicate constant values: I_0 means that the current is held at a constant by feedback, and V_0 means that the bias is also held at a constant, not by feedback but simply as an applied voltage.

Note that, whereas the spatial dependence of I is (theoretically) gone, the $\vec{r}$ dependence of z and ρ_s remain. In fact, $z(\vec{r},V_0)$ is defined to be a "topograph", which is a 2D image that shows how much z has to vary as the tip is scanned in r across the sample surface in order to maintain the constant current. Moreover, the explicit topograph representation in this model is

$$z(\vec{r},V_0) = -z_\phi ln\left[\frac{I_0(V_0)}{\kappa \int_0^{eV_0}\rho_s(\vec{r},E)dE}\right] \tag{1.13}$$

In effect, the topograph is a visual representation of the corrogations of a sample surface. It is *not* a representation of a local density of states or charge density, but rather is a reflection of the total effect of all local quasiparticles occupying all energy levels (from the Fermi level E_F to the bias energy) at particular points on the surface. Atomic (lattice) densities, vacancies, and impurities are easily

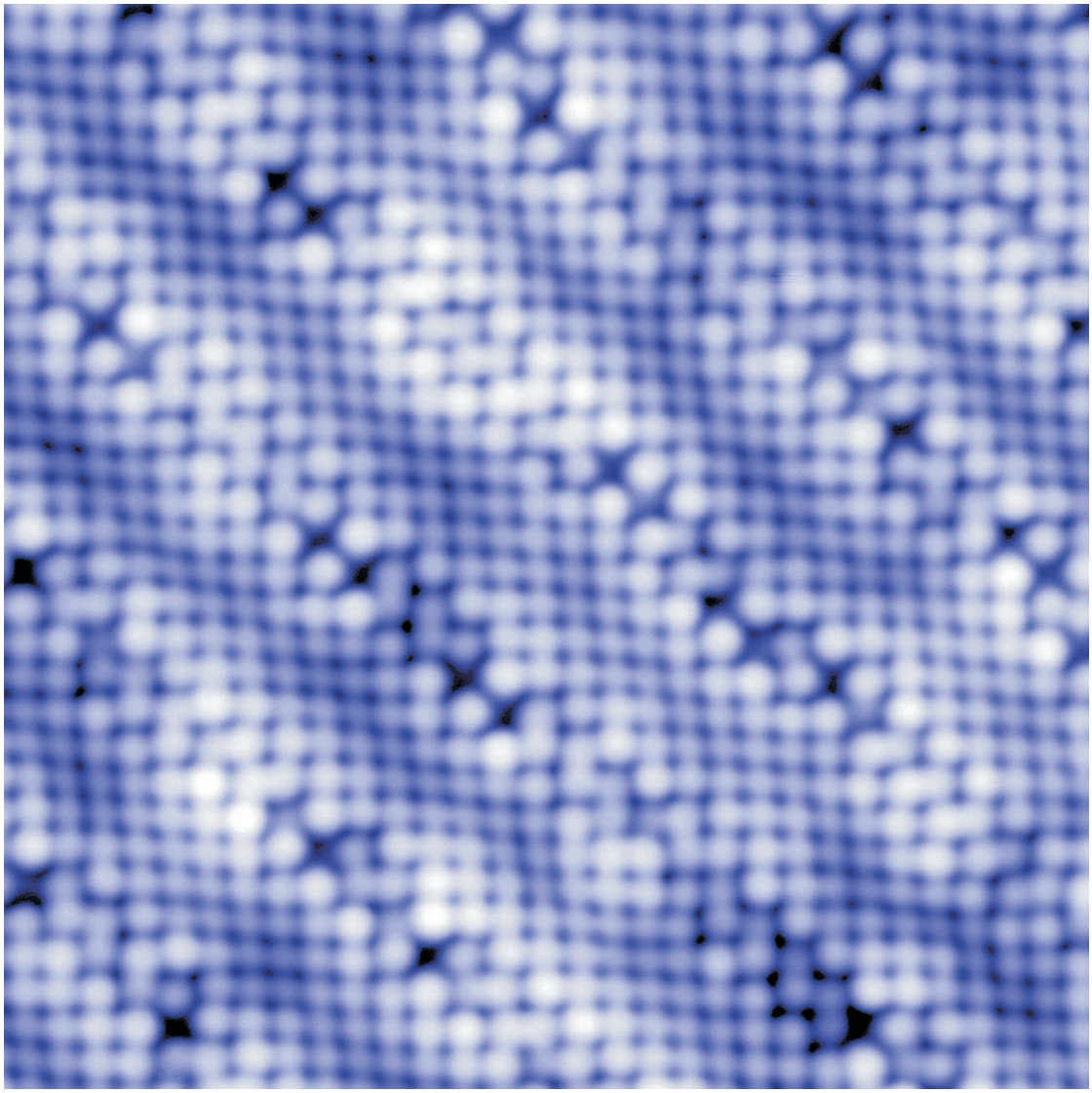

Figure 1.3: An Example of a Topograph, BSCCO. T_C=45K for the BSCCO sample shown. The size of the field of view is 12nm×12nm. The supermodulation, or surface reconstruction, of BSCCO is clearly evident, along with lattice vacancies.

found with a topograph, as well as larger features such as step edges and surface adsorbates. Example topographs are shown in Figures 1.3 and 1.4.

Because z is logarithmic in the current I, the feedback mechanism will be able to detect small changes in z as large deviations from the setpoint current (I_0). This allows quick feedback response and better feedback sensitivity than, for example,

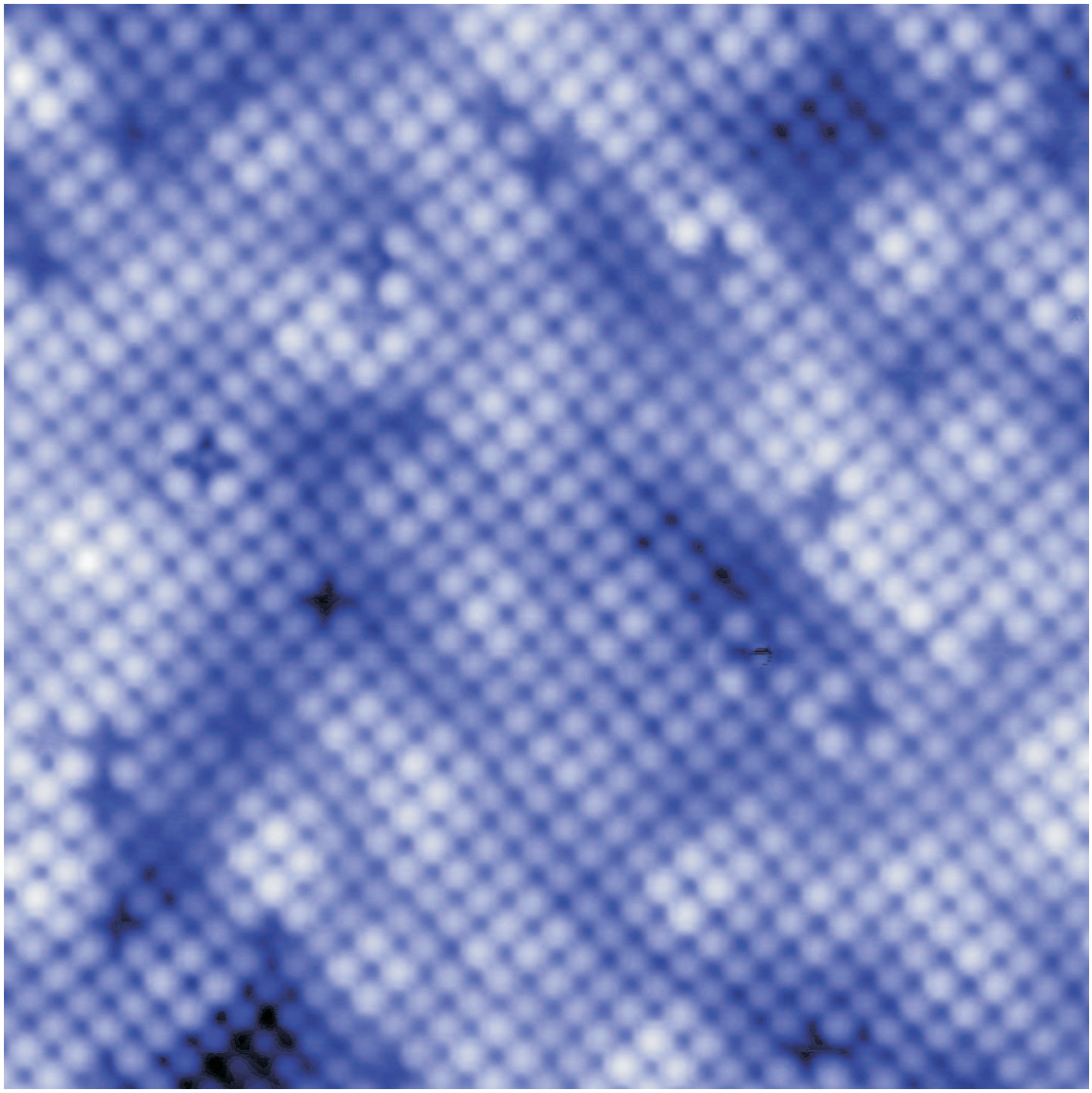

Figure 1.4: An Example of a Topograph, NaCCOC. This NaCCOC sample is doped p=0.12 and T_C=21K. The size of the field of view is 11.5nm×11.5nm. Many lattice vacancies are readily apparent.

if the two quantities were related linearly.

1.3.2 An Interlude: Setpoint Effect and Mapping with an STM

The STM has the ability to measure various quantities in a 2D image format, or map, in real-space as the STM tip is scanned across the sample surface. (This is discussed in more detail in Section 2.2.) If these type of experiment use feedback in order to reposition the tip before the measurement is made (which is extremely common), then the results of the experiment are subject to what is known as the *setpoint effect*, or setup condition effect. This systematic effect will impact the results of any measured quantity, but usually, it only matters in cases in which there is $\vec{r}$ dependence on the quantity (i.e. a map). (As an aside, photoemission studies have a similar technical limitation which is also referred to as a setpoint effect.) I shall discuss how the effect is eliminated to produce new physical observables in Section 4.1.3.

The z value, or tip to sample separation, on which the STM settles as it moves into position just before a measurement is a function of the setpoint (constant bias V_0 and current I_0), and unfortunately, the measured quantity will change depending on the choice of V_0. This systematic error occurs even if one corrects for the fact that the tunneling resistance, $R \equiv \frac{V_0}{I_0}$, is not the same between measurements with differing V_0.

Consequently, we must allow z to have setpoint bias (V_0) dependence, which is why I wrote $z(V)$ starting with Equation 1.10. So, in cases in which there is $\vec{r}$ dependence for quantities measured after feedback repositioning, we must write $z(V)$ as

$$z(\vec{r}, V_0) \tag{1.14}$$

But there is something special about the above quantity. We have seen it be-

fore, in Equation 1.12. In fact, the prefactor above is essentially a *topograph*, as I showed in the previous section. That is to say, the setpoint effect manifests itself as a modification to our measurable quantity (e.g. $g \equiv \frac{dI}{dV}$) which is mathematically equal to a topograph taken with the same setpoint. In other words, due to the nature of feedback itself, measurable quantities become contaminated with a topograph-like envelope that is usually a significant modification to the actual desired quantity. We can write an expression for the prefactor in a form from the topograph equation:

$$\kappa\, e^{-\frac{z(\vec{r_0},V_0)}{z_\phi}} = \frac{I_0(V_0)}{\int_0^{eV_0} \rho_s(\vec{r_0},E)dE} \equiv \zeta(r_0,V_0) \tag{1.15}$$

As one can see above, the prefactor is a constant for a particular choice of r_0 and bias V_0, which means that for one chosen point on a map (or a single measurement which does not depend on $\vec{r}$), the measurement is still proportional to the actual desired value. For this reason, the setpoint effect is usually not an issue until a map is created and neighboring $\vec{r}$ sites are compared to one another.

I will henceforth refer to the setpoint prefactor as $\zeta(r_0, V_0)$, as defined above.

1.3.3 Workfunction Measurements (Bulk)

We may also use an STM to obtain a measure of the workfunction of the sample. If one first chooses a particular position on the sample surface ($\vec{r_0}$) as well as a bias energy (V_0), the workfunction may then be calculated, and it is uniquely determined up to small variations with $\vec{r}$ or z. Starting again from Equation 1.11 but with these substitutions, we then have

$$I(\vec{r_0},z,V_0) = \kappa\, e^{-\frac{z(\vec{r_0},V_0)}{z_\phi}} \int_0^{eV_0} \rho_s(\vec{r_0},E)dE \tag{1.16}$$

Taking the logarithm of both sides and arranging the terms suggestively, the

equation now reads

$$ln\left[I(\vec{r}_0, z, V_0)\right] = \left[-\frac{1}{z_\phi}\right] z(\vec{r}_0, V_0) + ln\left[\kappa \int_0^{eV_0} \rho_s(\vec{r}_0, E)dE\right] \tag{1.17}$$

This is a linear equation given in standard slope/y-intercept form ($y = slope * x + b$) for a straight line with $y \approx ln\left[I(\vec{r}_0, z, V_0)\right]$, $slope \approx -\frac{1}{z_\phi}$, $x \approx z(\vec{r}_0, V_0)$, and y-intercept $b \approx ln\left[\kappa \int_0^{eV_0} \rho_s(\vec{r}_0, E)dE\right]$. Thus, if you measure the current I while varying z for a given choice of $\vec{r}$ and V, the a plot of the natural logarithm of the current versus z will have a slope that will give a measure of the workfunction. Specifically,

$$slope \approx -\frac{1}{z_\phi} = -\frac{\sqrt{8m}}{\hbar}\sqrt{\phi} \tag{1.18}$$

(See Equation 1.10.) Thus,

$$\phi = \frac{(\hbar * slope)^2}{8m} \tag{1.19}$$

Recall that ϕ is the *convoluted* workfunction, not just the workfunction of the sample alone. Measuring the workfunction is one procedural benchmark used in the characterization of STM tips.

It is also possible to create workfunction images, which map out the small variations in this measured workfunction over the xy-plane. An example image of such a workfunction map is shown in Figure 1.5.

1.3.4 Differential Conductance Spectroscopy

This type of experiment is often called Scanning Tunneling Spectroscopy (STS), or simply a "spectrum". It is the basic measurement used to obtain a reasonable measure of the electronic occupation, or local density of states, in a sample at one finely-chosen position on the sample surface. However, there are a few nuances to this characterization of the technique which should be examined more carefully.

Figure 1.5: (**Top**) An Example of a Workfunction Map, NaCCOC. This NaCCOC sample is doped p=0.12 and T_C=21K. The size of the field of view is 11.5nm×11.5nm. (**Lower-Left**) The energy ranges from 5.6eV in **black** to 9.6eV in white. (**Lower-Right**) Histogram of the workfunction image values. Although there is spatial variation in the workfunction values, it is a small fraction of the average workfunction value.

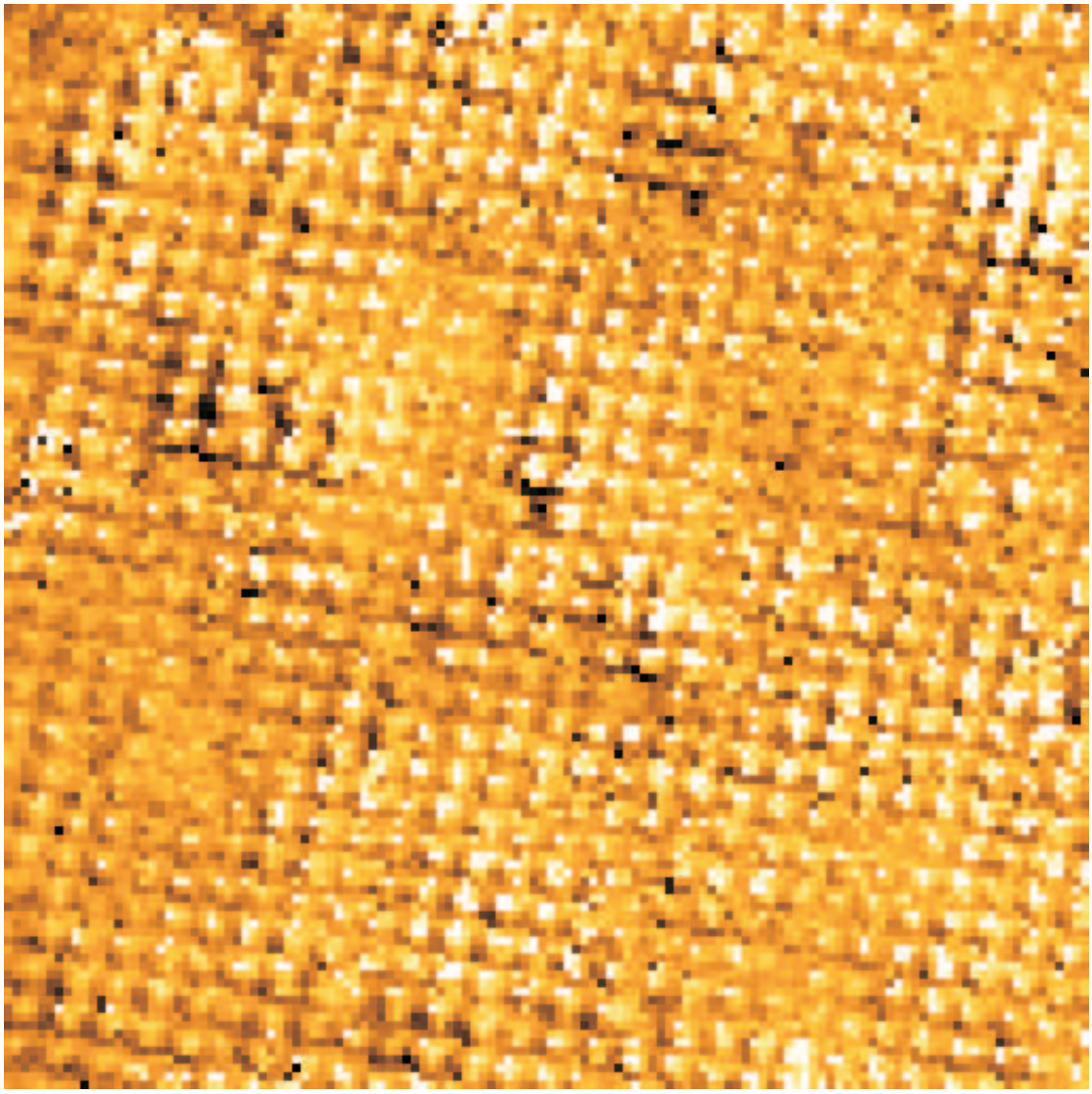


9.6eV
5.6eV

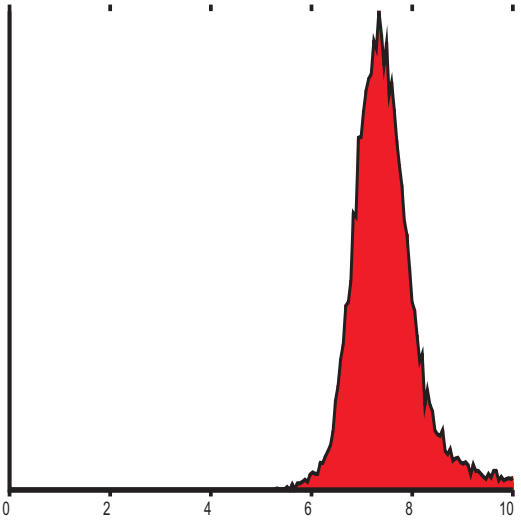
0
2
4
6
8
10

I will first present the naive representation of differential conductance spectroscopy, showing how, in a simple model, the conductance $g \equiv dI/dV$ measured while tunneling through a sample is proportional to the the sample's local density of states $\rho_s(\vec{r}, E)$. Then, I will show the setpoint effect corrected version of the same quantity.

For a single spectroscopy measurement, the tip moves, in electronic feedback, across the sample surface, and it is halted at one particular $\vec{r}$ location and z distance above the surface (determined by the V_0 and I_0 setpoint). Next, feedback is turned off, and the bias V is ramped through a chosen energy range while the current I is measured simultaneously with g. The measurement is done with no electronic feedback, so neither z nor $\vec{r}$ change during the experiment for any (intentional) reason. Once again invoking Equation 1.11, we can denote z_0 as the constant tip-sample distance and $\vec{r}_0$ as the x-y plane value which are chosen before the spectral measurement. Taking the derivative with respect to bias (V) in an effort to calculate $\frac{dI}{dV}$, we obtain

$$\frac{dI(\vec{r}_0, z, V)}{dV} = \kappa \, e^{-\frac{z_0}{z_\phi}} \frac{d}{dV} \int_0^{eV} \rho_s(\vec{r}_0, E) dE \tag{1.20}$$

Recall that the Fermi Energy E_F has been defined to be 0, for convenience (see Section 1.1). There are several mathematically equivalent ways to proceed. I will show my preferred method.

The method is to use Liebniz's Integral Rule for differentiation of an integral, a trick used when the differentiation is dependent on one or both of the integration limits. This rule is also known as "differentiation under the integral sign", and it assumes that functions are well-behaved (uniformly continuous) and differentiable. The fundamental theorem of calculus is a special case of Leibniz's Rule. I use the

version of the Leibniz's Rule applicable to monovariant functions:

$$\frac{d}{dx}\int_{f_1(x)}^{f_2(x)} g(t)dt = g(f_2(x))\frac{df_2(x)}{dx} - g(f_1(x))\frac{df_1(x)}{dx} \tag{1.21}$$

Substituting in Equation $x \approx V$, $t \approx E$, $g(t) \approx \rho_s(E)$, $f_1(x) \approx 0$, and $f_2(x) \approx eV$, we see immediately that the second term above vanishes, and the expression $\frac{df_2(x)}{dx} \approx \frac{d(eV)}{dV} = e$. Hence, what remains is

$$\frac{d}{dV}\int_0^{eV} \rho_s(E)dE = e\rho_s(eV) \tag{1.22}$$

Equation 1.20 becomes

$$\frac{dI(\vec{r_0}, z_0, V)}{dV} = \kappa\, e^{-\frac{z_0}{z_\phi}} e\rho_s(\vec{r_0}, eV) \tag{1.23}$$

or, neglecting the (assumed) constants,

$$\boxed{g(\vec{r_0}, V) \equiv \frac{dI(\vec{r_0}, z_0, V)}{dV} \propto \rho_s(\vec{r_0}, eV)} \tag{1.24}$$

Once again, g is the *differential conductance* at a particular energy (eV).

Equation 1.24 is not strictly correct, as I explained in Section 1.3.2. In fact, it is not a good approximation in many experiments to regard z, the tip-sample separation, as a constant as I did in Equation 1.20 when I replaced z with z_0. This is because of the setpoint effect, which causes quantities to be dependent on the particular bias (V_0) which the feedback settles upon before the measurement. If I substitute the setpoint prefactor term ($\zeta(r_0, V_0)$) back into back into Equation 1.20 (with z now having V_0 dependence), we obtain

$$g(\vec{r_0}, V) = \zeta(r_0, V_0)e\rho_s(\vec{r_0}, eV) \tag{1.25}$$

or the more utilitarian

$$\boxed{g(\vec{r_0}, V) \propto \zeta(r_0, V_0)\rho_s(\vec{r_0}, eV)} \tag{1.26}$$

This is the more accurate and useful expression for a differential conductance spectrum.

1.3.5 Differential Conductance Mapping

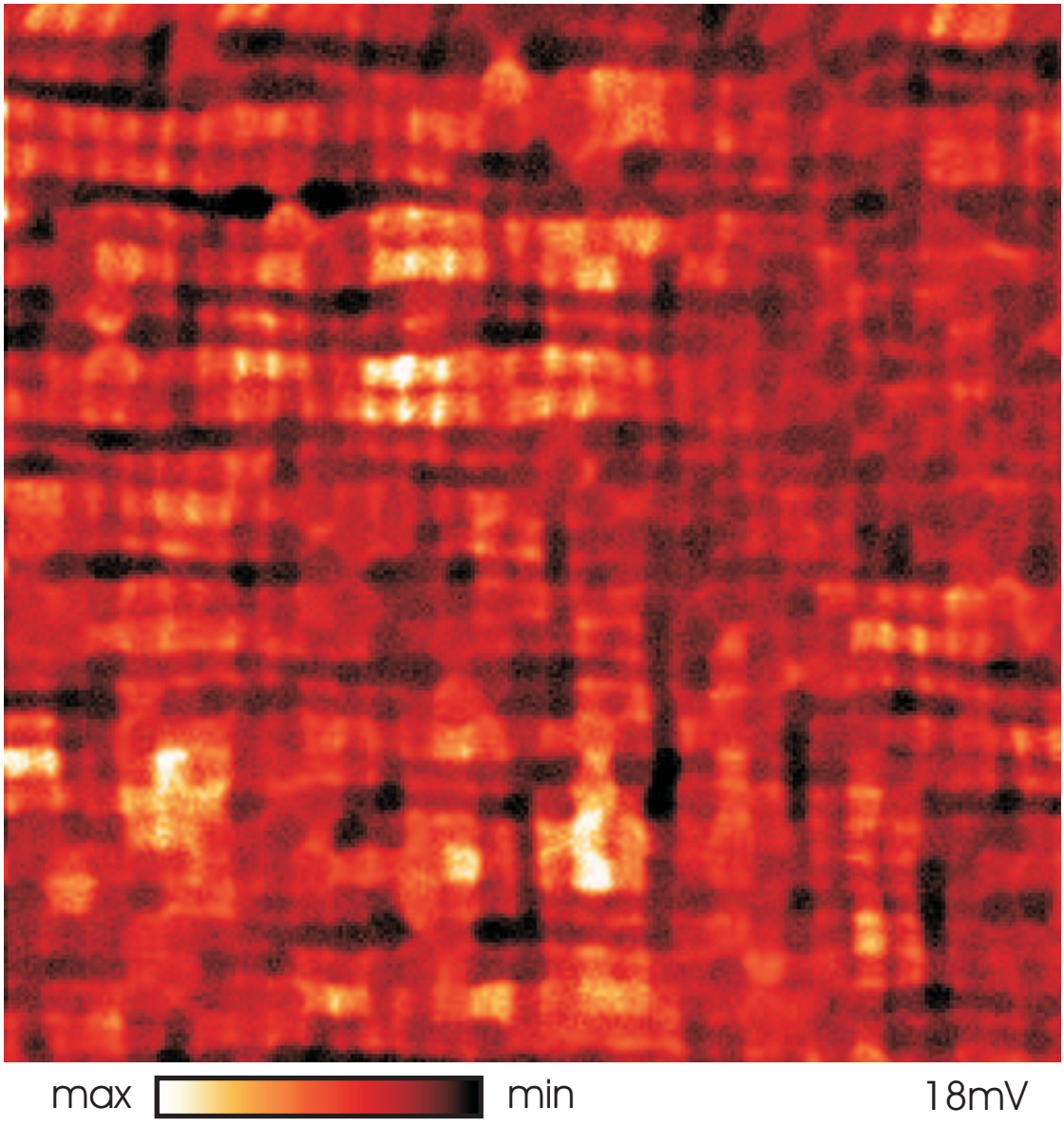

Figure 1.6: An Example of a Differential Conductance Map, BSCCO. This map is taken in the same field of view as that of the topograph in Figure 1.3. The energy of this particular layer is 18mV.

Now that we understand how one differential conductance spectrum is measured, we can simply take an array of these measurements in a uniformly-spaced grid on the sample surface to form a measure of the *local density of states*, or

LDOS, on different areas of the sample. In doing so, we may mentally allow $\vec{r_0}$ to vary in Equation 1.26, and return it to its continuous representation, $\vec{r}$.

Thus, for differential conductance mapping, we have

$$\boxed{g(\vec{r},V) \propto \zeta(\vec{r},V_0)\rho_s(\vec{r},eV)} \tag{1.27}$$

or, in the less-correct formulation,

$$g(\vec{r},V) \propto \rho_s(\vec{r},eV) \tag{1.28}$$

Although $\vec{r}$ is, strictly speaking, a continuous variable, points on the 2D plane are sampled discretely, on a raster. Since spectroscopic measurements are made at points quite close to one another in a typical differential conductance map, we usually need not think of $\vec{r}$ as anything but continuous. However, keep in mind that each point on the xy-plane specified by $\vec{r}$ represents an independent spectroscopic measurement.

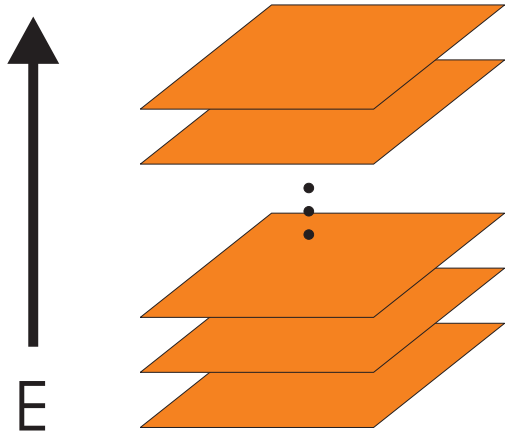

Figure 1.7: A generic $g(\vec{r},E)$ or $I(\vec{r},E)$ layered object. Each layer is a 2D array of data which represents a distinct, discrete energy level E.

The $g(\vec{r},V)$ object forms a 3D grid of raw data which is used as a basis for analyses of various types in STM research. One may think of differential conductance maps as a stack of pancakes, each pancake being a 2D image representing

$g(\vec{r})$ and having an energy eV which is definite and discrete (see Figure 1.7).[5] An example of a differential conductance map is shown in Figure 1.6.

1.3.6 Current Mapping

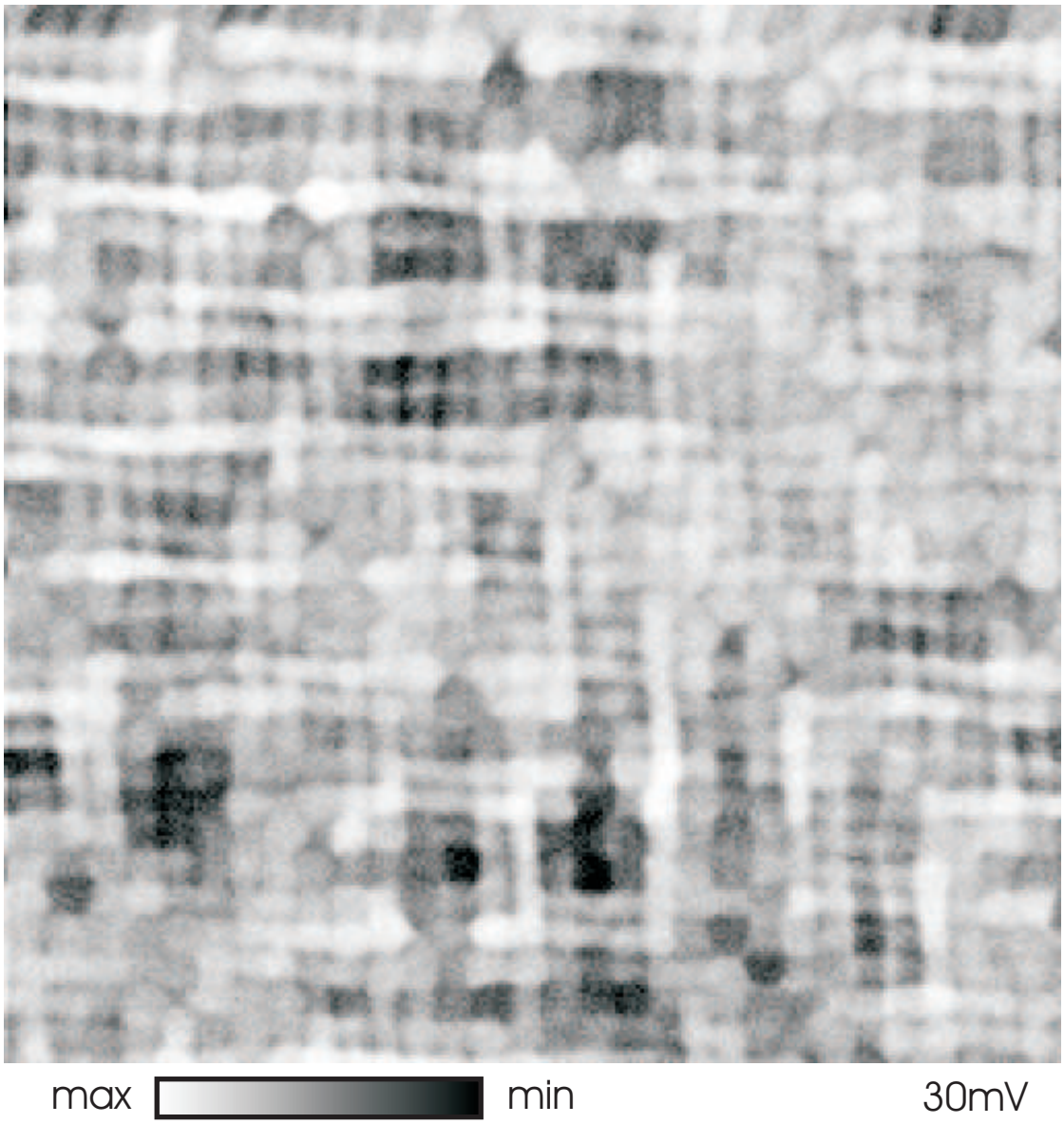

Figure 1.8: An Example of a Current Map, BSCCO. This map is taken in the same field of view as that of the topograph in Figure 1.3. The energy of this particular layer is 30mV.

Current maps $I(\vec{r}, V)$ are taken simultaneously with a differential conductance map which represent $I(V)$ curves at every point on the raster. Equivalently, they represent a 2D image $I(\vec{r})$ of the current for every discrete energy eV. We again consider the bias-dependent prefactor as discussed in the previous section in Equation 1.15. Because measurements at each point in the current map have a bias dependence, we again have a setpoint effect, and therefore must replace the prefactor in Equation 1.11 with the bias-dependent one. This gives

$$\boxed{I(\vec{r}, z, V) \propto \zeta(r_0, V_0) \int_0^{eV} \rho_s(\vec{r}, E) dE} \tag{1.29}$$

after relaxing the equality to a proportionality.

Current maps can hold just as much relevant physical information as do differential conductance maps, as I will show in future chapters. An example of a current map is shown in Figure 1.8.

BIBLIOGRAPHY

[1] W. R. Bandy and A. J. Glick. Tight-binding green's-function calculation of electron tunneling. i. one-dimensional two-band model. *PRB*, 13:3368–3380, apr 1976.

[2] J. Bardeen. Tunnelling from a many-particle point of view. *Phys. Rev. Lett.*, 6(2):57–59, Jan 1961.

[3] G. Binnig and H. Rohrer. Scanning tunneling microscopy. *IBM Journal of Research and Development*, 30(4):355, 1986.

[4] D. J. Griffiths. *Introduction to Quantum Mechanics, 1st. ed.* Prentice Hall, Inc., Upper Saddle River, NJ 07458, 1995.

[5] J. Hoffman. *A Search for Alternative Electronic Order in the High Temperature Superconductor $Bi_2Sr_2CaCu_2O_{8+\delta}$ by Scanning Tunneling Microscopy.* PhD thesis, University of California at Berkeley, 2003.

[6] E. Hudson. *Investigating High-T_C Superconductivity on the Atomic Scale by Scanning Tunneling Microscopy.* PhD thesis, University of California at Berkeley, 1999.

[7] J. Lee, K. Fujita, K. McElroy, J. A. Slezak, M. Wang, Y. Aiura, H. Bando, M. Ishikado, T. Masui, J.-X. Zhu, A. V. Balatsky, H. Eisaki, S. Uchida, and J. C. Davis. Interplay of electronlattice interactions and superconductivity in $Bi_2Sr_2CaCu_2O_{8+\delta}$. *Nature*, 442:546–550, 2006.

[8] M. Razavy. *Quantum Theory of Tunneling.* World Scientific Publishing Co. Pte. Ltd., 5 Toh Tuck Link, Singapore 596224, 2003.

[9] J. Tersoff. Anomalous corrugations in scanning tunneling microscopy: Imaging of individual states. *Phys. Rev. Lett.*, 57(4):440–443, Jul 1986.

[10] J. Tersoff. Sample-dependent resolution in scanning tunneling microscopy. *Phys. Rev. B*, 39(2):1052–1057, Jan 1989.

[11] J. Tersoff. Role of tip electronic structure in scanning tunneling microscope images. *Phys. Rev. B*, 41(2):1235–1238, Jan 1990.

[12] J. Tersoff and D. R. Hamann. Theory and application for the scanning tunneling microscope. *Phys. Rev. Lett.*, 50(25):1998–2001, Jun 1983.

[13] J. Tersoff and D. R. Hamann. Theory of the scanning tunneling microscope. *Phys. Rev. B*, 31(2):805–813, Jan 1985.

Chapter 2
Experiment Setup and Methods

2.1 Laboratory Infrastructure

Ultra-low vibration, very low-noise, very low-temperature, scanning tunneling microscopy (STM) experiments require much supporting hardware. Here I describe both the basic, and more advanced, techniques used to realize our quality experiments.

2.1.1 Feedback Circuitry

Figure 2.1 shows a schematic representation of the basic STM current loop circuit. In constant-current mode, a constant bias is applied by the ECU (Electronic Control Unit) to the tip/sample junction, which is inside the cryostat (in situ). The potential difference results in a tunneling current if the tip is sufficiently close to the sample. This current is converted to a voltage by a current preamplifier outside the system and is passed back into the ECU. A feedback control algorithm inside the ECU (a PID; or Proportional, Integral, Derivative; control system) determines how much the tip needs to move in order to maintain a constant current. The voltage on Z, the vertical piezo signal, is then adjusted to retract or extend the piezo tube as needed.

While all of the above is happening, the ECU also controls the lateral position of the tip. It does this by applying a potential difference across either side of the piezo tube, in either the X or the Y directions. If scanning in topographic mode, the $\pm$X and $\pm$Y voltages are automatically adjusted and timed such that the piezo tube will cause the tip to traverse the surface, one line at a time. This allows the creation of the topograph image in accordance with Section 1.3.1 by tracking the

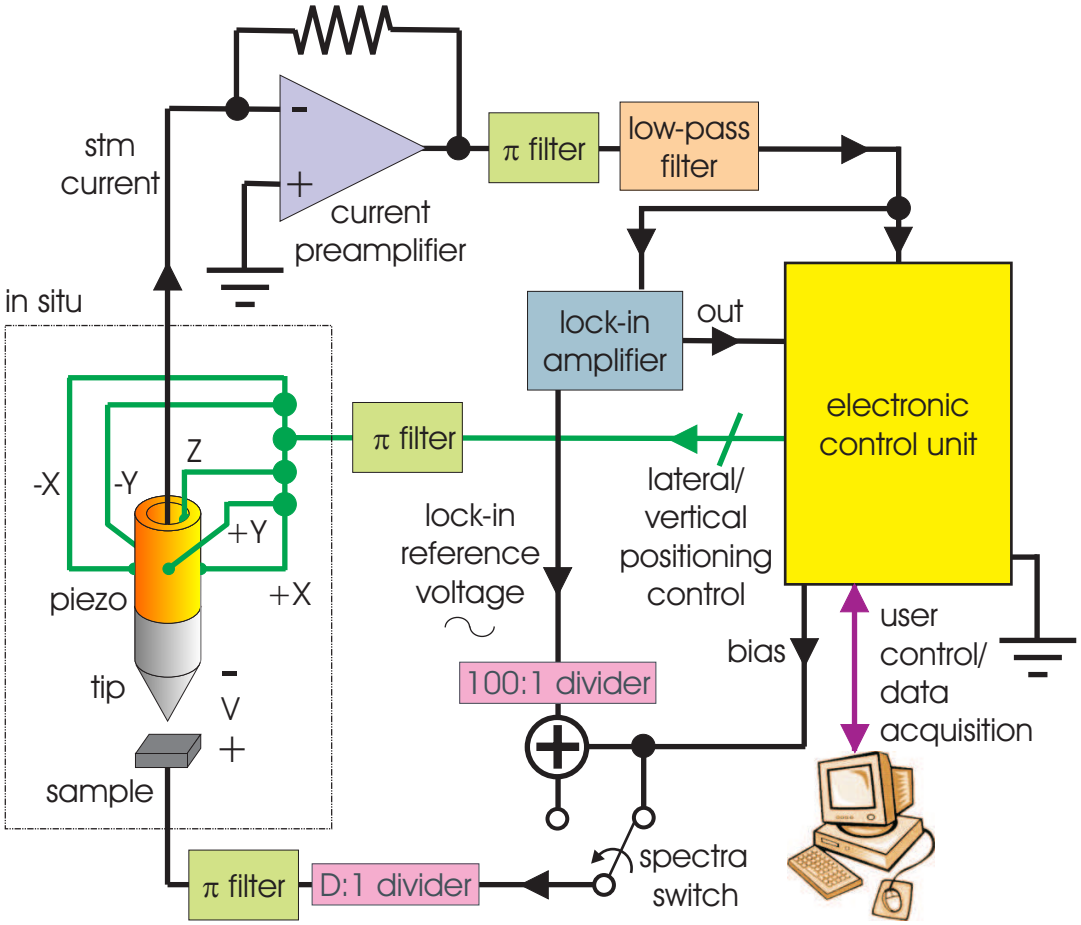

Figure 2.1: Schematic of Constant-Current Feedback Circuit. The schematic is simplified for illustration important major components, but is not to scale. The STM current flows from the STM junction in situ to a current preamplifier, through a few filters, and into the electronic control unit (ECU). If in feedback, the ECU adjusts the bias to keep the current at a constant value based upon the current measurement. The ECU also controls timing of lateral (±X,±Y) and vertical (Z) high voltages for piezo positioning. If spectra are being measured out of feedback, the a lock-in reference voltage is added to the (constant) value of the bias, and the lock-in signal is sent to the ECU for capture. The "spectra switch" is not a real switch, but is technically a function inside the ECU, as is the 100:1 divider.

value of the feedback voltage Z across the sample surface.

If scanning in differential conductance (spectra) mode, the scanning behavior described above similarly occurs, but at each point on the image grid, the feedback

stops momentarily. All X, Y, and Z adjustments cease, and a spectra curve is measured out of electronic feedback. This will be described in more detail in Section 2.2.2.

2.1.2 Liquid Helium Dewar

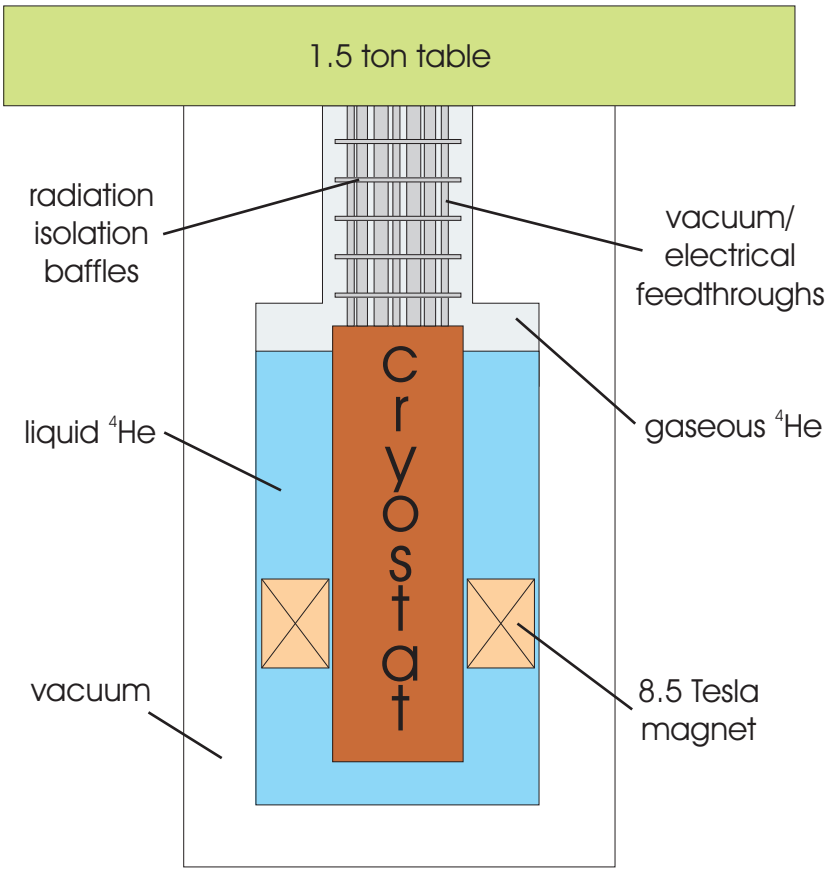

Figure 2.2: Schematic of LHe Dewar. The cryostat sits in a ^{4}He bath at 4.2K. The bath space is surrounded by several layers of vacuum padding to provide excellent thermal and radiative isolation, and radiative baffles shield from thermal radiation near the top of the dewar. Feedthroughs for a variety of purposes including vacuum pumping, electrical signals, and mechanical manipulation support the cryostat. An 8.5 Tesla superconducting magnet surrounds the core of the experiment.

The basic enclosure surrounding a low-temperature physics experiment is the liquid helium (LHe) dewar. Modern dewars may be customized to accommodate almost any diameter experiment, although other considerations (such as magnetic field strength or size and weight of the dewar) may independently constrain the maximum allowable size of the experiment.

The dewar consists of a hollow inner cylindrical core which is filled with liquid ^4He, or LHe, during an experiment measurement (see Figure 2.2). This LHe "bath space" cools the insert, as well as shields it mildly from radiative heating. Around the bath space is at least one vacuum jacket layer, more in modern dewars for better isolation. (Our dewar has 3 jacket layers.) Theoretically, the best insulator of all is nothing (i.e. a vacuum), and thus dewars use a strong vacuum to thermally insulate the inner system from conductive and radiative heat leaks.

Liquid helium has a low latent heat at 4.2K, but in comparison to the cooling power possible through use of the enthalpy of ^{4}He from 300K to 4.2K, it is greatly advantageous to use the warming of the gas as well to cool the cryostat.[9] In addition, the latent heat of liquid nitrogen (LN_2) is $\sim$60 times that of LHe, and LN_2 is far cheaper. Hence, using LN_2 to cool to 77K makes economic sense both monetarily and temporally. Our cooldown procedure incorporates a LN_2 phase, a LHe phase, and then a dilution refrigerator phase which can bring the base temperature of the fridge down to a minimal temperature of 10mK, if desired.

2.1.3 Cryostat and Dilution Refrigerator

The heart of the experiment is the cryostat, which houses the dilution refrigerator, sample insertion mechanisms, thermometers, electronic wiring, geophone, and various other onboard apparatuses, in addition to the STM itself. The dilution refrigerator in particular allows temperature floors of around 10mK accompanied

with cooling power high enough to reliably cool large pieces of metal and other objects in good thermal contact with the fridge.

2.1.3.1 Refrigerator Components Internal to Cryostat

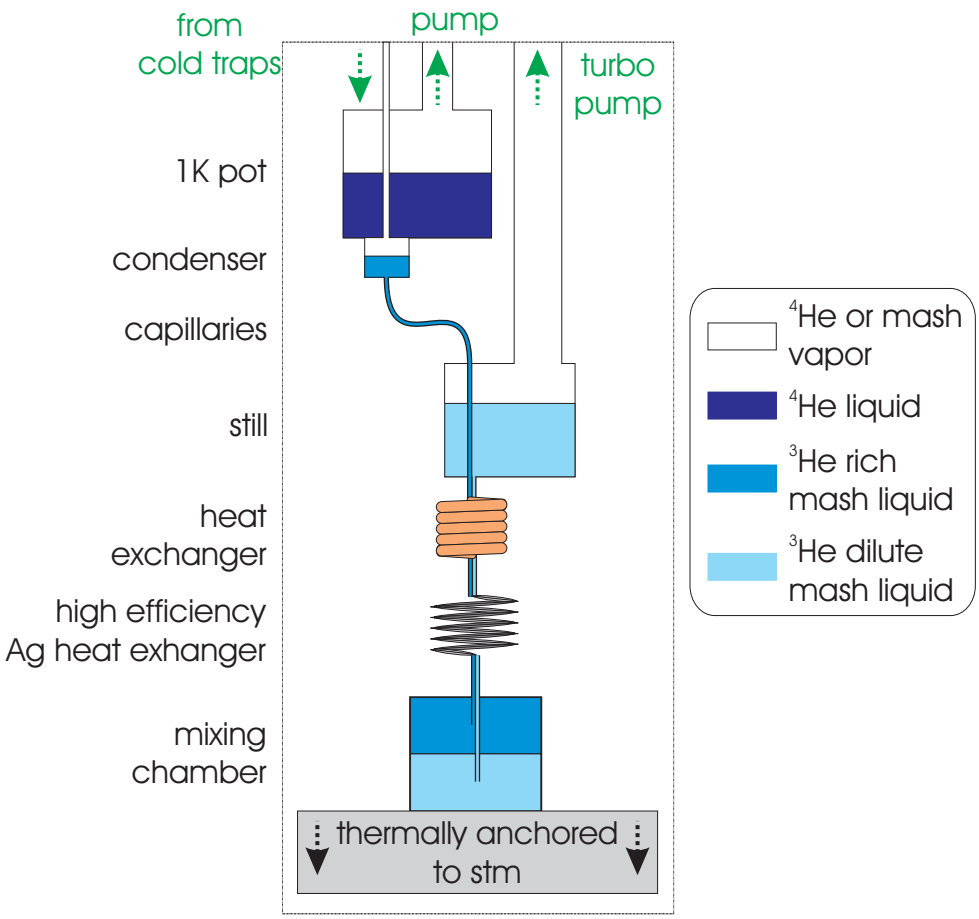

Figure 2.3: Interior of Cryostat: Dilution Refrigerator Components. The major components of a dilution refrigerator are shown.

As mash (slang for ^{3}He/^{4}He mixture) enters into the dilution refrigerator unit inside the cryostat, shown in Figure 2.3, the mixture is pre-cooled by a 1K pot to promote condensation. The 1K pot is a small metal enclosure of about 100 cm^3 which is filled with normal liquid ^{4}He. The liquid ^{4}He enters the pot from the LHe bath at 4.2K through a long siphon (not shown in the figure). As the vapor pressure

of the liquid ^{4}He is pumped away by a high-power mechanical pump, the liquid reduces in temperature to around 1.2K. Moreover, it undergoes a phase transition to the superfluid ^{4}He state.[9, 10] This results in increased cooling efficiency over a situation in which mash may be pre-cooled by ^{4}He alone, without evaporative cooling.

Ideally, the mixture will condense in a small volume thermally connected to the 1K pot called the condenser. The mash will then travel through a series of heat exchangers, one anchored to the still and two connected to returning mash. The purpose of these exchangers is to remove as much heat as possible from the liquid mash entering the system before it arrives into the mixing chamber. This job is so important that several heat exchangers are used in order to get the job done, the last one being a high-efficiency silver sintered heat exchanger (expensive).

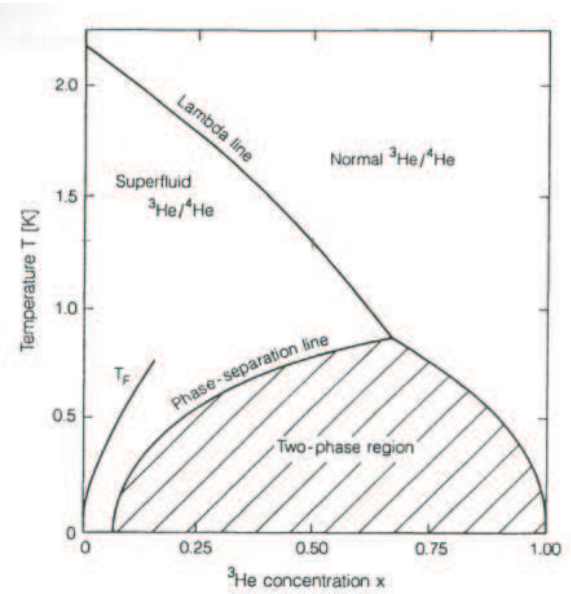

Figure 2.4: Mash (^{3}He/^{4}He Mixture) Concentration Phase Diagram.[1] Saturated vapor pressure is assumed.

Once the mash reaches the mixing chamber, if the refrigerator has been constructed properly, it has cooled below 0.7K, the temperature at which the tricritical

point exists in the phase diagram (see Figure 2.4). The tricritical point separates superfluid ^{3}He/^{4}He, normal ^{3}He/^{4}He, and a state in which there is phase separation between ^{3}He rich and ^{3}He dilute mixtures. The striking and critical property of mash is that as temperature is lowered to 0K, there always remains a finite concentration of ^{4}He, even though the fraction is small ($\sim$6%). This is due to the fact that ^{3}He and ^{4}He are both quantum liquids, and therefore may have a zero entropy (S=0) for T=0K even though there is only partial solubility in that limit.

If the mash temperature is below the lambda point, at least some of the two-liquid, phase separated state exists at saturated vapor pressure. Meanwhile, vapor pressure (almost purely ^{3}He, due to its high vapor pressure) is being pumped away in the still from the dilute phase. This results in a destruction of thermal equilibrium and, due to the osmotic pressure[9] difference between the two phases, the lighter ^{3}He rich phase is encouraged to give up some of its ^{3}He atoms to the denser ^{3}He dilute phase, a process which causes cooling. The ^{3}He vapor pressure is then pumped away by at the still, and the same ^{3}He gas is returned to the system through the condenser line, completing the cycle.

2.1.3.2 The Dilution Refrigerator Closed-Loop Circuit

On a large scale, the dilution refrigerator is a closed-loop circuit through which mash, a mixture of ^{3}He and ^{4}He, is pumped continuously. Mash is pulled into the inlet of two pumps connected in series, and is pushed from the outlet of the second pump into the rest of the circuit. In our case, the first pump is a turbo pump which performs work on a large diameter cross sectional area coming from the dilution fridge in the cryostat. The purpose of using a higher-powered pump and a larger cross sectional area is to increase the pumping power of the circuit, which is one factor in determining the base temperature of the refrigerator. Our dilution refrigerator is designed to have a cooling power of 400 μW. When mash leaves the

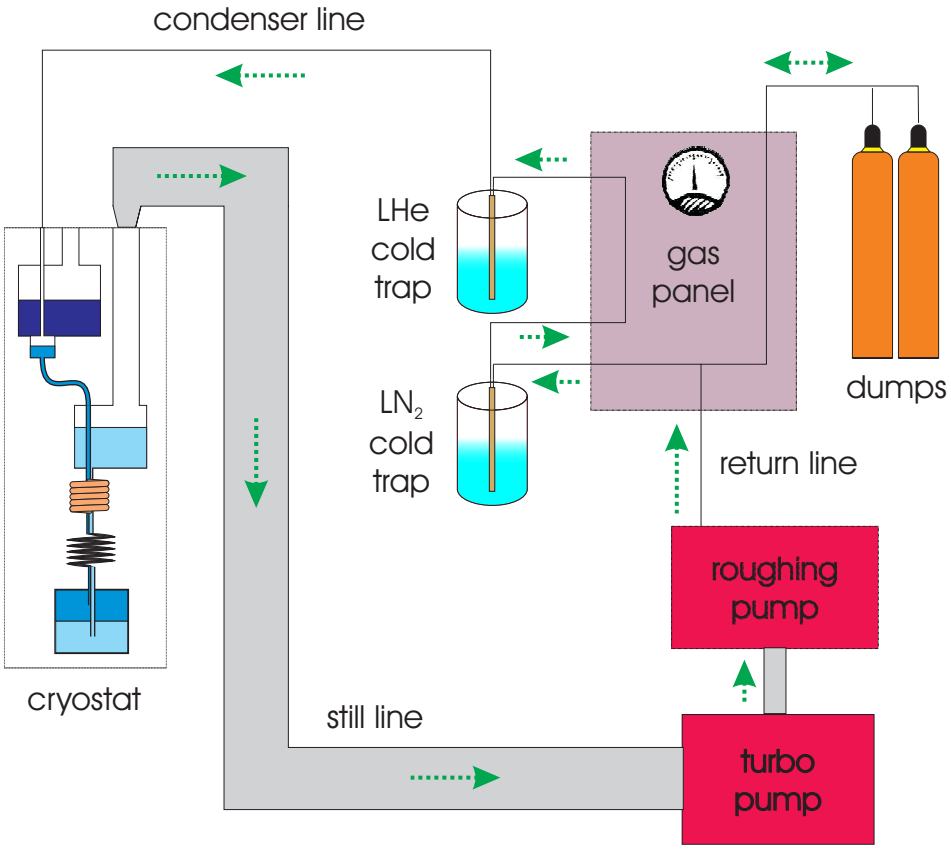

Figure 2.5: Dilution Refrigerator Closed-Loop Circuit. Mash flows from the cryostat through circulation pumps, cold trap filters, and back to the experiment. Dumps are used for mixture storage and over- or under-pressure safety.

second pump, it is pushed through a series of cold traps, which are cryogenic filters used to "clean" the mash (see Section 2.1.3.4). After cleaning, the mash enters the high impedance condenser line, which has a flow rate controlled by a precision throttling valve. The mash then enters the cryostat through the condenser line and is pre-cooled by the 1K pot, as described before.

2.1.3.3 Modes of Operation

Mash may enter or leave the circuit as pressure demands through a connection to the dumps, which are mash storage tanks. There are several modes of operation of

a dilution refrigerator; among them are "continuous", "closed-circuit", and "one-shot" modes. These modes are generally controlled by opening or closing particular valves in the closed circuit, and also those connecting the circuit to the dumps, at particular times. In continuous mode, all valves are open, including those to the dumps (generally for overpressure and underpressure safety). This mode has the advantage of being able to cool indefinitely, but the disadvantage of additional room-temperature mixture continuously entering the system through the condenser valve (and thus heating the fridge). For my tenure in this lab, dilution refrigerator experiments were performed in continuous mode. Closed-circuit mode is similar to continuous mode except the connection to the dumps is severed. (i.e. The amount of mixture in the closed circuit is kept at a constant.) In one-shot mode, the mixture is allowed to condense in the mixing chamber of the fridge with all valves open. Then, a valve between the pump return line and the cold traps is closed, preventing any additional mixture from entering the fridge. The system then cools using the finite heat capacity of what mash is condensed in the mixing chamber. Gradually the liquid will all boil off and will be pumped away, eliminating the dilution unit's cooling power. This method is advantageous in that there is no additional heat leak due to room-temperature mixture entering the system, but it is disadvantageous because it limits the amount of time available with cooling (and hence experiment time at very low temperatures).

2.1.3.4 Cold Traps

In order to prevent contamination of the mash, the mash is pushed through cold traps before entering the condenser line. The first cold trap is a LN_2 cold trap, which will trap anything which has a freezing point greater than that of LN_2 ($\sim$77K). This includes water vapor, oxygen, and most importantly, oil vapor from the pumps. Oil vapor can and does leak from the outlet of an oil-based mechanical

pump into the mash circuit. In order to prevent oil or these other undesirables from entering the cryostat, a LN_2 trap is needed. The second cold trap is a LHe trap, which will trap anything with a freezing point above that of LHe (∼4.2K). The LHe trap catches mostly H_2, and perhaps a few minor gases. H_2 can wreak havoc on dilution refrigerator. Because H_2 molecules are so small, they can permeate through just about anything; but in addition, H_2 will condense at ∼14K, well above the mash and ^{4}He bath temperatures. Without a LHe cold trap, there is a possibility of H_2 clogging impedance capillaries.

2.1.4 Position Sensor

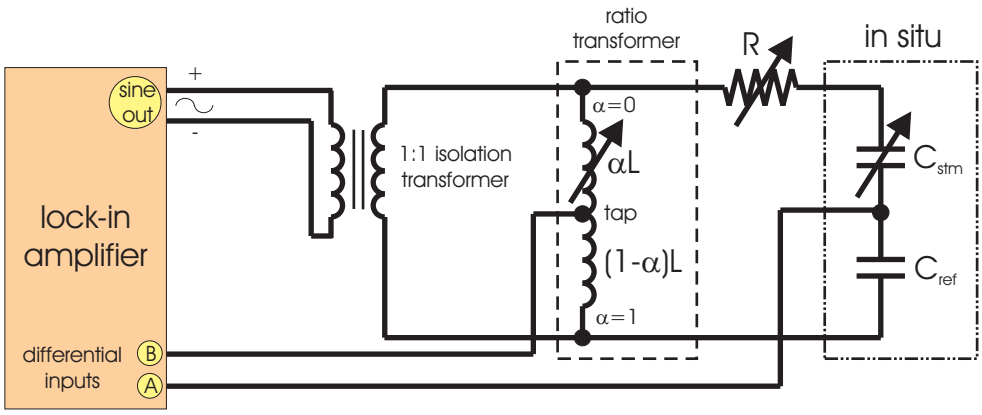

Figure 2.6: Position Sensor Circuit.

It is extremely useful in STM experiments to have the capability to precisely track the position of the STM walker. We use a symmetric capacitance bridge circuit[10] to make this precision measurement.

Two capacitances, in series, are placed in parallel with an inductance with a variable tap location (see Figure 2.6). C_{stm} is the capacitance between two cylinders attached to the STM walker which overlap to a certain degree. As this overlap increases, indicating that the walker is moving closer to the sample, C_{stm}

also increases. The other capacitance C_{ref} is a constant reference capacitance, placed in situ, used merely for voltage balancing the capacitance bridge. The inductance tap is variable, tunable by hand, as is the resistance (R). The tap location effectively creates two inductances, αL and $(1-\alpha)L$, where α is a fraction between 0 and 1. (The total inductance is $\alpha L+(1-\alpha)L = L$.) The two inductances constitute a second voltage balancing point in the circuit at the tap. The circuit is driven simply by a sinusoidal voltage excitation. The ground of the experiment is decoupled from the oscillator (the lock-in amplifier) through the use of a 1:1 voltage isolation transformer.

In effect, both the two capacitances and the two inductances independently form voltage dividers. If the voltage at the top of the circuit (applied sinusoidal voltage) is V_I, then I can write the voltages in the middle of either the two capacitances or the two inductances as voltage dividers using the appropriate reactive impedances of the circuit elements:

$$V_C = \frac{Z_{C_{ref}}}{Z_{C_{stm}} + Z_{C_{ref}}} V_I = \frac{\frac{1}{j\omega C_{ref}}}{\frac{1}{j\omega C_{stm}} + \frac{1}{j\omega C_{ref}}} V_I = \frac{1}{1 + \frac{C_{ref}}{C_{stm}}} V_I \tag{2.1}$$

and

$$V_L = \frac{Z_{(1-\alpha)L}}{Z_{(1-\alpha)L} + Z_{\alpha L}} V_I = \frac{j\omega(1-\alpha)L}{j\omega(1-\alpha)L + j\omega\alpha L} V_I = (1-\alpha)V_I \tag{2.2}$$

where V_C is the voltage between the two capacitances, V_L is the voltage between the two inductances, and j is the unit imaginary number. Here I have neglected the resistance (R) because it is included in the circuit to balance any stray resistances: it should effectively and ideally be canceled away on circuit balance. The voltage difference between the two parts of the bridge, which is measured by the lock-in, is

$$V_{diff} = V_C - V_L = \left[\frac{1}{1 + \frac{C_{ref}}{C_{stm}}} - (1-\alpha)\right] V_I \tag{2.3}$$

C_{stm} is measured by balancing the electronic resonance bridge (i.e. finding the condition in which $V_C = V_L$, or $V_{diff} = 0$). If indeed we have voltage balance, then I find

$$\frac{C_{stm}}{C_{ref}} = \frac{1}{\alpha} - 1 \tag{2.4}$$

For off-balance operations, the sensitivity of the symmetric capacitance bridge to changes in C_{stm} due to STM motion is

$$S_{C_{stm}} \equiv \frac{d(V_{diff})}{d(C_{stm})} = \frac{C_{ref}}{(C_{stm} + C_{ref})^2} V_I \tag{2.5}$$

and the sensitivity of the measurement to changes in the inductance ratio (α) is

$$S_\alpha \equiv \frac{d(V_{diff})}{d(\alpha)} = V_I \sim \frac{5mV_{rms}}{10^{-3}\ change\ in\ \alpha} \tag{2.6}$$

for a typical excitation of the lock-in. If C_{ref} is chosen to be near the middle of our expected values for C_{stm}, then $C_{stm} \approx C_{ref}$, and

$$S_{C_{stm}} \approx \frac{V_I}{4C_{stm}} \sim \frac{5V_{rms}}{4(5nF)} = \frac{1mV_{rms}}{4pF} \tag{2.7}$$

for typical numbers in our setup. Empirical observations and linear response analysis show a roughly linear relationship between the overlap length of the STM's two capacitive cylindrical plates and C_{stm}. However, it is often more convenient to measure V_{diff} as the STM walks and this overlap changes. Figure 2.7 shows a typical measurement of V_{diff} as a function of the number of steps taken by our STM.

2.1.5 Wiring

Most of the signal cables inside the cyrostat are small diameter, stranded stainless steel coaxial cables of approximately 0.8mm in diameter. Shields are made of braided stainless steel.

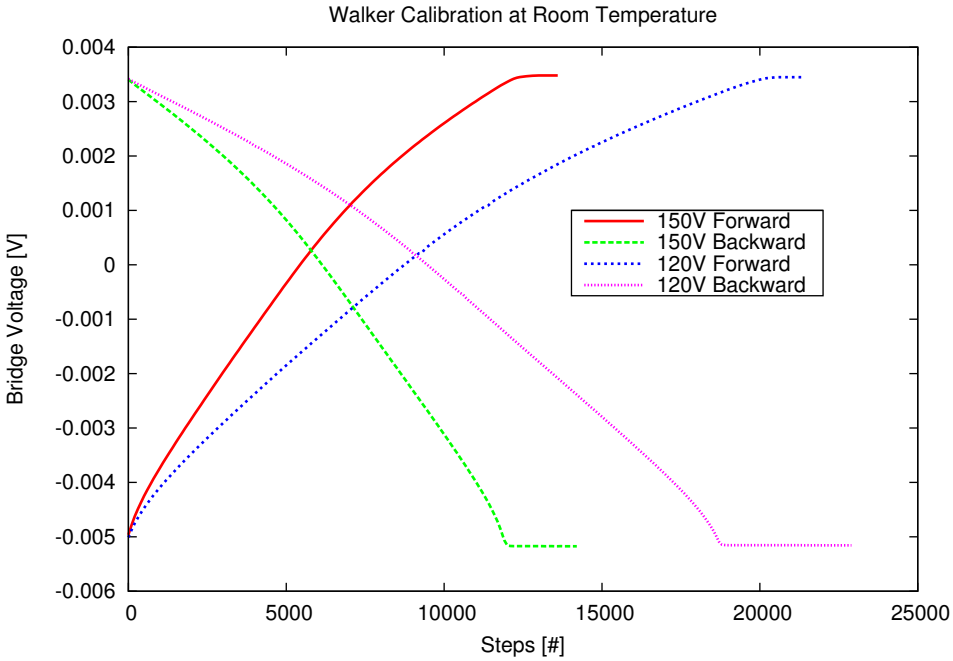

Figure 2.7: Walker Calibration at Room Temperature. Curves for two stepping voltages, 120 V and 150 V, are shown.

All signals are passed through (π) filters (a circuit consisting of two parallel capacitors interrupted in the middle with a series resistor or inductor) at room temperature to prevent any stray RF energy from entering the system and thus removing extraneous noise.

2.1.6 Vibration Isolation

Vibration isolation is essential to many kinds of high-precision physics experiments. In our system, there are several layers of vibration and acoustic isolation which enable a highly sensitive, very low-noise environment.

In the schematic Figure 2.8, the LHe dewar is attached to a Pb filled table weighing approximatley 1.5 tons. The table is suspended on 3 air springs, each of which is attached to a wooden leg filled with roughly 0.5 tons of Pb. The

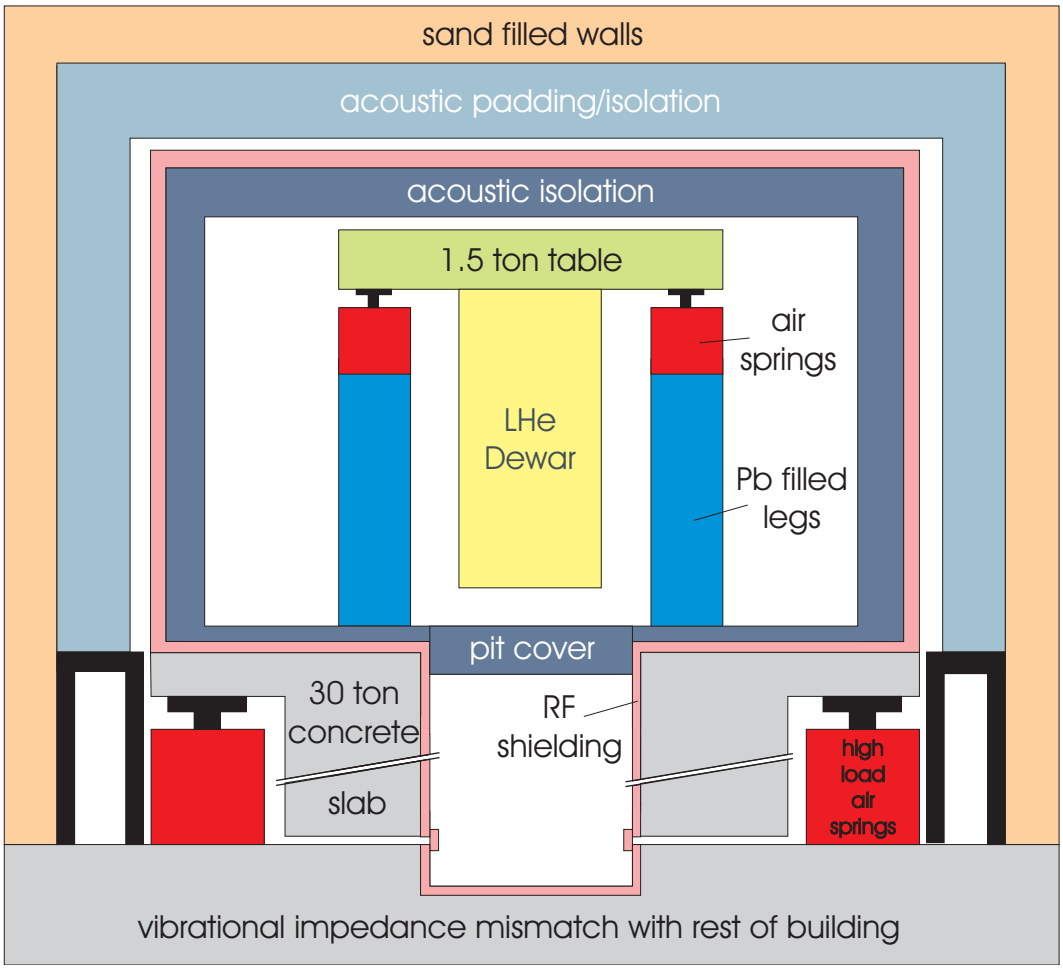

Figure 2.8: Schematic of Vibration, Acoustic, and RF Isolation Systems. Figure is not to scale.

experiment (table, legs, and all) rests on a large, 30-ton slab of concrete which forms the perimeter of the inner experiment room. This inner room is itself floated on larger air springs. Acoustic padding insulates the inner room from extraneous sound, while a Faraday cage insulates the inner room from unwanted RF radiation. The outer room also has acoustic isolation in its interior, as well as exterior walls filled with sand. The entire laboratory rests on a concrete foundation which has a mechanical impedance mismatch with the rest of the building for the purpose of dampening unwanted incoming vibrations.

2.1.7 RF Shielding

To prevent additional electronic noise or heating due to ambient RF radiation from a wide variety of external sources, a Faraday cage was included with the construction of our inner experiment room. The material chosen for the cage is Cu. The wall need not be very thick since the penetration depth of the radiation is very small at RF frequencies. Using[2]

$$\delta = \frac{1}{\pi f \mu \sigma} \tag{2.8}$$

the penetration depth (δ) for Cu at 100MHz, a typical RF frequency (f), is a mere 6.5 μm. The thickness chosen for our room's shielding is about 2 mm, which corresponds to a penetration of the RF shielding thickness for a frequency of about 1 kHz.

2.1.8 8.5 Tesla Magnet

The liquid ^{4}He dewar is equipped with a superconducting toroid coil which has a maximum field of 8.5 Tesla at about 90 A. After a bypass conductive pathway is obstructed through the use of a heat switch, the toroid is slowly energized to the desired $\vec{H}$ field. It is again isolated from the circuit after the heat switch is turned off, allowing the current in the magnet to continue to flow in "persistent mode" even after the source leads are disconnected. Theoretically, the current in the magnet will flow, and the magnetic field will be maintained, indefinitely, as long as the magnet does not "quench". Quenching may occur if any part of the magnet goes from a superconducting to normal state, either by accidentally allowing the magnet to warm or by stochastic fluctuations.

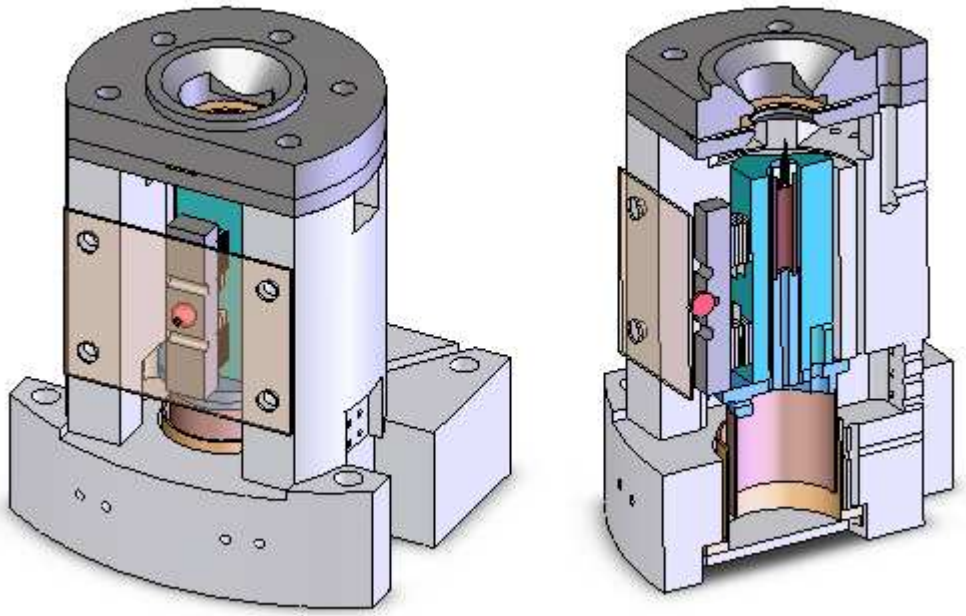

Figure 2.9: STM head. (**Left**) Front view. (**Right**) Sectioned view.

2.1.9 STM Head

The STM head is an S. H. Pan design implementing a stick/slip style of motion produced by shear piezos.[7] The design has been described in earlier scientific instrument publications,[8, 11] and has served as the workhorse in many successful, modern, high-precision STM experiments.[4, 6]

The STM body is made of Macor, chosen because it is easily machinable and because of its high thermal but low electrical conductivity. A highly-polished, sapphire, triangular prism is held tightly in place by 6 shear piezos mounted on the inside walls of the STM. Two concentric cylindrical capacitors, one attached to the walker prism and one attached to the STM body support, form a capacitive sensor which may be measured to determine the position of the walker (see Section 2.1.4).

The STM walker takes one step using a stick/slip static frictional motion. High voltages (∼300 V peak) applied to each these piezos cause them to rapidly shear

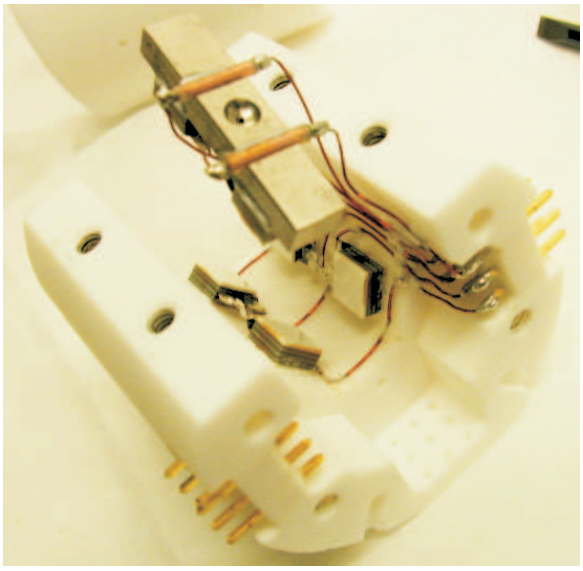

Figure 2.10: STM Head in the Early Stages of Construction

one after another, and then relax evenly in the new position. Each step size is roughly 30 nm, but the size may be tuned by adjusting the tension of a BeCu plate on the front of the STM. The plate pushes against the front piezo mount through a small ruby sphere.

Samples are inserted into the system through a loading chamber at the top of the fridge. They are slowly lowered on a stiff rod, stopping at several places through the insert for both radiative and conductive cooling of the sample. Samples are cleaved at around 18K and are immediately inserted and locked into the STM head (at either 4.2K or $\sim$100mK).

A second BeCu plate acts as a sample bias electrode and a rigid press plate. This plate is circular, affixed to the top of the STM, and has a central hole through which the stud presents the sample to the STM tip. A sample attached to an insertion stud is mechanically pressed against this plate for rigid support, and the constant voltage setpoint bias is applied to this plate. The plate is also bound to the STM stage via an optimized thermal conduction path, providing a good

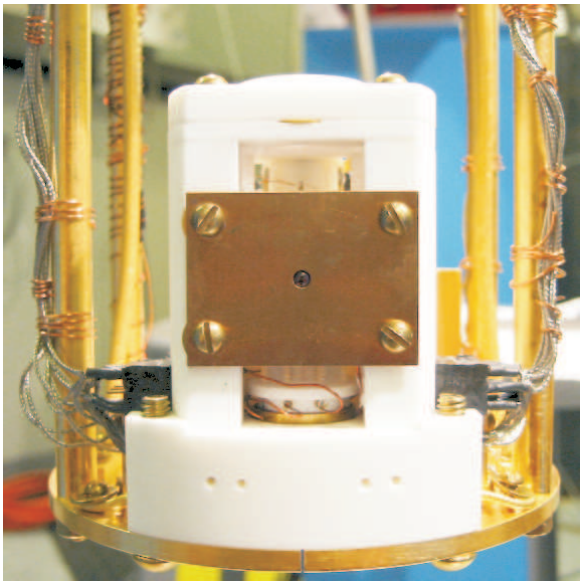

Figure 2.11: STM Head Photograph. The image shows the front view of the STM head, which is mounted on the lowest stage of the cryostat. This STM was constructed by the author.

thermal connection to the low-temperature cryostat.

The STM used in this research was constructed by the author. The anatomy of this particular STM head design is largely as previous described,[3, 5] with few modifications. A full STM head assembly instruction set is included in this dissertation in Appendix B. The material used for the front piezo mount has been changed from Macor to titanium for better mechanical strength with increased tightening of the front BeCu plate.

2.1.10 Laboratory Photographs

Figure 2.12 shows the table suspending the experiment dewar alongside the two panels used for routing gases in and out of the system. Photographs of various critical areas of the experiment, including supporting infrastructure, are shown in Figure 2.13.

Figure 2.12: Experiment Table with Dewar and Gas Panels. This image shows a portion of the interior of the inner acoustic/RF room. On the left of the image, the table suspends the raised dewar on air springs atop three wooden legs filled with Pb. On the right are gas routing systems. A gas panel (blue) routes ^{3}He/^4He gas mixture through cold traps and to the dewar. Further on the right, a waste panel handles ^{4}He boiloff recovery. The wide pipe at the top of the image is the still pumping line for the dilution refrigerator.

Figure 2.13: Various Photos of Experiment, RF/Acoustic Room, and Infrastructure. (**Top-Left Panel**) View from the outer acoustic room inside the inner RF room. The cryostat, at room temperature, hangs from the table with the dewar lowered into the pit. The pit cover can be seen at the lower-left part of the image. (**Top-Right Panel**) The cryostat is seen in the foreground with the mixture and auxiliary gas routing panel in the background. The LN_2 cold trap dewar can be seen to the left of the gas panel. The walls of the pit, covered with a Cu layer for RF shielding, may be seen in the lower part of the image. (**Bottom-Left Panel**) A closer view of the various thermal stages of the cryostat. The different components of the dilution refrigerator are visible. At the bottom of the cryostat sits the STM head. (**Bottom-Right Panel**) Loose, welded, metal bellows and plastic tubes for mixture, ^{4}He, and compressed gases are connected from the control room and pump compartment to the isolated RF/acoustic floating room. All connections are designed to be very loosely connected to minimize vibrational coupling to the room.

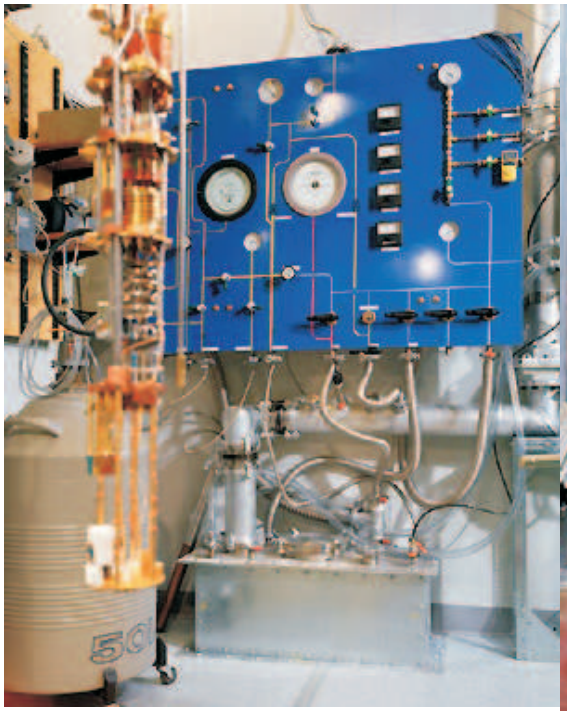

2.2 Measurement Methods

The following sections are technical comments about the methods of obtaining measurements such as described in Section 1.3.

2.2.1 The Topograph

The topograph, as described in Section 1.3.1, is a measure of the feedback calibration of the STM tip height as it is scanned over the sample surface. High voltages control the deflections of a scanner piezo which produces a motion of the tip such that it scans over the sample surface in a grid (see Figure 2.14). The feedback quantity is theoretically proportional to $z(\vec{r}) + z_{const}$, where z_{const} may be nonzero. More importantly, the feedback is a reflection of the variations in $z(\vec{r})$, due to changes in the integrated density of states of the sample, as the tip is scanned across real space. Thus, the topograph typically images atomic/lattice locations, impurities, lattice vacancies, step edges, surface adsorbates, and may sometimes even detect effects due to large spatial changes in the local density of states.

2.2.2 Measuring Conductance Spectra, or $\frac{dI}{dV}$

When taking differential conductance measurements, the a defined setpoint is chosen for a constant current and bias, effectively parking the tip at some immobile tip-to-sample separation above the sample surface. Then, the control circuit is taken out of feedback, and differential conductance spectra can be measured. This is done by varying the bias in a predetermined way and measuring the current response. For each particular energy, the total output of the bias is a predefined constant ($V_{bias}(t)$) plus a higher frequency excitation (ΔV):

$$V(t) = V_{bias}(t) + \Delta V(t) \tag{2.9}$$

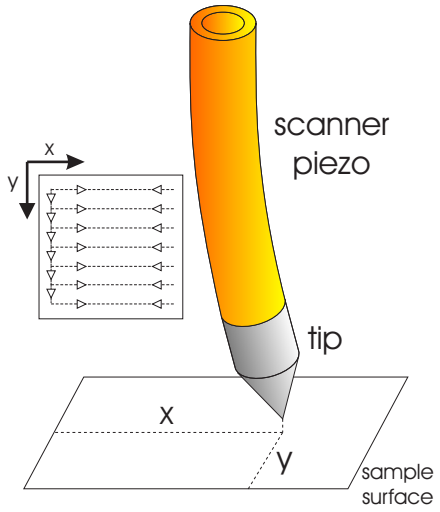

Figure 2.14: Piezo Deflections During Topograph Scanning (Exaggerated). High voltages (up to ±300V) from the ECU control the shape of the scanner piezo and therefore the x and y position of the tip over the sample surface. The bending of the scanner piezo tube is extremely exaggerated. (**Inset**) Top view of the same sample surface showing a trace of the tip position during a topograph scan. Arrows indicate motion of tip apex. Scanning progresses one line at at time, with each line moving forward and backward in the x direction.

The voltage excitation comes from the output of the lock-in amplifier at the chosen reference frequency (f_{ref}) and reference voltage (V_{ref}), measured in RMS volts. Specifically, the form of the excitation is

$$\Delta V(t) = V_{ref} sin(\omega t) \tag{2.10}$$

where $\omega = 2\pi f_{ref}$, and no phase is given because it is defined to be zero. This signal performs the work of actually measuring $\frac{dI}{dV}$ at the particular set bias (V_{bias}). The bias itself changes with time so that different energies can be sampled, but it remains constant on the time scale of one particular $\frac{dI}{dV}$ measurement. Specifically, V_{bias} follows a sort of stair step pattern:

$$V_{bias}(t) = V_{start} + \frac{V_{end} - V_{start}}{N-1} \sum_{k=1}^{N-1} \Theta(t - [t_{start} + \frac{k}{N}(t_{end} - t_{start})]) \tag{2.11}$$

where Θ is the Heaviside unit step function. This function is plotted in Figure

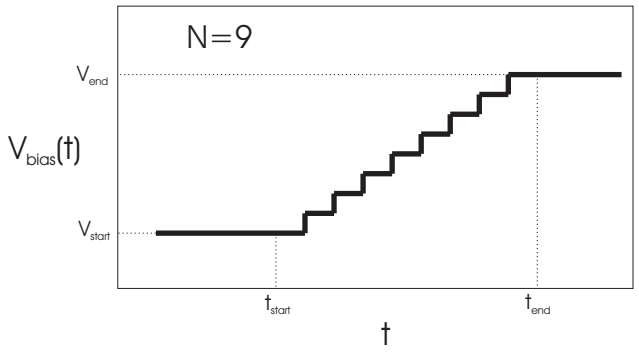

Figure 2.15: Schematic of V_{bias} Step Train.

2.15 so one can see how the voltage bias is ramped during a conductance measurement. The ECU stays at each voltage for a certain period of time $\Delta t = \frac{t_{end}-t_{start}}{N}$ and then continues to the next point. As long as $f_{ref} \gg \frac{1}{\Delta t}$, each "step" on the stairs is effectively constant for one particular energy of the conductance measurement.

For a *single* voltage bias (V_{bias} with no time dependence), the current response to the sinusoidal excitation will be at the same frequency the voltage excitation (and also its harmonics). Specifically, the response will be a Taylor expansion expanded around the point V_{bias}:

$$I(V(t)) = \sum_{n=0}^{\infty} \frac{I^{(n)}(V_{bias})(V(t) - V_{bias})^n}{n!} = \sum_{n=0}^{\infty} \frac{I^{(n)}(V_{bias})(\Delta V(t))^n}{n!} \tag{2.12}$$

explicitly writing the first few terms, we have

$$I(V(t)) = I(V_{bias}) + \frac{dI}{dV}\Delta V(t) + \frac{1}{2}\frac{d^2I}{dV^2}[\Delta V(t)]^2 + \dots \tag{2.13}$$

$$= I(V_{bias}) + \frac{dI}{dV}V_{ref}sin(\omega t) + \frac{1}{2}\frac{d^2I}{dV^2}V_{ref}sin^2(\omega t) + \dots \tag{2.14}$$

where $sin^2(\omega t + \phi)$ can be shown trigonometrically to be proportional to a linear combination of $sin(2\omega t)$, $cos(2\omega t)$, and constants. The excitation ΔV itself is usually a small oscillation on top of the constant V_{bias} once the signal arrives at the experiment, so the second-order term as well as all higher-order terms are negligibly small compared to the zeroth- and first-order terms.

Furthermore, due to the fact that the phase-locked loop (PLL) of the lock-in multiplies input signals by the reference excitation, orthogonal sinusoidal functions average to zero, including all harmonics of the fundamental reference excitation and all out-of-phase signals. This effectively acts as a very narrow pass band filter, which has a frequency centered around f_{ref} by design. (The frequency for the narrow pass band filter can be chosen to be $2f_{ref}$ to correspond to the second-order signal, or $\frac{d^2I}{dV^2}$, but the selected signal is weaker because it is a second order harmonic, and the S/N is poorer. See Section 2.2.4.)

Thus, with the lock-in filtering applied, all terms in 2.14 go away (normally) except the first term. The lock-in also averages its product over a programmed time period to arrive at the final response A_{out} as follows

$$A_{out}(t) = \frac{1}{\tau}\int_{t-\frac{\tau}{2}}^{t+\frac{\tau}{2}} dt' sin(\omega t' + \phi)\left[\frac{dI}{dV}V_{ref}sin(\omega t')\right] \tag{2.15}$$

where ϕ is a the phase offset of the reference voltage relative to the current response phase, which is most often tuned on the lock-in to be zero so that the two signals are in-phase. Performing this integral I find

$$A_{out}(t) = \frac{V_{ref}}{2\tau}\frac{dI}{dV} \tag{2.16}$$

as long as several oscillations occur over the integration period, or $\tau \gg \frac{1}{f_{ref}}$. Hence, the final response (A_{out}), in the simplest case, is fully real and proportional to $\frac{dI}{dV}$.

2.2.3 Choosing a Lock-In Excitation for Differential Conductance Measurements

The essential problem is to measure some physical $\frac{dI}{dV}$ curve which is currently unknown. In reality, this function $\frac{dI}{dV}$ is a *continuous* function of voltage (V_{bias}).

However, since the ECU will be used to measure this continuous function, only a finite number of points can be stored: the ECU will sample only particular points along the real $\frac{dI}{dV}$ curve, corresponding to N distinct energies.

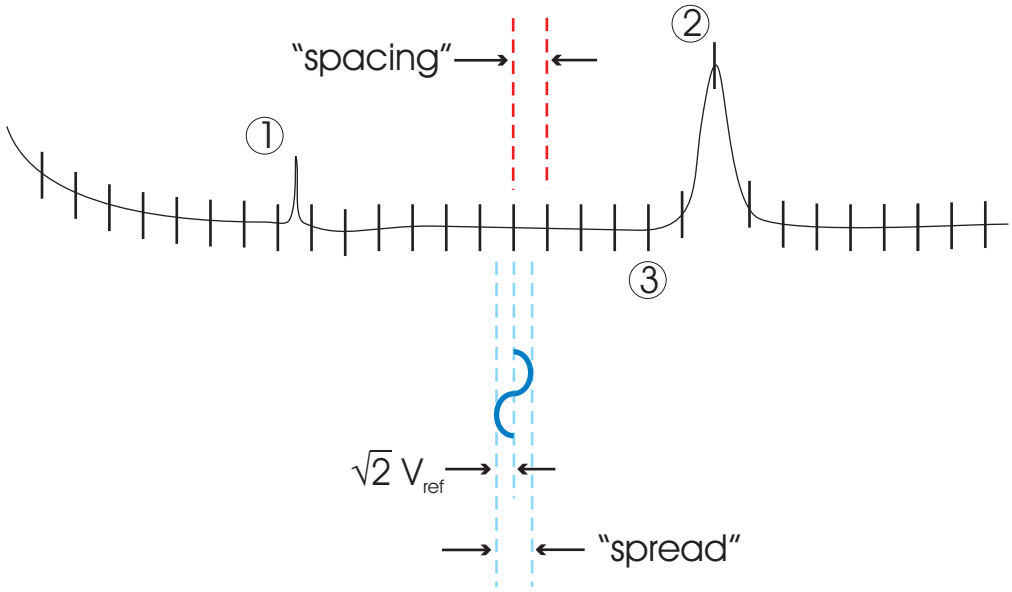

Figure 2.16: Comparison Between Excitation and Resolution Energy Spans. A simulated curve, shown in black, is measured by exciting the system with a lock-in reference excitation (blue curve) at each point, and then sweeping through all points to be measured (short vertical lines). If the voltage excitation is too large, the measurement at point (3) may be contaminated by the large peak at point (2). If the voltage excitation is too small, neither of the measurements at the points on either side of the small peak (1) may find the peak at all.

The ECU uses the constant bias V_{bias} (see Section 2.2.2) to sweep along the function to be measured one point at a time, and it uses the A.C. excitation from the lock-in to "feel around locally" each of those discrete points. Figure 2.16 shows the spread of the excitation in comparison to the span of the energy resolution for a simulated curve. Each vertical line is one discrete point on the curve that will be sampled.

Effectively, the maximum extent of the lock-in excitation denotes the "spread" of the measurement for a particular point. It is this "spread" around each point

which samples the real $\frac{dI}{dV}$ curve in the immediate vicinity of the point to get a final average value. The "spacing" of the sampled curve is space between two finite points on the curve, or the energy spacing.

The "spread" of the reference excitation should be about equal, or slightly greater than, the "spacing" of the discrete curve, defined by V_{bias}, at the STM itself. If the "spread" is too small, then we will miss pieces of the curve we are trying to measure, and we will also suffer from increased noise. If the "spread" is too big, points relatively far away from a feature may measure the feature's presence when they reasonably should not, and points close to the feature will measure areas far away from it where there may be little spectral weight. These effects will result in the feature being smeared, appearing spread out in energy and reduced in height. A good rule of thumb is to have a small overlap between adjacent points, to increase S/N without sacrificing the ability to focus on curve features.

If there are no dividers in the circuit (see Figure 2.1), then the "spread" is simply the peak-to-peak voltage of the lock-in sinusoid, $2\sqrt{2}V_{ref}$, since V_{ref} is always given as an RMS voltage. However, in our system, there is a built-in B:1 divider, where $B = 100$, inside the ECU which divides the reference voltage (ΔV) only, and not the bias (V_{bias}). In addition, a divider (ratio D:1) is often used in the bias circuit for the purpose of decreasing the minimum possible energy spacing. Then, the overall "spread" of the excitation is reduced by these two dividers:

$$"spread" = \frac{2\sqrt{2}V_{ref}}{BD} \tag{2.17}$$

To quantify the energy "spacing" is trivial. It is simply the range of the measurement V_{end} - V_{start}, divided by the number of points (N) minus 1:

$$"resolution" = \frac{V_{end} - V_{start}}{N - 1} \tag{2.18}$$

As indicated, the "spread" should be designed to be about equal to the "spacing". If we set Equations 2.17 and 2.18 equal to each other, then we have

$$\boxed{V_{ref} = \frac{BD}{2\sqrt{2}} \frac{V_{end} - V_{start}}{N-1}} \tag{2.19}$$

for exactly equal "spread" and "spacing".

Instead of exactly matching the "spread" and "spacing", some overlap for the "spread" at each point may be desired. Although one may increase the "spread" by increasing the reference voltage, the factor $\sqrt{2} \approx 1.4$, is a fairly reasonable factor for overlap. Thus, if we simply remove the $\sqrt{2}$ from Equation 2.19, the reference voltage is effectively underestimated, but that underestimation constitutes a useful overlap (and makes the math simpler). In this case (with $\sqrt{2}$ overlap),

$$\boxed{V_{ref} = \frac{BD}{2} \frac{V_{end} - V_{start}}{N-1}} \tag{2.20}$$

This is the main result for selecting a physically reasonable lock-in excitation. In practice, some experimentalists choose reference voltages slightly higher than this number to increase S/N, as discussed in the next section.

2.2.4 Signal-to-Noise Ratio Considerations

The signal-to-noise ratio (S/N) is generally defined as

$$S/N \equiv \frac{P_{signal}}{P_{noise}} \tag{2.21}$$

where P is power. Thereby, if your signal increases by a factor of 2, so does your S/N, and correspondingly, if your noise decreases by a factor of 2, your S/N increases by the same factor. Because the lock-in response is proportional to V_{ref}, as shown in Equation 2.16, we may expect the S/N to increase by a factor of 4 if we double the reference voltage. The signal-to-noise improvement (SNRI) is then

$$SNRI \equiv \frac{S/N^{new}}{S/N^{old}} = \left(\frac{V_{ref}^{new}}{V_{ref}^{old}} \right)^2 \tag{2.22}$$

Accordingly, increasing V_{ref} is always a good idea to increase S/N, if there is physical justification to do so.

As an aside, in STM experiments, one may also increase the meaningful signal by increasing the magnitude of the tunneling current. This is achieved by either increasing the current setpoint or decreasing the voltage bias (usually the former, since bias is physically meaningful as the electronic excitation energy). This results in a SNRI of

$$SNRI = \left(\frac{I^{new}}{I^{old}}\right)^2 \tag{2.23}$$

Finally, the (white) noise level from the experiment can be reduced by averaging many samples of the same measurement over an extended period of time. This averaging can be performed via the lock-in time constant, or by extending the time allocated to measure each point, for example by increasing τ in Equation 2.11. Since time plays the role of the number of samples in ordinary statistical averaging theory, the normal statistical confidence interval is is proportional to $\frac{1}{\sqrt{T}}$, where T is the averaging time. Hence, the SNRI in this case is

$$SNRI = \left(\frac{\text{noise power}^{old}}{\text{noise power}^{new}}\right)^2 = \left(\frac{\frac{1}{\sqrt{T^{old}}}}{\frac{1}{\sqrt{T^{new}}}}\right)^2 = \frac{T^{new}}{T^{old}} \tag{2.24}$$

2.2.5 Tip Preparation and Qualification

Tip preparation refers to the processes necessary to bring the tip into a state suitable for scanning and tunneling. In general, a metallic tip is covered with a (relatively) thick layer of oxide after being exposed to air and oxygen for any brief period of time. The oxide must be removed in situ via field emission, which is a process in which high voltages (20-100V) are applied across the tip/bias junction, causing large currents (10nA-5μA) to flow across the junction. This somewhat

violent procedure often causes dramatic changes to the STM tip, even causing a relatively large piece of the tip apex to break off. The breakage ensures that the aforementioned oxide layers are removed in situ.

In addition to breakages, field emission can also be used to modify the tip in a variety of ways by varying the voltages applied to the junction and the tip-sample distances. With patience, a tip suitable for STM work can be acquired. The following is a list of requirements for tips prepared by field emission on Au to be used in our experiments.

1. *No multi-stable tips.* Often, the current from STM tips may fluctuate between 2, 3, or more different values, even when held at a constant feedback position. This usually indicates that the tip is in a physically multi-stable state, possibly caused by continuous reconfigurations of the particles near the tip apex.
2. *Good stability.* Tips must not change during the course of measuring several topographs. Unstable tips are not so useful.
3. *No blunt tips.* The ability to resolve finer features ($\sim$1nm) is good. However, it is often difficult to tell if a tip resolves fine enough features on a Au surface.
4. *Flat $\frac{dI}{dV}$ spectra.* Because Au is metallic, it should have a flat density of states as a function of energy for a single point spectra, especially within $\pm$2V.
5. *Reasonable workfunction (Φ) measurements.* Workfunction values of $\sim$3-7eV should be found on Au (see Section 1.3.3).
6. *No tip anisotropy.* Sometimes, a tip will pick up more spectral weight in one direction relative to the orthogonal direction, or features on the sample surface will seem to be stretched in one direction. This is often difficult to tell on a surface of Au, but can easily be seen on a well-known periodic lattice such as that of HOPG or $NbSe_2$.

7. *No multiple tips.* A multiple tip may tunnel into the surface states via several locations near the tip apex, resulting in images on a topograph which appear repeated.

Even if all the above requirements are met for a single tip (which can be difficult), it is still no guarantee that a quality tip will be present upon the approach of a well-cleaved sample surface. In this sense, the success of any single field emission process remains a somewhat unpredictable event.

BIBLIOGRAPHY

[1] D. S. Betts. *An Introduction to Millikelvin Technology.* Cambridge University Press, Cambridge, 1989.

[2] D. J. Griffiths. *Introduction to Electrodynamics, 3rd Ed.* Prentice Hall, Inc., Upper Saddle River, NJ 07458, 1999.

[3] E. Hudson. *Investigating High-T_C Superconductivity on the Atomic Scale by Scanning Tunneling Microscopy.* PhD thesis, University of California at Berkeley, 1999.

[4] Y. Kohsaka, C. Taylor, K. Fujita, A. Schmidt, C. Lupien, T. Hanaguri, M. Azuma, M. Takano, H. Eisaki, H. Takagi, S. Uchida, and J. C. Davis. An intrinsic bond-centered electronic glass with unidirectional domains in underdoped cuprates. *Science*, 315:1380, 2007.

[5] K. Lang. *Scanning Tunneling Spectroscopy Study of Inhomogeneity, Granularity, and Segregation in the Electronic Structure of $Bi_2Sr_2CaCu_2O_{8+\delta}$.* PhD thesis, University of California at Berkeley, 2001.

[6] K. McElroy, D.-H. Lee, J. E. Hoffman, K. M. Lang, J. Lee, E. W. Hudson, H. Eisaki, S. Uchida, and J. C. Davis. Coincidence of checkerboard charge order and antinodal state decoherence in strongly underdoped superconducting $Bi_2Sr_2CaCu_2O_{8+\delta}$. *Physical Review Letters*, 94(19):197005, 2005.

[7] S. H. Pan. Piezo-electric motor. International Patent publication No. WO 93/19494 (International Bureau, World Intellectual Property Organization), 30 September 1993.

[8] S. H. Pan, E. W. Hudson, and J. C. Davis. ^{3}he refrigerator based very low temperature scanning tunneling microscope. *Review of Scientific Instruments*, 70:1459–1463, 1999.

[9] F. Pobell. *Matter and Methods at Low Temperatures, 2nd Edition.* Springer-Verlag, Germany, 1996.

[10] R. C. Richardson and E. N. Smith. *Experimental Techniques in Condensed Matter Physics at Low Temperatures.* Addison-Wesley, Reading, Massachusetts, 1998.

[11] C. Wittnevena, R. Dombrowski, S. H. Pan, and R. Wiesendanger. A low-

temperature ultrahigh-vacuum scanning tunneling microscope with rotatable magnetic field. *Rev. Sci. Inst.*, 68:3806–3810, 1997.

Chapter 3
Cuprate Basics and Underdoped Cuprates

The discovery in 1986 of high-T_C superconductivity by Bednorz and Müller at IBM, Zürich (perhaps coincidentally only a half-decade removed from development of the STM at same research laboratory), enabled scientists around the world to consider the new phenomenon in the light of its unlikely manifestation: that of somewhat complex, layered, ceramic compounds.[8] The purpose of this chapter is to briefly describe basic properties, historical evidence, and theories regarding both early and modern cuprate superconductors. I will also discuss the doping evolution of underdoped cuprates and why the electronic phases associated with them remain somewhat mysterious.

3.1 Resistivity

There are characteristic differences between the resistivity curves of conventional metals, conventional (non-cuprate) superconductors, and high-T_C superconductors. Here I will describe these differences qualitatively.

3.1.1 Conventional Metals

The resistivity (ρ) of conventional metals follows Fermi Liquid theory behavior. Electron quasiparticle scattering from phonons (electron/phonon), other electron quasiparticles (electron/electron), and lattice or defect impurities (electron/defect) all contribute to the resistivity. However, whereas electron and phonon scattering are temperature dependent, impurity scattering is not, meaning that an resistivity offset will exist at all temperatures, even T=0K. A theoretically pristine, defect-free

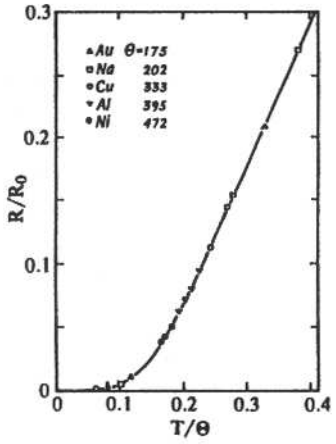

Figure 3.1: Measured Resistivity of Various Conventional Metals and BCS Superconductors.[9, 11]

sample would have no impurity contribution to the resistivity, and the resistivity would extrapolate to zero at T=0K. Moreover, real samples always have some impurities, and the $T\sim$0K resistivity offset can be considered a way to characterize the density of defects in a sample. Figure 3.1(A) shows the resistivity of several metallic elements. At low temperatures ($T \ll \Theta_D$, the Debye temperature), the behavior follows the so-called "Bloch-T^5" law:[2]

$$\rho(T) \sim T^5 \tag{3.1}$$

3.1.2 Conventional Superconductors

The resistivity of conventional superconductors drops to zero at a superconducting transition temperature known as T_C. In theory, the resistivity demonstrates its expected normal statebehavior for temperatures greater than T_C, but abruptly drops to zero at T_C and remains zero for all lower temperatures. Figure 3.2(A) shows data from the original discovery of superconductivity in 1911,[25] and Figure 3.2(B) shows later measurements from some Type II conventional superconductors. This zero-resistivity behavior is described well by BCS theory.[5, 6]

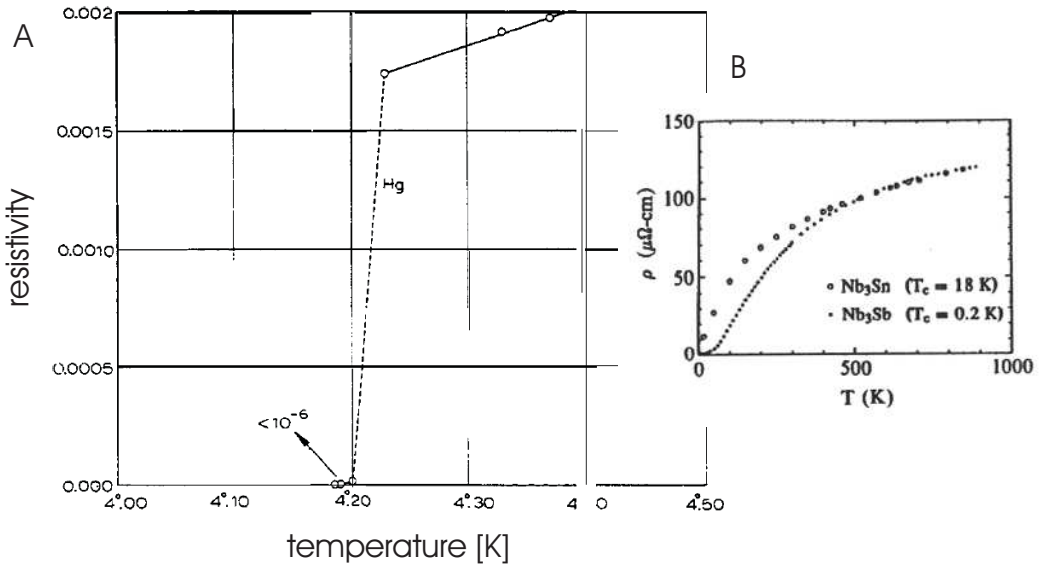

Figure 3.2: (**A**) Original Discovery of Superconductivity by Onnes.[25] (**B**) Two resistivity curves of conventional, but Type II, superconductors.[9]

3.1.3 High-T_C Cuprate Superconductors

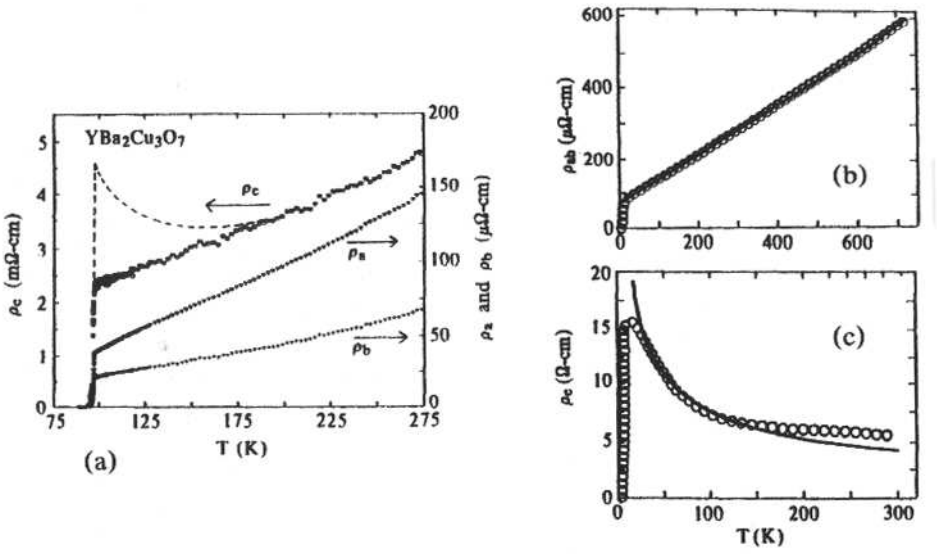

Figure 3.3: Measured Resistivity of Various Cuprate Superconductors. (**Left**) YBCO Resistivity in the three crystallographic directions. $\rho_a \neq \rho_b$ due to anisotropy caused by Cu-O "chains" in YBCO.[9, 12] (**Right**) Resistivities of 2-Bi cuprate compounds, such as BSCCO.[9, 21]

The resistivity of the cuprate superconductors is somewhat different than that of conventional superconductors, but really only in two major ways. First, T_C for the cuprate superconductors is typically higher than that of the conventional superconductors. As of this writing, the highest known T_C for the cuprates is ∼4-5 times higher than the highest of the conventional (BCS) superconductors. Second, due to the geometry of the cuprate compounds, which are sheets of interpentrating layers of CuO_2 planes and buffer layers (see Section 3.2), there is anisotropy between the conductivity along the c-axis (ρ_c) and along either the a- or the b-axes (ρ_{ab}). YBCO breaks further symmetry because it also has "chains" of Cu-O which run along one of the a- or b-axis directions.[9] Examples of resistivity curves showing these anisotropies in the cuprates are shown in Figure 3.3.

3.2 Crystal Structure and Doping

High-T_C cuprate superconductors have a variety of crystal structures. The only general chemical commonality between cuprate compounds is the presence of one (or several) CuO_2 planes per unit cell, although many different cuprates can be formed using the same constituent elements. Cuprates can be thought of as being constructed by stacking these CuO_2 layers alternately with relatively insulating buffer layers that are unique to each compound. The two materials studied in this dissertation, BSCCO and NaCCOC, both have well-understood crystal definitions and symmetries.[9, 13]

BSCCO is a popularly studied cuprate superconductor. BSCCO compounds belong to a crystal structure family with formulation $A_2Sr_2Ca_{n-1}Cu_nO_{4+2n}$, where A can be a variety of elements, but Bi is commonly used. The parameter n denotes the number of CuO_2 layers present per unit cell. The particular material studied in this dissertation has two CuO_2 layers per unit cell, and the formula-

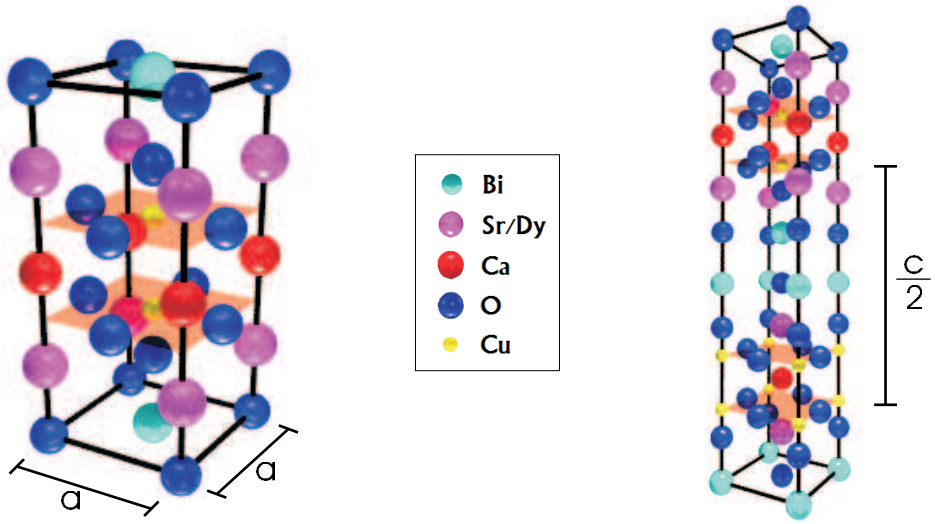

Figure 3.4: Crystal Structure of BSCCO. The identities of atomic constituents are indicated in the inset. Each atom's size is chosen as a fraction ($\frac{2}{5}$) of the atomic radius[28] size. (**Left**) Primitive Cell of BSCCO. Two types of blocking layer are BiO and SrO. BSCCO is doped by substituting Dy for Sr, or by introducing O atoms at interstitial locations. The CuO_2 layer is emphasized with a tan sheet. There are two CuO_2 layers per primitive cell. The Bravais vector for the primitive cell is ($\frac{a}{2}$,$\frac{a}{2}$,$\frac{c}{2}$). (**Right**) One choice for unit cell of BSCCO. It is constructed by duplicating the primitive cell, shifting it (with circular boundary conditions) by ($\frac{a}{2}$,$\frac{a}{2}$,0), and translating it by (0,0,$\frac{c}{2}$).

tion is $Bi_2Sr_2Ca_1Cu_2O_8$, with $n = 2$. This compound is commonly referred to as "Bi2212", or simply "BSCCO" (without referencing n). A form of this crystal structure is seen in Figure 3.4. Like many other members of high-T_C families, Bi2212 may be doped in two ways: Substitutional doping, which is usually performed during sample growth, and additional oxygen doping, which may be performed in an annealing furnace after sample growth. Substitutional doping is usually performed by replacing ^{2+}Ca ions with a dopant ion, but ^{2+}Sr ions may also be replaced. In the case of this dissertation, ^{+3}Dy is the dopant ion, with a doping fraction of x. Independently, oxygen doping may be performed to increase the oxygen population by a fraction of δ. The net formulaic representation is

$Bi_2Sr_2Dy_xCa_{1-x}Cu_2O_{8+\delta}$, and the net doping ($p$), the empirical quantity, is some function (η) of x and δ, where η is some yet undetermined function which likely varies depending on the particular high-T_C family in question.

$$p = \eta(x, \delta) \tag{3.2}$$

I will henceforth refer to this formulation as simply "BSCCO with a doping of p".

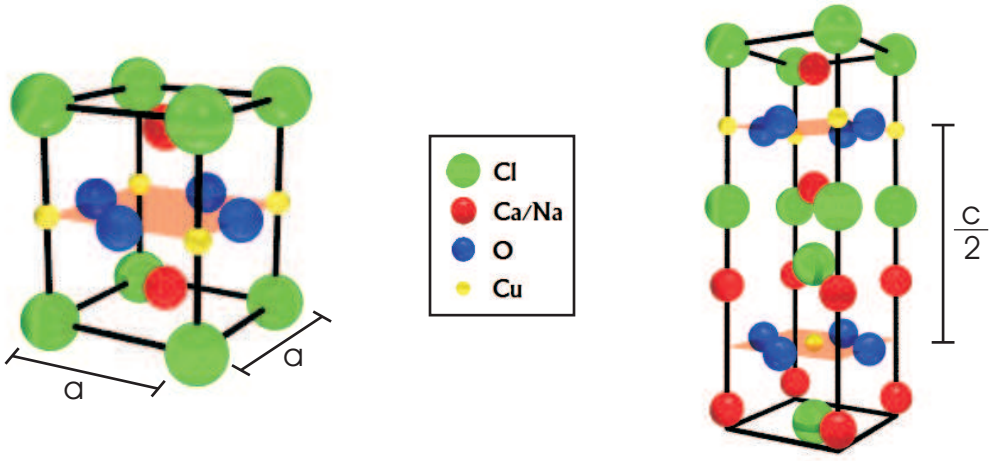

Figure 3.5: Crystal Structure of NaCCOC. The identities of atomic constituents are indicated in the inset. Each atom's size is chosen as a fraction ($\frac{2}{5}$) of the atomic radius[28] size. (**Left**) Primitive Cell of NaCCOC. The Blocking layer consists of Cl and Ca. CCOC is doped by substituting Na for Ca. The CuO_2 layer is emphasized with a tan sheet. There is one CuO_2 layer per primitive cell. The Bravais vector for the primitive cell is ($\frac{a}{2}$,$\frac{a}{2}$,$\frac{c}{2}$). (**Right**) One choice for unit cell of NaCCOC. It is constructed by duplicating the primitive cell, shifting it (with circular boundary conditions) by ($\frac{a}{2}$,$\frac{a}{2}$,0), and translating it by (0,0,$\frac{c}{2}$).

NaCCOC is a newer cuprate superconductor. CCOC, or "oxychloride", compounds share a crystal structure with the A_2CuO_4 family, with one exception: O atoms in the blocking layer are replaced by Cl atoms.[17] In the formula, A is usually La or Sr, but in the case of this dissertation, A is Ca, which may be replaced via substitutional doping of Na with fraction x. A form of this crystal structure is seen in Figure 3.5. The net chemical formula for the compound is $Ca_{2-x}Na_xCuO_2Cl_2$,

and the total empirical doping (p) is thus, simply,

$$p = x \tag{3.3}$$

I will henceforth refer to this formulation as simply "NaCCOC with a doping of p".

3.2.1 Shorthand

"UDXY" will refer to an underdoped cuprate (usually BSCCO) with a T_C of XY.

3.3 Sample Growth

High-quality BSCCO samples are usually grown with a floating-zone method. This method uses a mirror furnace to superheat a small volume of space through which a seed crystal is slowly pulled. The heat allows the compound to become fluid-like and the atoms and ions inside to become mobile. Upon cooling, the BSCCO sample will then crystalize into a lowest-energy configuration, a lattice.[14, 33] The BSCCO samples studied in this dissertation were provided by the S. Uchida group.

The more recently synthesized NaCCOC is created in a capsule which is excited by very high pressures (GPa). The pressure acts as the catalyst which forces the material to crystalize. Stochiometric ratios of different elements and compounds are added to the capsule before its pressurization, which must be controlled precisely in order to avoid contamination due to uncombined ions.[3, 4, 15] The NaCCOC samples studied in this dissertation were provided by the H. Takagi group.

Samples may also be grown using MoCVD and MBE, but such samples were not studied during the course of this research.

3.4 Magnetic Susceptibility

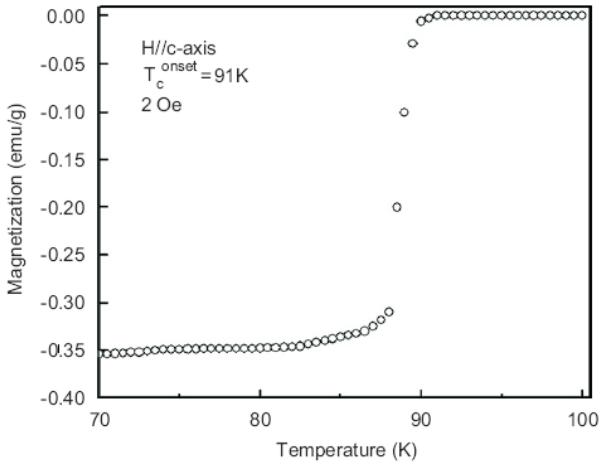

Figure 3.6: Typical Magnetization Curve for a Cuprate Crystal. The BSCCO crystal measured here was grown using similar methods to the BSCCO crystals studied in this dissertation.[33]

In the normal state, cuprates are generally nonmagnetic or trivially magnetic. As temperature is lowered, however, the superconducting state emerges, along with the Meissner effect.[32] The sample must then take on a nonzero magnetization (susceptibility) in order to expel magnetic flux. Figure 3.6 shows a typical magnetization curve for a BSCCO sample grown using similar methods as the samples studied in this dissertation.[33]

3.5 Phase Diagram

The phase diagram of the high-T_C cuprate compounds is interesting to both theorists and experimentalists because of the richness of mysterious phases.[10, 19] On the left of the diagram in Figure 3.7, at low temperatures and doping, the cuprates are nominally half-filled and exhibit a low-entropy spin order resulting in antiferromagnetism. Here, energetic competition on the microscopic scale determines a Mott

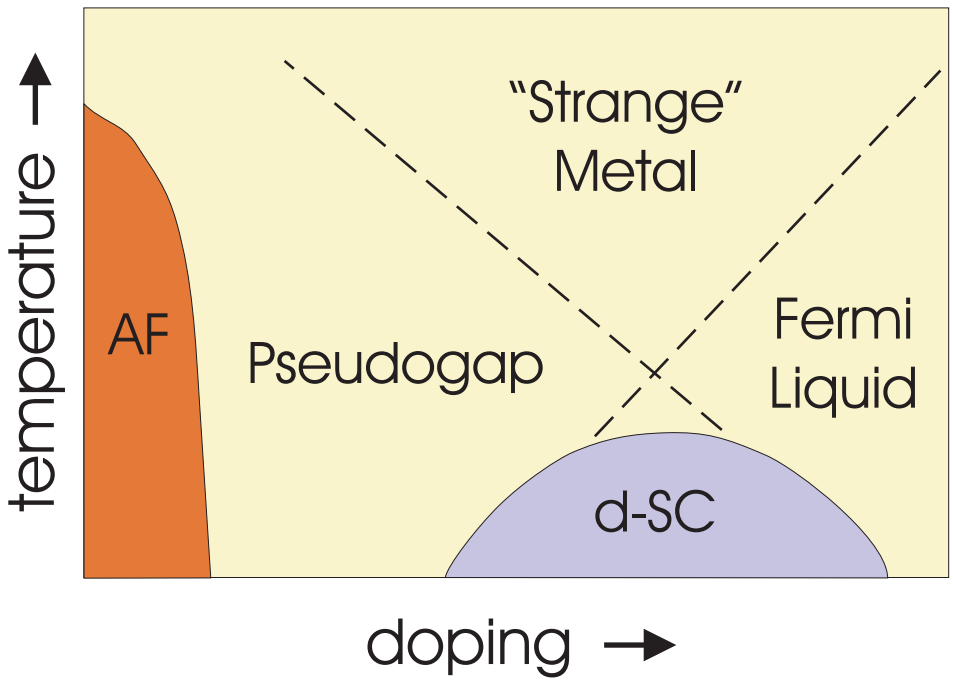

Figure 3.7: Generalized phase diagram of the cuprate superconductors. At zero to low hole doping, the microscopic state is an antiferromagnet, but with increased doping, the phase changes to a d-wave superconductor at very low temperature. These known phases appear to be separated by lesser understood phases at intermediate and high doping, or for higher temperatures.[22]

insulator (see Section 3.7). As doping is slightly increased, the system gradually leaves the Mott insulator phase and enters a lesser understood "pseudogap" phase (see Section 3.8), which part of this dissertation endeavors to understand. Further increasing doping results in a phase transition into the d-wave superconducting state, in which Bogoliubov quasiparticles dominate and superconducting pairing is possible. There is an optimum doping level for which the maximum T_C of samples is defined. Above this point, the cuprate has some metallic properties, but does not appear to be a Fermi liquid.[1, 16] Finally, to the right of the supercondcting "dome", more canonical normal (Fermi liquid) metal behavior is seen, although even here some properties do not behave as proper Fermi liquid substances, such as the transition metals.

3.6 d-Wave Superconductivity

Cuprate superconductors have been assumed to have d-wave symmetry for some time, being demonstrated by a wide variety of different probes, including SQUID.[34] and ARPES measurements.[29] This is somewhat of a surprising result since, theoretically, the a- and b-axis directions in cuprates should be equivalent; but d-wave symmetry gives a Ginsberg-Landau wavefunction that changes sign upon rotations by $\frac{\pi}{2}$. However, although these sign changes do alter the quasiparticle density somewhat, the density itself does not break 2-fold rotational symmetry.

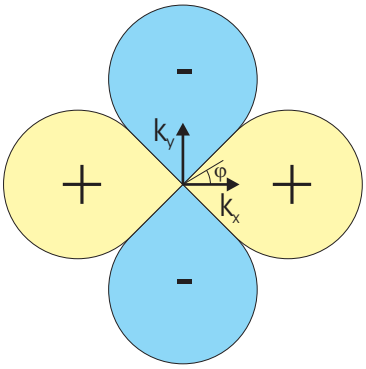

Figure 3.8: Angular Dependence of D-Wave Order Parameter. $\Delta(\phi)$ is shown in polar coordinates. The origin is located in the center of the figure.

D-Wave symmetry specifies a 2-fold rotationally symmetric order parameter. It is generally expected, due to cyclic boundary conditions and a desire for simplicity, that smoothly-connected functions are the best choice to parameterize the angular variation in the order parameter. For a graphical representation of the order parameter, see Figure 3.8.

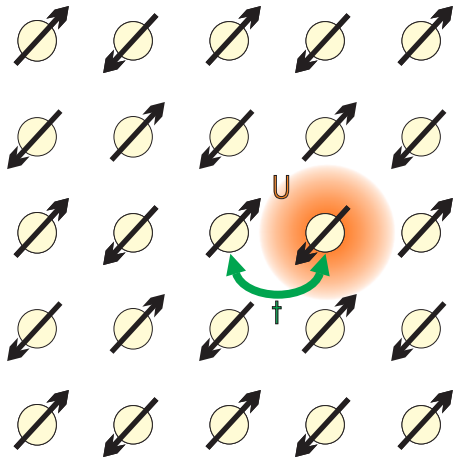

Figure 3.9: Schematic of Antiferromagnetic Néel order. Each site is occupied by one electron, with a spin, at half-filling. The spins alternate as either lattice direction is traversed. The state is a Mott insulator due to the fact that Coulomb repulsion (U) is stronger than the hopping integral (t).

3.7 Antiferromagnetic Mott Insulator as "Parent" State

Cuprate compounds which have a d-wave superconducting phase also exhibit an antiferromagnetic phase low doping ($p <\sim 0.05$, depending on the compound). Certainly at $p = 0$, the state is antiferromagnetic, and the microscopic electronic structure displays Néel[24] order, shown in Figure 3.9. The simplest Néel order schematic is an square lattice half-filled with electrons, constituting one electron per site. Each electron has a spin, and for any particular site, nearest-neighbor spins oppose the spin of that site. This arrangement constitutes the antiferromagnetic nature of the state, since the coarse-grain averaged magnetization has a net spin contribution of zero.

Furthermore, Néel order antiferromagnets are also insulators. This is a somewhat surprising result, since the states are half-filled. The theory of correlated insulator was worked out by Mott,[23] and it is applicable to antiferromagnets. Electrons at one site may hop (energy cost t) to the nearest neighboring site without violating the Pauli exclusion principle, but because there is also a Coulomb repul-

sion (energy cost U) between the two electrons, this behavior may be prevented. For large U, the t-J model can also be used to describe the Mott insulator, with the parameter $J \sim \frac{t^2}{4U}$.

Because the antiferromagnetic Mott insulator is the state from which high-T_C superconductivity emerges in the cuprates as doping is increased, it is reasonable to consider that it may also be the parent state for the superconducting order. In other words, it has been hypothesized that by adding dopants (holes) into the Néel order picture, it might be possible to find a general theory, in which the Mott insulator is a limiting case, which describes the superconductor-to-insulator transition. For this reason, it has recently been crucial scientifically to study compounds doped near this transition in order to explore the physics between the antiferromagnetic and d-wave superconducting states, in the region of the pseudogap.

3.7.1 Measured Gap Properties

Peaks symmetric about the Fermi energy are found commonly in BSCCO spectra, especially at near-optimal doping. These peaks are often called "coherence" peaks because it is believed that they are a direct measure of the superconducting gap, and thus the order parameter of superconductivity. If so, BCS physics explains the emergence of the gaps as spectral weight shifts away from the Fermi energy and into these large peaks as the superconducting phase is entered. However, this cannot be the entire story, and I will describe a few inconsistencies with BCS in the next section.

Since spectra can be measured for each point on a topograph, or 2D grid of points, it is possible to produce a "gapmap", which is an image of the gap magnitude at each one of these points. Such a map is shown in Figure 3.10,

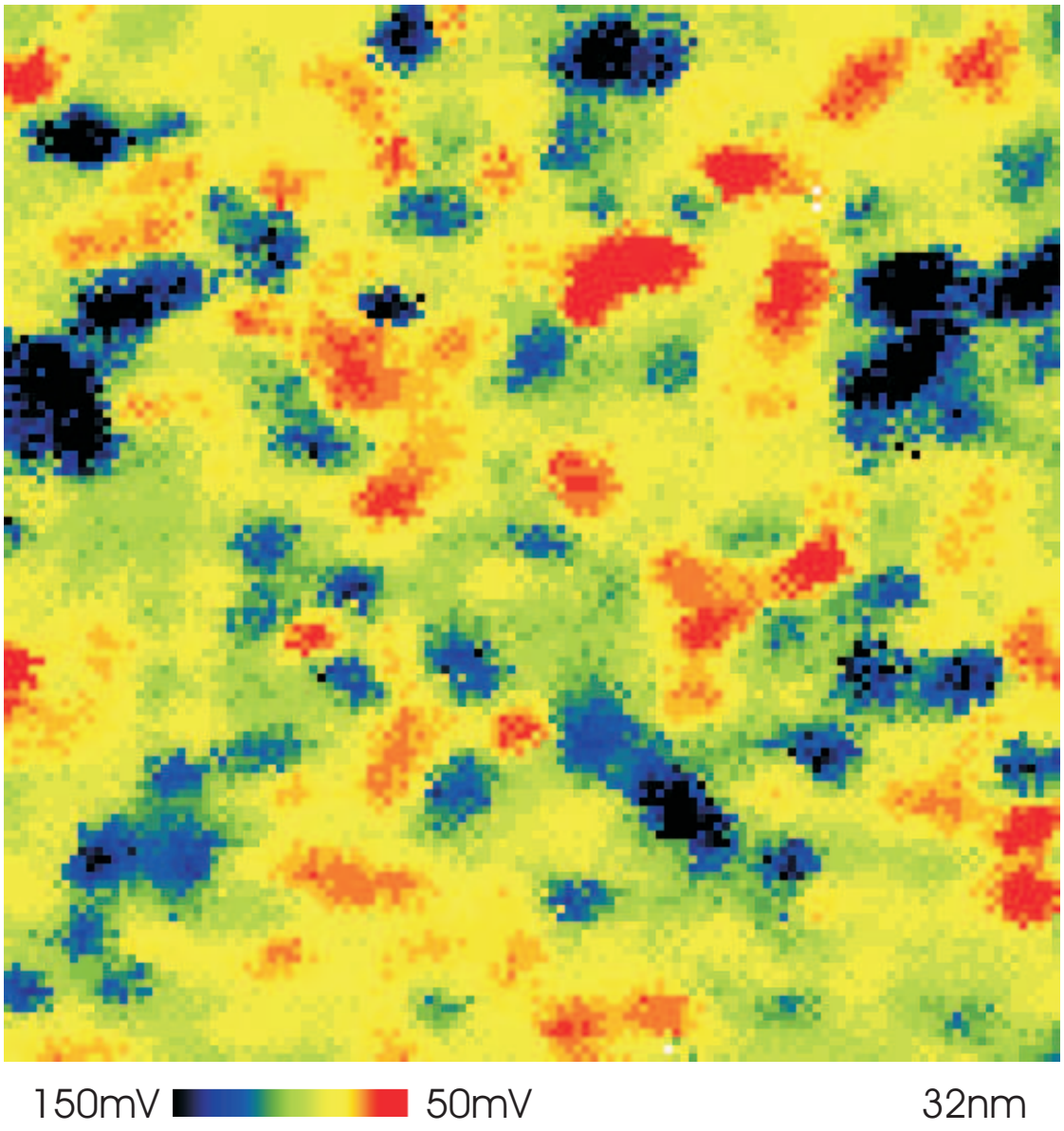

Figure 3.10: Example Gapmap: UD45 BSCCO. Gapmap was created using a 3 of 5 peak finding algorithm. The most common gap value, according to the histogram, is about 85mV for UD45. The map shows spectral inhomogeneity[18] among gap values. The size of the map is 32nm×32nm.

along with its associated topograph, for UD45. Using statistics on the gapmap, it is possible to describe qualities of the distribution of spectra across the sample surface. It is also interesting to note that, while these distributions are generally

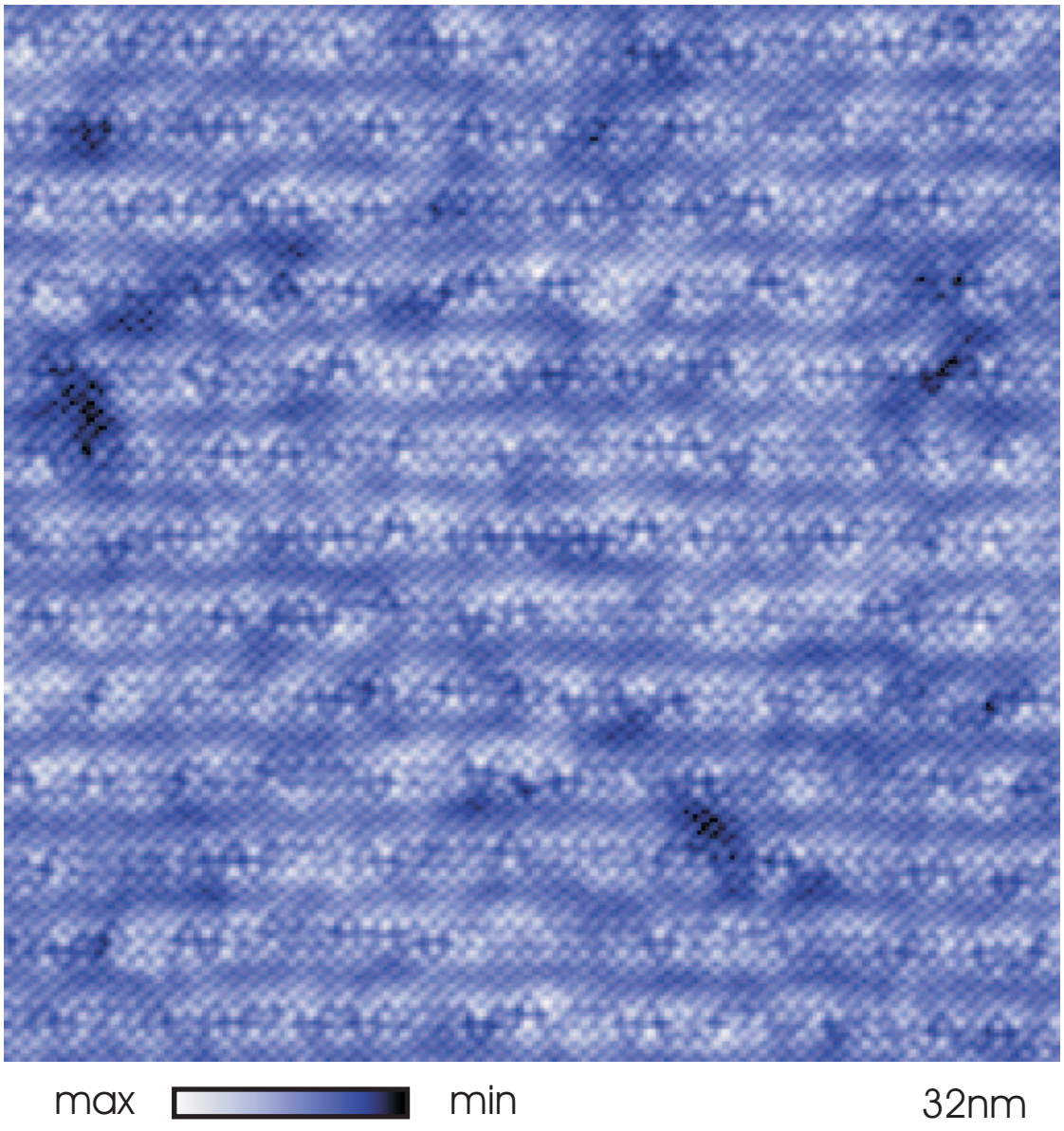

Figure 3.11: Associated Gapmap Topograph, UD45 BSCCO. Associated topograph taken in the same field of view as the previous gapmap.

well-behaved and manifest themselves as Gaussian or Lorentzian forms, spatial inhomogeneity exists across the sample. In particular, a single spectra may have a neighboring spectra which is dramatically different, both in gap magnitude and general shape. (Neighboring spectra are usually separated by only a small fraction

Figure 3.12: Spectra Averaged Around Most Common Gap Magnitude. Each spectrum represents at least 1000 spectra, taken over the sample surface, which have gap values within about 1 standard deviation, in energy, of the most common gap magnitude. For each spectrum, the bounding curves denote the standard deviation, in amplitude, between these selected spectra. The most common gap magnitude is found by performing a 3 of 5 peak finding algorithm on all spectra, binning the gap magnitude results into a histogram, and finding the peak of the Gaussian or Lorentzian in the histogram. Both the average and standard deviation curves have been normalized by a constant factor such that different average spectra are visually comparable.

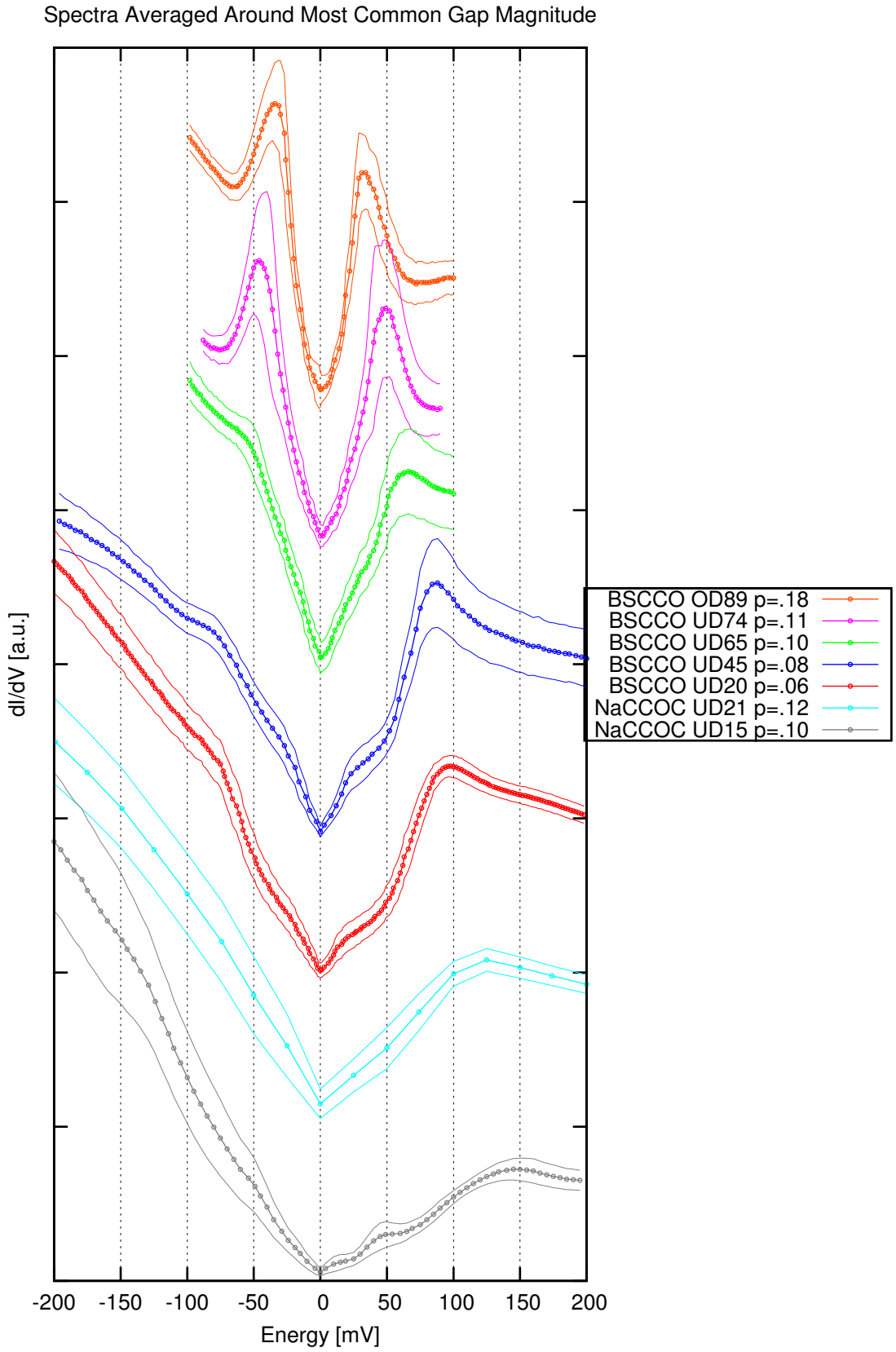
Spectra Averaged Around Most Common Gap Magnitude
dI/dV [a.u.]
Energy [mV]
-200
-150
-100
-50
0
50
100
150
200
BSCCO OD89 p=.18
BSCCO UD74 p=.11
BSCCO UD65 p=.10
BSCCO UD45 p=.08
BSCCO UD20 p=.06
NaCCOC UD21 p=.12
NaCCOC UD15 p=.10

of a lattice constant (a_0).)

Figure 3.12 shows average spectra for several BSCCO and NaCCOC samples measured in our laboratory. The spectra have been averaged around the most common (the mathematical mode) gap value as measured by a 3 of 5 peak finding algorithm. Spectra averaged are taken within around 1 standard deviation of the most common gap value. Note the gradual evolution of the gap peaks as doping and/or T_C is decreased, a behavior which extends to underdoped superconducting samples and even may extend into the pseudogap regime of the phase diagram.

3.8 Pseudogap

The so-called "pseudogap" regime is given the designation because a variety of experimental probes, including e.g. STM and ARPES, find a gap in the measured spectral density in this region, which is *outside* of the nearby superconducting dome in the phase diagram (see Figure 3.7). Because the measured gaps are nominally associated with the superconducting phenomenon, which is the behavior expected from BCS theory, the fact that a gap exists at all in the underdoped regime raises basic questions about our understanding of superconductivity.

3.8.1 What About the Phase Transition and Order Parameter?

Early studies have revealed a transition with temperature into the pseudogap regime through changes in magnetic susceptibility, coefficient of linear-T heat capacity,[20] and in-plane transport.[7, 30] However, it is the scanning tunneling microscope itself which reveals the evolution of the electronic structure across this phase boundary with the most detail.

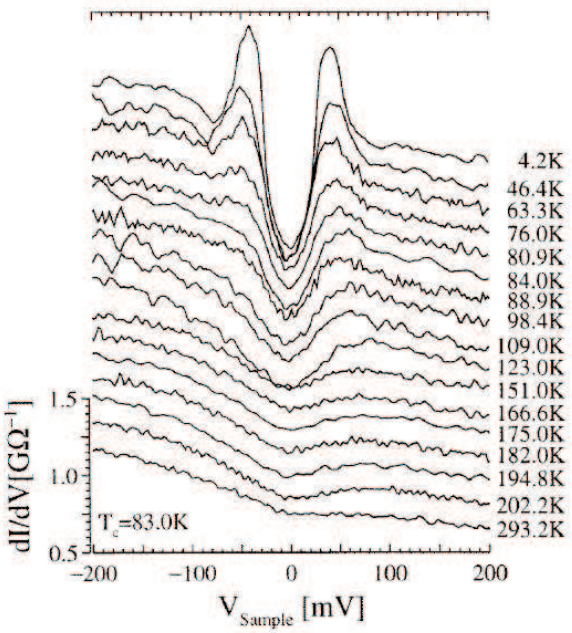

Figure 3.13: Behavior of Gap With Temperature in Underdoped BSCCO. The gap appears as the sample is cooled to 4.2K and enters the pseudogap phase. However, the gap magnitude is not temperature dependent.[26]

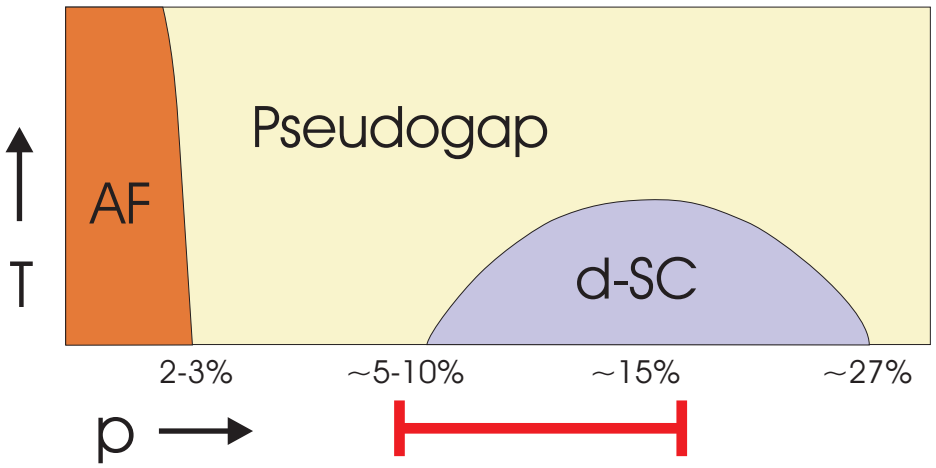

Figure 3.14: Apparent Range Over Which Spectral Gaps Evolve. The red bar under the truncated phase diagram indicates the region over which it has been found that gaps appear to evolve in the cuprates. This range likely extends from within the pseudogap regime, through optimal doping, and perhaps slightly beyond into the overdoped regime.

Measurements of the gap parameter as a function of temperature and as a function of doping by STM seem to imply that the gap measured in the pseudogap regime and in the d-wave superconducting phase may be related,[31] if not one in the same. In Figure 3.13, we see a gradual evolution of of a measured spectral gap as a function of temperature in the underdoped regime.[26] In this measurement, the coherence peaks simply collapse downward as temperature is increased. In addition, as previously shown in Figure 3.12, our research reveals average spectral gaps in BSCCO which appear to evolve slowly over a wide range of dopings, encompassing both the pseudogap and the superconducting regimes. See Figure 3.14 for a schematic of this range. As doping is increased, the gap magnitude is reduced. This effect has also been found near optimal doping in BSCCO.[27] It thus appears, naively, as if the gap seen in both phases is one in the same, and its magnitude is merely being modified as one increases hole doping.

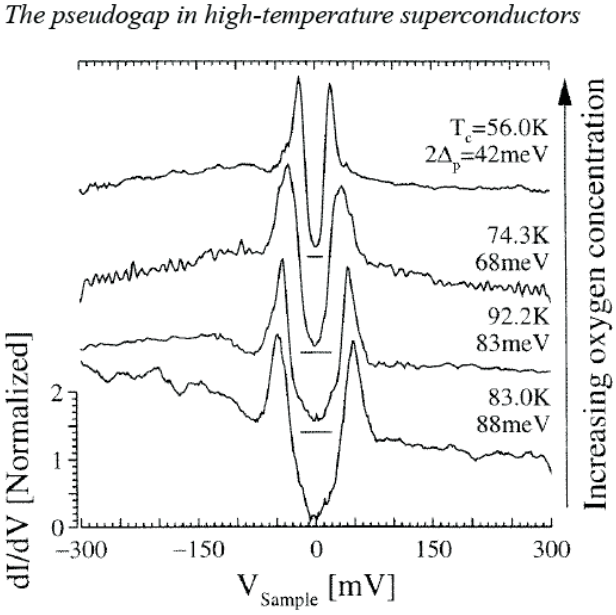

Figure 3.15: Gap Narrowing with Oxygen Doping in Near-Optimally Doped BSSCO.[27]

These evidences point to the boundary between the superconducting and the pseudogap regimes many not constitute a "hard" (1^{st}- or 2^{nd}-order) phase transition at all, but rather a "soft" kind of transition, in which one phase gradually melts into the other. With this idea in mind, it may be reasonable to ask the question whether the actual transition to or from superconducting behavior may be controlled by a different order parameter, or perhaps even by none at all. Perhaps many variables such as a gap order parameter, quasiparticle scattering, spatial electronic ordering, or any other number of phenomena simultaneously form a "recipe" which must be correct for d-wave superconductivity to emerge. It is the aim of this work to try to answer this, and related, questions.

3.9 Experiments Devised to Address Unanswered Questions

We have performed STM experiments on many well-known High-Tc superconductors. Among these are two prominent compounds, BSCCO and NaCCOC, which may be doped in a variety of ways as described in Section 3.2. For each cuprate family, several different transition temperatures and dopings were studied in drawing the conclusions given in this dissertation.

BIBLIOGRAPHY

[1] P. W. Anderson. The 'strange metal' is a projected fermi liquid with edge singularities. *Nature Physics*, 2:626–630, 2006.

[2] N. W. Ashcroft and N. D. Mermin. *Solid State Physics*. Thomson Learning, Inc., 1976.

[3] M. Azuma, T. Saito, S. Ishiwata, I. Yamada, Y. Kohsaka, H. Takagi, and M. Takano. Single crystal growth of transition metal oxides at high pressures of several gpa. *Physica C*, 392-396:22–28, 2003.

[4] M. Azuma, T. Saito, I. Yamada, Y. Kohsaka, H. Takagi, and M. Takano. Single crystal growth of $Ca_{2-x}Na_xCuO_2Cl_2$ and related compounds at high pressures of several gpa. *Journal of Low Temperature Physics*, 131:3/4, 2003.

[5] J. Bardeen, L. N. Cooper, and J. R. Schrieffer. Microscopic theory of superconductivity. *Phys. Rev.*, 106(1):162–164, Apr 1957.

[6] J. Bardeen, L. N. Cooper, and J. R. Schrieffer. Theory of superconductivity. *Phys. Rev.*, 108(5):1175–1204, Dec 1957.

[7] B. Batlogg, H. Y. Hwang, H. Takagi, R. J. Cava, H. L. Kao, and J. Kwo. Normal state phase diagram of $(La,Sr)_2CuO_4$ from charge and spin dynamics. *Physica C*, 235-240:130–133, Dec 1994.

[8] J. G. Bednorz and K. A. M ueller. Possible high-tc superconductivity in the ba-la-cu-o system. *Z. Physik, B*, 64:189–193, 1986.

[9] G. Burns. *High-Temperature Superconductivity: An Introduction*. Academic Press Limited, 24-48 Oval Road, London NW1 7DX, 1992.

[10] A. Cho. High-temperature superconductivity turns 20: High tc: The mystery that defies solution. *Science*, 314(5802):1072–1075, 2006.

[11] Z. Fisk and G. W. Webb. Saturation of the high-temperature normal-state electrical resistivity of superconductors. *Phys. Rev. Lett.*, 36(18):1084–1086, May 1976.

[12] T. A. Friedmann, M. W. Rabin, J. Giapintzakis, J. P. Rice, and D. M. Ginsberg. Direct measurement of the anisotropy of the resistivity in the a-b plane of twin-free, single-crystal, superconducting $YBa_2Cu_3O_{7-\delta}$. *Phys. Rev. B*, 42(10):6217–6221, Oct 1990.

[13] D. M. Ginsberg. *Physical Properties of High Temperature Superconductors II*. World Scientific Publishing Co. Pte. Ltd., P. O. Box 128, Farrer Road, Singapore 9128, 1990.

[14] G. D. Gu, K. Takamuku, N. Koshizuka, and S. Tanaka. Large single crystal bi-2212 along the c-axis prepared by floating zone method. *Journal of Crystal Growth*, 1-2:325–329, 1993.

[15] Z. Hiroi, N. Kobayashi, and M. Takano. Synthesis, structure, and superconductivity of $Ca_{2-x}Na_xCuO_2Cl_2$. *Physica C*, 266:191–202, 1996.

[16] J. Hwang, T. Timusk, and G. D. Gu. Doping dependent optical properties of $Bi_2Sr_2CaCu_2O_{8+\delta}$. *Journal of Physics Condensed Matter*, 19:125208, 2007.

[17] Y. Kohsaka. *Nano-Scale Electronic Spectroscopy of the Metal-Insulator Transition in a High-Temperature Superconductor*. PhD thesis, University of Tokyo, 2004.

[18] K. Lang. *Scanning Tunneling Spectroscopy Study of Inhomogeneity, Granularity, and Segregation in the Electronic Structure of* $Bi_2Sr_2CaCu_2O_{8+\delta}$. PhD thesis, University of California at Berkeley, 2001.

[19] A. J. Leggett. What do we know about high t_c? *Nature Physics*, 2:134–136, 2006.

[20] J. W. Loram, K. A. Mirza, J. R. Cooper, and W. Y. Liang. Electronic specific heat of $YBa_2Cu_3O_{6+x}$ from 1.8 to 300 k. *Phys. Rev. Lett.*, 71(11):1740–1743, Sep 1993.

[21] S. Martin, A. T. Fiory, R. M. Fleming, L. F. Schneemeyer, and J. V. Waszczak. Normal-state transport properties of $Bi_{2+x}Sr_{2-y}CuO_{6+\delta}$ crystals. *Phys. Rev. B*, 41(1):846–849, Jan 1990.

[22] K. McElroy. Death of a fermi surface. *Nature Physics*, 2:441–442, 2006.

[23] N. F. Mott. The basis of the electron theory of metals, with special reference to the transition metals. *Proceedings of the Physical Society of London Section*, A62:416–422, 1949.

[24] L. Neel. Proprietes magnetiques des ferrites - ferrimagnetisme et antiferromagnetisme. *Annales de Physique*, 3:137–198, 1948.

[25] H. K. Onnes. Investigations into the properties of substances at low temperatures, which have led, amongst other things, to the preparation of liquid helium, December 11, 1913. Nobel Lecture.

[26] C. Renner, B. Revaz, J. Genoud, and O. Fischer. Oxygen doping and temperature dependence of the tunneling spectroscopy on $Bi_2Sr_2CaCu_2O_{8+\delta}$. *Journal of Low Temperature Physics*, 105(5-6):1083–1089, Dec 1996.

[27] C. Renner, B. Revaz, J.-Y. Genoud, K. Kadowaki, and O. Fischer. Pseudogap precursor of the superconducting gap in under- and overdoped $Bi_2Sr_2CaCu_2O_{8+\delta}$. *Phys. Rev. Lett.*, 80(1):149–152, Jan 1998.

[28] R. D. Shannon. Revised effective ionic radii and systematic studies of interatomic distances in halides and chalcogenides. *Acta Cryst.*, A32:751–767, 1976.

[29] Z.-X. Shen, D. S. Dessau, B. O. Wells, D. M. King, W. E. Spicer, A. J. Arko, D. Marshall, L. W. Lombardo, A. Kapitulnik, P. Dickinson, S. Doniach, J. DiCarlo, T. Loeser, and C. H. Park. Anomalously large gap anisotropy in the a-b plane of $Bi_2Sr_2CaCu_2O_{8+\delta}$. *Phys. Rev. Lett.*, 70(10):1553–1556, Mar 1993.

[30] H. Takagi, B. Batlogg, H. L. Kao, J. Kwo, R. J. Cava, J. J. Krajewski, and W. F. Peck. Systematic evolution of temperature-dependent resistivity in $La_{2-x}Sr_xCuO_4$. *Phys. Rev. Lett.*, 69(20):2975–2978, Nov 1992.

[31] T. Timusk and B. Statt. The pseudogap in high-temperature superconductors: an experimental survey. *Reports on Progress in Physics*, 62(1):61–122, 1999.

[32] M. Tinkham. *Introduction to Superconductivity, 2nd. ed.* Dover Publications, Inc., 31 East 2nd Street, Mineola, NY 11501, 2004.

[33] J. S. Wen, Z. J. Xu, G. Y. Xu, M. Hcker, J. M. Tranquada, and G. D. Gu. Large bi-2212 single crystal growth by the floating-zone technique. *Journal of Crystal Growth*, 2007.

[34] D. A. Wollman, D. J. Van Harlingen, W. C. Lee, D. M. Ginsberg, and A. J. Leggett. Experimental determination of the superconducting pairing state in ybco from the phase coherence of ybco-pb dc squids. *Phys. Rev. Lett.*, 71(13):2134–2137, Sep 1993.

Chapter 4
Tunneling Asymmetry

Tunneling asymmetry (sometimes abbreviated TA) refers to the differences in spectral weight, or density of states, which appear for energies equal in magnitude away from the Fermi energy (E_F), but opposite in sign. Studies of such differences can bring to light questions of why such "energetic symmetry" is broken as the cuprates are doped, either by electrons or holes.

4.1 Motivation for Interest in Tunneling Asymmetry

There are many reasons of interest to study tunneling asymmetry. Theoretical sum rules, Mott insulator physics, and setpoint effect elimination are among the most prominent motivations.

4.1.1 Spectral Weight Transfer and Sum Rules

In canonical band theory, the density of states is divided at the Fermi level between states which are "hole-like" and "electron-like" because the Fermi function is so sharp around the E_F. All energies greater than the E_F represent probabilities of tunneling into the quantum system (electron injection) and all energies less than E_F represent probabilities of tunneling out of the quantum state (electron extraction). The positive energies can then be thought of in terms of their hole occupations, and negative energies can be thought of as electron-bearing. Thus, in this picture, ratio of positive states to negative states changes as a function of the carrier concentration.

It has been proposed that similar, but more involved, interpretations may apply in the cuprates. Some theorists have suggested this in the form of Mott-Hubbard

calculations revealing spectral weight transfer[8] and sum rules.[2, 3] In the former case, electron and hole contributions to the Hubbard model band structure occur through a similar mechanism as described above, and vary as a strong function of doping. In the latter case, through the use of Gutzweiller-projected resonant valence bond (RVB) theory, sum rules have been developed from spectral function considerations. Among these are the so-called "fugacity" factor Z calculated as

$$Z = \frac{2x}{1+x} \tag{4.1}$$

which is related to the ratio of density of states as

$$\frac{1}{Z} = \frac{g(+|E|)}{g(-|E|)} \tag{4.2}$$

In addition, the integrated local of density of states is related to doping through[10]

$$\frac{\int_0^{\Omega_L} d\omega\ g(\vec{r},\omega)}{\int_{-\infty}^{0} d\omega\ g(\vec{r},\omega)} = \frac{2x(\vec{r})}{1-x(\vec{r})} + \cdots \tag{4.3}$$

with Ω being an energy in the spectrum and Ω_L being an upper cutoff energy chosen by restricting states to the lower Hubbard band (LHB) and requiring $t \ll \Omega_L \ll U$.

Both of these relationships hint at the possibility that the (local) density of states may be related to doping in a simple manner.

4.1.2 Mott Insulator Physics

Many "stripe" and "ladder" theories,[4–6, 9, 11, 12] as well as many others involving forms of hole localization, require spatial reorganization of charge densities which vary as the hole concentration increases from the Mott insulator state. Previous resonant soft x-ray scattering experiments[1] show variation in charge scattering amplitude x=1/8 doped LBCO with variations in temperature, sample angle, and

energy, and quantify the "Mottness" (magnetic versus thermal energy) of the sample in this way. This may be a method in which to understand and test stripe charge variation for a wide variety of compounds. Moreover, if hole densities are, in fact, localized in real space, then a formal, precise means by which to locate and/or quantify them would be a huge step forward to verifying and understanding such localization theories. Thus, the possibility of imaging charge in real space is an important challenge, and success would bestow great explanatory power.

4.1.3 Setpoint Effect

As has been previously described (see Section 1.3.2), the setpoint effect can prove to be a significant obstacle to proper measurement of physical quantities in STM. It would be extremely advantageous if there were a means by which the setpoint effect could be reduced, or better yet, eliminated experimentally or analytically. Fortunately, there is such a means,[7] which I will describe shortly. In fact, it turns out that there are many direct ways in which to deal with measurement inaccuracies due to the setup condition.

4.2 Tunneling Asymmetry Metrics

4.2.1 Canceling the Setpoint Effect

It turns out that many calculable quantities result in a complete elimination of the setpoint effect. Here I define two such quantities, both of which have been very fruitful in revealing underlying physics in the underdoped cuprate compounds. Both of them will be extremely useful tools in the upcoming chapters.

4.2.1.1 Z-Ratio Defined

Ratios are an excellent way to eliminate an inaccuracy in the (more realistic) formulation of the conductance measurements. We can see why with the following derivation. Recall Equation 1.27, which says

$$g(\vec{r}, V) \propto \zeta(\vec{r}, V_0)\rho_s(\vec{r}, eV) \tag{4.4}$$

When one makes a differential conductance map measurement, an entire family of "layers", each layer representing a different energy V, is obtained. We may select any two of these differential conductance layers (e.g. V_1, V_2) to create a new ratio quantity. The conductance ratio $\frac{g(\vec{r},V_1)}{g(\vec{r},V_2)}$ is particularly revealing. In the special case where V_1 is chosen to be $+|V|$, and V_2 is chosen to be $-|V|$, where V is any measured voltage, we may define

$$Z(\vec{r}, V) \equiv \frac{g(\vec{r}, +|V|)}{g(\vec{r}, -|V|)} \tag{4.5}$$

Noting Equation 4.4, we see that the matrix element-dependent prefactor ζ cancels out in the division, as it will do for any choice of V_1 and V_2. Moreover, and perhaps more importantly, Z is directly expressible in terms of measurable quantities only. Hence, we determine

$$\boxed{Z(\vec{r}, V) = \frac{\rho_s(\vec{r}, +e\,|V|)}{\rho_s(\vec{r}, -e\,|V|)}} \tag{4.6}$$

which is a setpoint-independent quantity. $Z(\vec{r}, V)$ is called a "Z-map", and when calculated, has striking qualities which I will describe in the next chapter.

4.2.1.2 R-Ratio Defined

Similarly to the Z-Ratio, the R-Ratio may be defined by taking a ratio of current maps. Again, one is free to take the ratio of any two energy layers (e.g. V_1 and

V_2) in the family of energy layers in a current map to create a ratio. If we again allow $V_1 = +|V|$ and $V_2 = -|V|$, we may define

$$R(\vec{r}, V) \equiv \frac{I(\vec{r}, +|V|)}{I(\vec{r}, -|V|)} \tag{4.7}$$

Noting the form of Equation 1.29, we again note that the prefactor *zeta* will cancel in the division for any choice of V_1 and V_2, no matter what the choice of the bias V_0 was during the map. The new quantity R is also a also function of directly measurable quantities only. Hence we find

$$\boxed{R(\vec{r}, V) = \frac{\int_0^{+e|V|} \rho_s(\vec{r}, E) dE}{\int_0^{-e|V|} \rho_s(\vec{r}, E) dE}} \tag{4.8}$$

which is another setpoint-independent quantity. $R(\vec{r}, V)$ is called an "R-map", and when measured precisely using STM, has striking qualities which I will describe in the next chapter.

4.2.2 Experimental Verification of Setpoint Effect Cancellation

It is claimed that the objects $Z(\vec{r}, V)$ and $R(\vec{r}, V)$ are setpoint-independent quantities. Through the use of Equations 4.5 and 4.7, we may show that this is true. Figure 4.1 shows several selected layers of a differential conductance $g(\vec{r}, V)$ map, measured with two independent bias voltages. In many places, the data from one $g(\vec{r}, V)$ map does not match that of the data from the other $g(\vec{r}, V)$ map for identical energies. However, after calculating $Z(\vec{r}, V)$ using the above equation for each of the two $g(\vec{r}, V)$ data sets, it can be seen that the data now matches for equal energies (see Figure 4.2). (Here, it is understood that the given positive value of the energy V for the ratio map represents the ratio of the $g(\vec{r}, V)$ quantity at the positive $+|V|$ to negative energy $-|V|$.)

Figure 4.1: Bias Independence in Z: Before Calculation. Several selected energy layers of two $g(\vec{r}, V)$ maps measured with different biases, 600mV and -600mV, are shown, along with the $I(\vec{r}, V)$ maps measured simultaneously. Note that the maps are quite different for several energy layers.

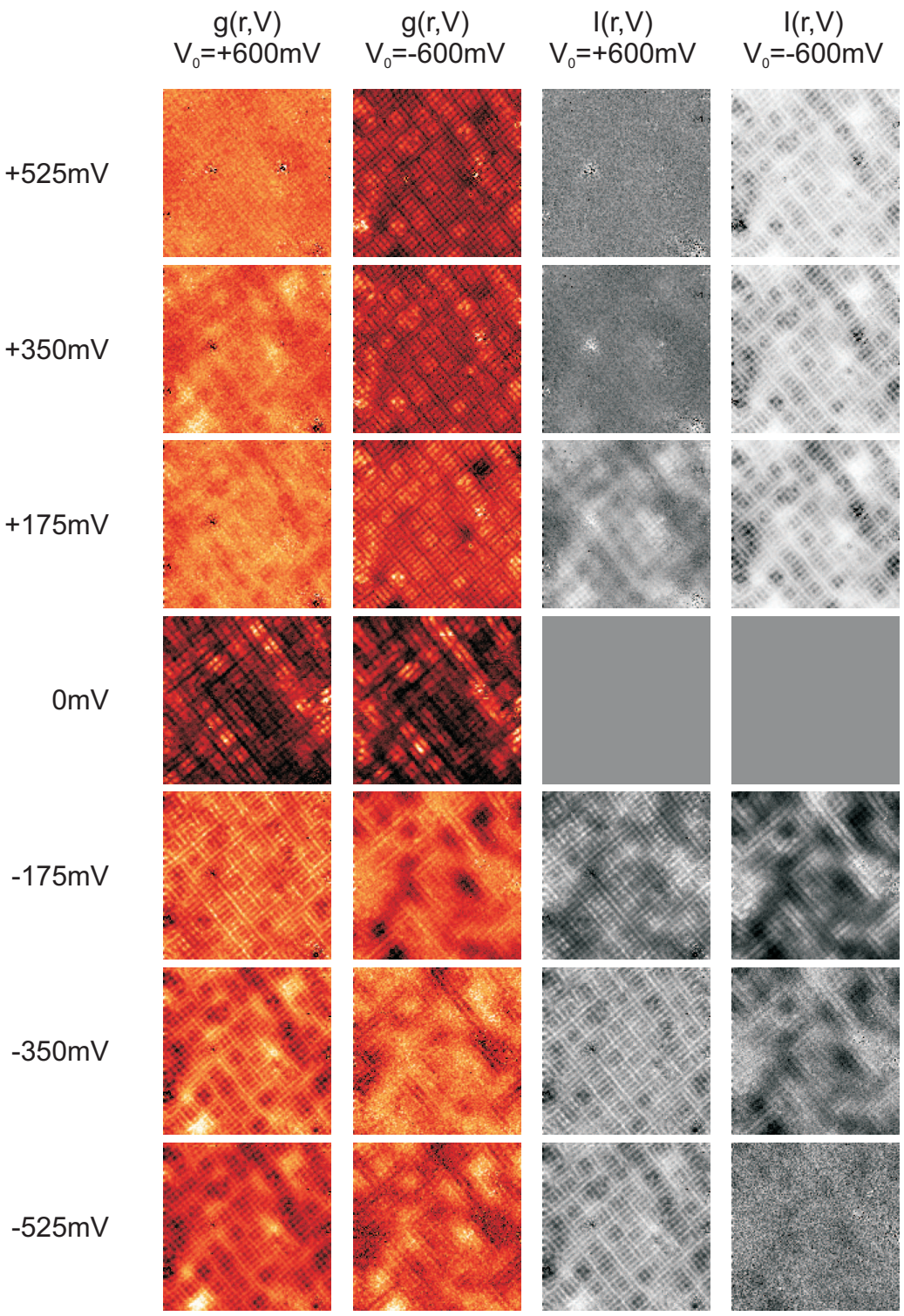
g(r,V)
V0=+600mV
g(r,V)
V0=-600mV
I(r,V)
V0=+600mV
I(r,V)
V0=-600mV
+525mV
+350mV
+175mV
0mV
-175mV
-350mV
-525mV

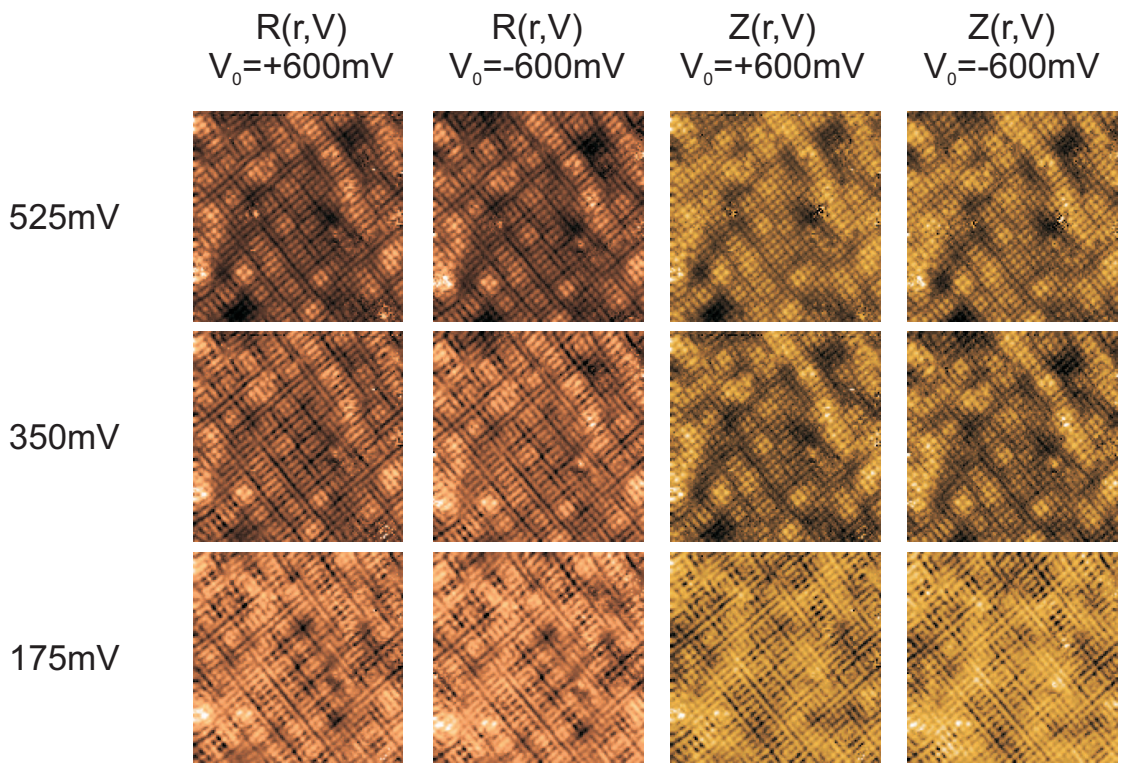

Figure 4.2: Bias Independence in Z: After Calculation. $Z(\vec{r},V)$ and $R(\vec{r},V)$ are calculated for each of the $g(\vec{r},V)$ and $I(\vec{r},V)$ maps in Figure 4.1. The two resulting maps appear almost completely identical. Note that the energy shown for the two asymmetry maps is the magnitude of the bias of each respective $g(\vec{r},V)$ or $I(\vec{r},V)$ map, and not simply a positive energy value.

Thus, we have defined and experimentally verified two setpoint independent quantities. In the next chapters, we will see how they may be exploited to gain insight into the electronic structure of the cuprates.

BIBLIOGRAPHY

[1] P. Abbamonte, A. Rusydi, S. Smadici, G. D. Gu, G. A. Sawatzky, and D. L. Feng. Spatially modulated mottness in $La_{2-x}Ba_xCuO_4$. *Nature Physics*, 1:155–158, 2005.

[2] P. W. Anderson. Present status of the theory of high tc cuprates. *Journal of Low Temperature Physics*, TBD, 2005.

[3] P. W. Anderson and N. P. Ong. Theory of asymmetric tunneling in the cuprate superconductors. *Journal of Physics and Chemistry of Solids*, 67:1, 2006.

[4] E. Arrigoni, E. Fradkin, and S. A. Kivelson. Mechanism of high-temperature superconductivity in a striped hubbard model. *Physical Review B (Condensed Matter and Materials Physics)*, 69(21):214519, 2004.

[5] E. Dagotto and T. M. Rice. Surprises on the way from one- to two-dimensional quantum magnets: The ladder materials. *Science*, 271:618–623, 1996.

[6] S. A. Kivelson, I. P. Bindloss, E. Fradkin, V. Oganesyan, J. M. Tranquada, A. Kapitulnik, and C. Howald. How to detect fluctuating stripes in the high-temperature superconductors. *Rev. Mod. Phys.*, 75(4):1201–1241, Oct 2003.

[7] Y. Kohsaka, C. Taylor, K. Fujita, A. Schmidt, C. Lupien, T. Hanaguri, M. Azuma, M. Takano, H. Eisaki, H. Takagi, S. Uchida, and J. C. Davis. An intrinsic bond-centered electronic glass with unidirectional domains in underdoped cuprates. *Science*, 315:1380, 2007.

[8] M. B. J. Meinders, H. Eskes, and G. A. Sawatzky. Spectral-weight transfer: Breakdown of low-energy-scale sum rules in correlated systems. *Phys. Rev. B*, 48(6):3916–3926, Aug 1993.

[9] D. Poilblanc and T. M. Rice. Charged solitons in the hartree-fock approximation to the large-u hubbard model. *Phys. Rev. B*, 39(13):9749–9752, May 1989.

[10] M. Randeria, R. Sensarma, N. Trivedi, and F.-C. Zhang. Particle-hole asymmetry in doped mott insulators: Implications for tunneling and photoemission spectroscopies. *Physical Review Letters*, 95(13):137001, 2005.

[11] S. R. White and D. J. Scalapino. Checkerboard patterns in the t-j model. *Physical Review B (Condensed Matter and Materials Physics)*, 70(22):220506, 2004.

[12] J. Zaanen and O. Gunnarsson. Charged magnetic domain lines and the magnetism of high-t_C oxides. *Phys. Rev. B*, 40(10):7391–7394, Oct 1989.

Chapter 5
Quantitative Imaging of Tunneling Asymmetry Reveals Electronic Domains

In light of motivations previously discussed with regard to tunneling asymmetry, we[3] performed STM and STS experiments on two lightly hole-doped cuprate compounds, NaCCOC with doping p=0.12 and BSCCO with T_C=45K.

5.1 Asymmetry Evolution with Doping

From considerations of the "fugacity" factor as discussed in Section 4.1.3, we see predicted theoretical tunneling spectra in Figure 5.1(C). As Z (or, alternatively, the hole density n) increases, so decreases the overall ratio of positive energy spectral density to negative energy spectral density. Indeed, actual measurements of the cuprate superconductors NaCCOC in Figure 5.1(D) and BSCCO show similar asymmetry in raw dI/dV spectra averaged over the entire sample area. (Spectra have been normalized such that spectral weight on positive bias side are similar.) Doping (here, x) increases correlate with decreased asymmetry.

These facts serve as a good first check that asymmetry considerations seem justified. However, we need not limit ourselves to averaged spectra; we now have a basis for creating atomic-scale asymmetry maps using variables derived in earlier sections.

5.2 $R(\vec{r}, E)$ Reveals Localization Patterns

The asymmetry map $R(\vec{r}, E)$ is not a direct quantitative measure of charge density. (i.e. Any proportionality coefficient or constant background are completely

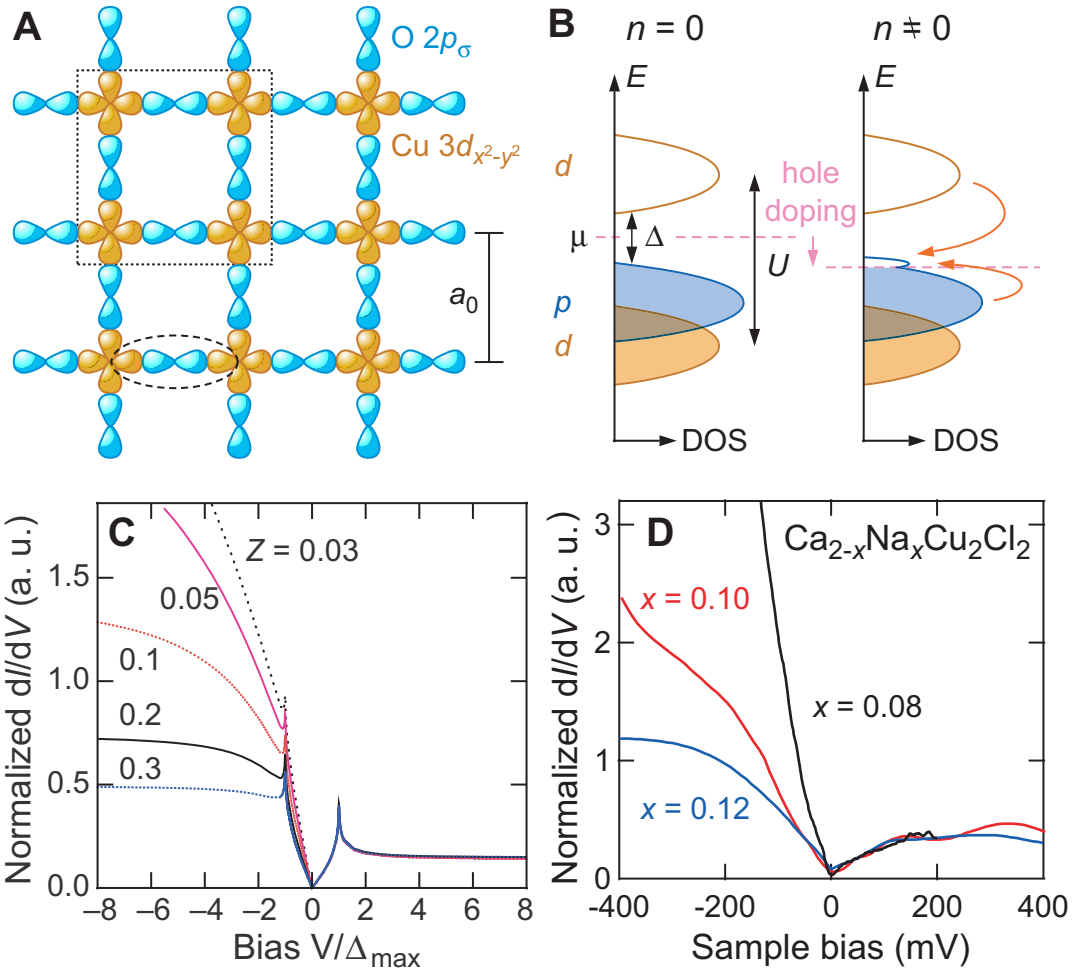

Figure 5.1: Asymmetry and Band Structure as CuO_2 Plane is Doped. (**A**) A schematic representation of the CuO_2 plane. Cu (valance 3d) orbitals are colored in orange while O (valance 2p) orbitals are colored in blue. The cartoon gives orbitals as if independent solutions to the Schrodinger equation represent each atomic constituent. (**B**) Hypothetical electronic band structure of the CuO_2 plane. The left image shows Hubbard-like bands with no doping while the right image shows how doping the Mott insulator may produce additional electronic states. (**C**) Calculated fugacity factor Z^1 asymmetry as a function of energy. The asymmetry shows a pronounced difference between electron injection (+V) and electron extraction (-V). Low values of Z correspond to low hole densities n. (**D**) Measured average tunneling spectra over the sample surface in NaCCOC for three underdoped samples.

unknown.) However, there is some evidence to suggest that the contrast found in an $R(\vec{r}, E)$ map is related to charge density.

First, the quantity is setpoint-independent, as discussed in earlier chapters. (See Section 4.2.1.2.) This excludes any possibility that the map may vary arbitrarily as a function of $\vec{r}$ due to a technical artifact.

Second, the STM measures a real current which must either be related to the (electron/hole) quasiparticle density of states or to a density of states modified by some kind of inelastic process. Inelastic processes would appear as a swift "step up" in dI/dV spectra (or as a strong peak in d2I/dV2 spectra), but we do not see these features in NaCCOC or BSCCO data. In particular, the inelastic phonon process should appear around 40mV,[4] there is no particular shift in dI/dV spectra at that energy. We therefore have no particular reason to presume that measured tunneling currents are anything but elastic in nature, and I will not postulate any inelastic tunneling process for these experiments.

Setting aside inelastic processes, then, the current originates via the mechanism of tunneling from some kind of state in the material in which electrons may exist to quasiparticle states in the metallic tip (or vice-versa). However, the only known states in which an electron may exist in an interacting compound are electronic (band structure, Coulomb) or magnetic (Mott physics, superexchange) in nature. There is no a priori reason to believe that the STM experiments discussed in this dissertation might probe magnetic states; the tips were metallic and not spin-polarized. (i.e. No ions consisting the tip are believed to have had a net spin, nor did the tip have a net magnetization.) Further, no external magnetic fields were applied to the samples before or during the course of the experiments. Because of these facts, we believe it is reasonable to assume the density map $R(\vec{r}, E)$ is in some way related to charge degrees of freedom.

Third, as discussed in Section 4.1.1, some theorists propose sum rules which offer simple relationships between doping level (x) and integrals over the density of

states of highly correlated materials. Although experimentalists cannot reproduce such integrals exactly (due to infinities), we may reproduce them up to a cutoff energy by using a simple mathematical argument (e.g. the definition of R-Ratio). Hence, the $R(\vec{r}, E)$ map could approximate a map which is algebraically related to *local* charge, or doping, in a sample. However, this begs the question as to how doping might become a function of $\vec{r}$, and also whether or not normalizing the integrated function over the volume of the sample would result in the doping of the sample. In other words, while it may be tempting to use Equations 4.3, 4.7, and 4.8 to produce an expression of the form

$$p(\vec{r}, E) \approx \frac{1}{1 + \frac{2}{R(\vec{r},E)}} \tag{5.1}$$

this new local charge density may not be well-defined.

5.3 Discoveries

We chose to try STM spectroscopy (differential conductance) maps on several different cuprate samples. In particular, the compounds NaCCOC and BSCCO, both underdoped cuprate superconductors (see Section 3), were studied exhaustively in our system. Compelled by ideas as described in Section 4.1, we took spectrographic asymmetry measurements and performed a series of calculations and analyses upon them. The samples were cleaved in situ, at cryogenic temperatures and under cryogenic ultra high vacuum, and inserted into our STM head.

5.3.1 Local Asymmetry Variations

Scanning tunneling spectrographs were taken on the sample surfaces of NaCCOC and BSCCO in locations chosen randomly anywhere (limited only by image resolution) between lattice positions. Typical topographs of both sample surfaces are

Figure 5.2: Doping Constituent Comparison of NaCCOC and BSCCO. (**A**) Schematic phase diagram of the high-T_C cuprate superconductors. The lightly hole-doped segment is emphasized, showing the evolution from the antiferromagnetic insulating (AFI) state to the d-wave superconducting (d-SC) phases. Between these two extremes lies the pseudogap (PG) state which, at low temperatures, harbors a glassy character (dotted line) consisting of spin degrees of freedom, charge degrees from freedom, or both. (**B**,**C**) Spectra taken at random points along the surfaces of NaCCOC and BSCCO, respectively, with setpoint 200pA at 600mV. Because the tunneling process keeps integrated dI/dV at positive biases constant due to the bias integration limit in Equation 1.12, the large variations appear at negative bias, which, in turn, acts as a direct measure of spatial variation of the tunneling asymmetry. As can be seen, electron extraction is favored over injection. Measurements indicate strong spatial asymmetry in both crystals, but in addition, the asymmetry itself varies as a function of position on a sub-lattice scale.

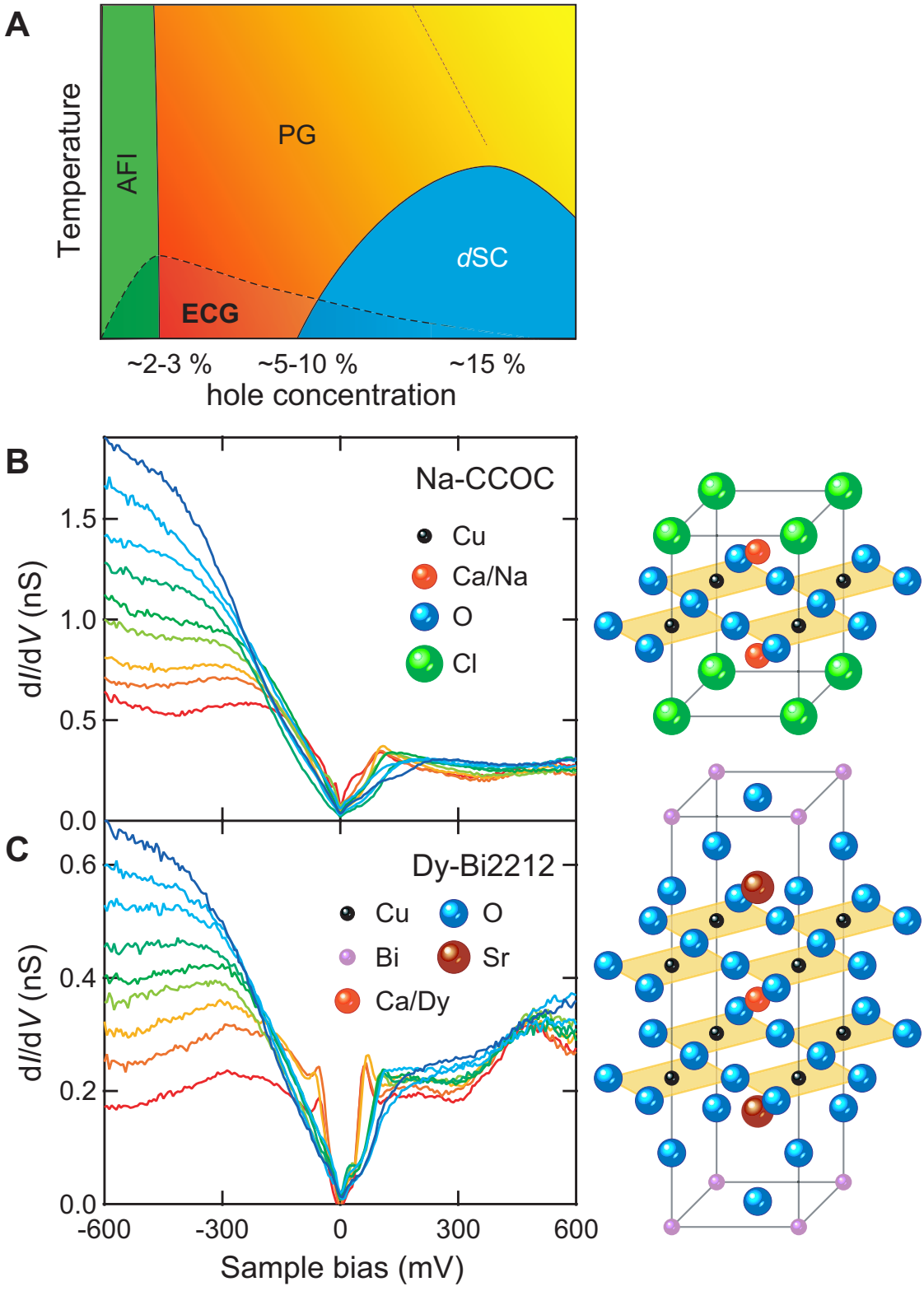
A
Temperature
AFI
PG
dSC
ECG
~2-3 %
~5-10 %
~15 %
hole concentration
B
Na-CCOC
Cu
Ca/Na
O
Cl
dI/dV (nS)
1.5
1.0
0.5
0.0
C
Dy-Bi2212
Cu
O
Bi
Sr
Ca/Dy
dI/dV (nS)
0.6
0.4
0.2
0.0
-600
-300
0
300
600
Sample bias (mV)

shown in Figures 5.3(A,B) and 5.4(C,F). (Data was taken at 4.2K.) For energies within 100mV from the Fermi energy (V=0), we observed the expected V-shaped behavior.[2, 5] However, for energies outside this range, we found that there was significant variation in dI/dV tunneling spectra from point to point. More specifically, as in Figure 5.2(B,C), the spectral weight for positive energies relative to the spectral weight for negative energies varied by a factor of up to 3 as we changed $\vec{r}$. (Spectra were all taken with identical setpoint conditions. Spectra were normalized such that the spectral weight for positive energies was comparable between spectra.) Hence, significant asymmetry variations can, and do, occur as real space is traversed, and on a scale of a fraction of a_0, the lattice constant, over these two underdoped cuprates samples.

5.3.2 Intrinsic Properties of CuO_2 Layers

It should be strongly emphasized that these common features between both materials occur in two chemically drastically different cuprate compounds: the blocking layers of each compound share no common elements. In NaCCOC, the apical sites are occupied by Cl ions, and the substitutional sites can be occupied by either Ca or Na, depending on doping. In the case of BSCCO, apical sites are occupied by O, and Ca may be substituted by Dy between CuO_2 layers (see the right side of Figure 5.2 for a comparison of crystal composition.)

In addition, the BSCCO unit cell has additional interpenetrating layers, the SiO and BiO layers, which increase its complexity with respect to NaCCOC, which has only a single CaCl layer. Termination layer(s) between the topmost CuO_2 layer and the STM tip therefore different completely between the two samples. Further, BSCCO has four CuO_2 layers per unit cell, whereas NaCCOC has only one. The interpenetrating SrO and BiO layers undergo the well-known incommensurate lat-

tice reconstruction, or supermodulation, whereas the CaCl layer in NaCCOC has no such reconstruction. Clearly, these are quite disparate compounds, both chemically and crystallographically. Hence, we assert that any complex phenomenon observed via tunneling asymmetry imaging in both compounds should be logically attributed to their single shared characteristic: the electronic structure of the CuO_2 plane.

5.3.3 High-Energy Asymmetry R-Maps

We continued to investigate asymmetry as well as other atomic-scale effects by measuring differential conductance $g(\vec{r}, E)$ and spectrographic current $I(\vec{r}, E)$ maps with sub-lattice resolution. Calculating $R(\vec{r}, E)$, as in Equation 4.7, for NaCCOC with doping p=0.012 and BSCCO with $T_C = 45K$ reveals several interesting features.

Topographs of NaCCOC (Figure 5.3(A)) and BSCCO (Figure 5.3(B)) show lattice sites as smooth, bright, regular dots on the sample surface. Infrequent sites in the NaCCOC topograph which look like dark crosses are missing Cl atoms, and the dark crosses similar in appearance in the BSCCO topograph are displaced Bi atoms along the maxima of the lattice supermodulation. We believe the topograph to show mainly the effects of the blocking layers; that is, the CaCl layer for NaCCOC and the BiO/SrO layers for BSCCO. Thus, these lattice sites denote Cl atoms in the case of NaCCOC and Bi atoms in the case of BSCCO. We believe this to be true for the following reason. Although vacancies are clearly visible in topographs, they do not appear in any special manner in dI/dV or R maps, which theoretically are believed to be much more closely associated with electronic order. Since blocking layers are generally considered insulating and CuO_2 layers are considered electronically active, it is then reasonable to associate the blocking

Figure 5.3: Comparison of Lattice and Electronic Features in NaCCOC and BSCCO. NaCCOC images are on the left, while BSCCO images are on the right. (**A**,**B**) Constant-current topographs showing the locations of atomic sites in both materials. The topographs are both $12nm^2$ in size. Imaging conditions: (**A**) 50pA at 600mV, and (B) 50pA at 150mV. The orange boxes in each image match the field of view in Figure 5.4(B,C,E,F). The small black arrows indicate the Cu-O bond directions. (**C**,**D**) The R maps in the same field of view as (A,B). The images show $R(\vec{r}, E = 150mV)$. High R (bright) corresponds to low asymmetry (more symmetric), whereas low R (dark) corresponds to high asymmetry (more antisymmetric). The blue boxes share fields of view with the images in Figure 5.4(A,D). (**E**,**F**) Images of $\nabla^2 R$ (i.e. the Laplacian) computed from (C,D). These images help to visualize the atomic-scale features and spatial domain patterns.

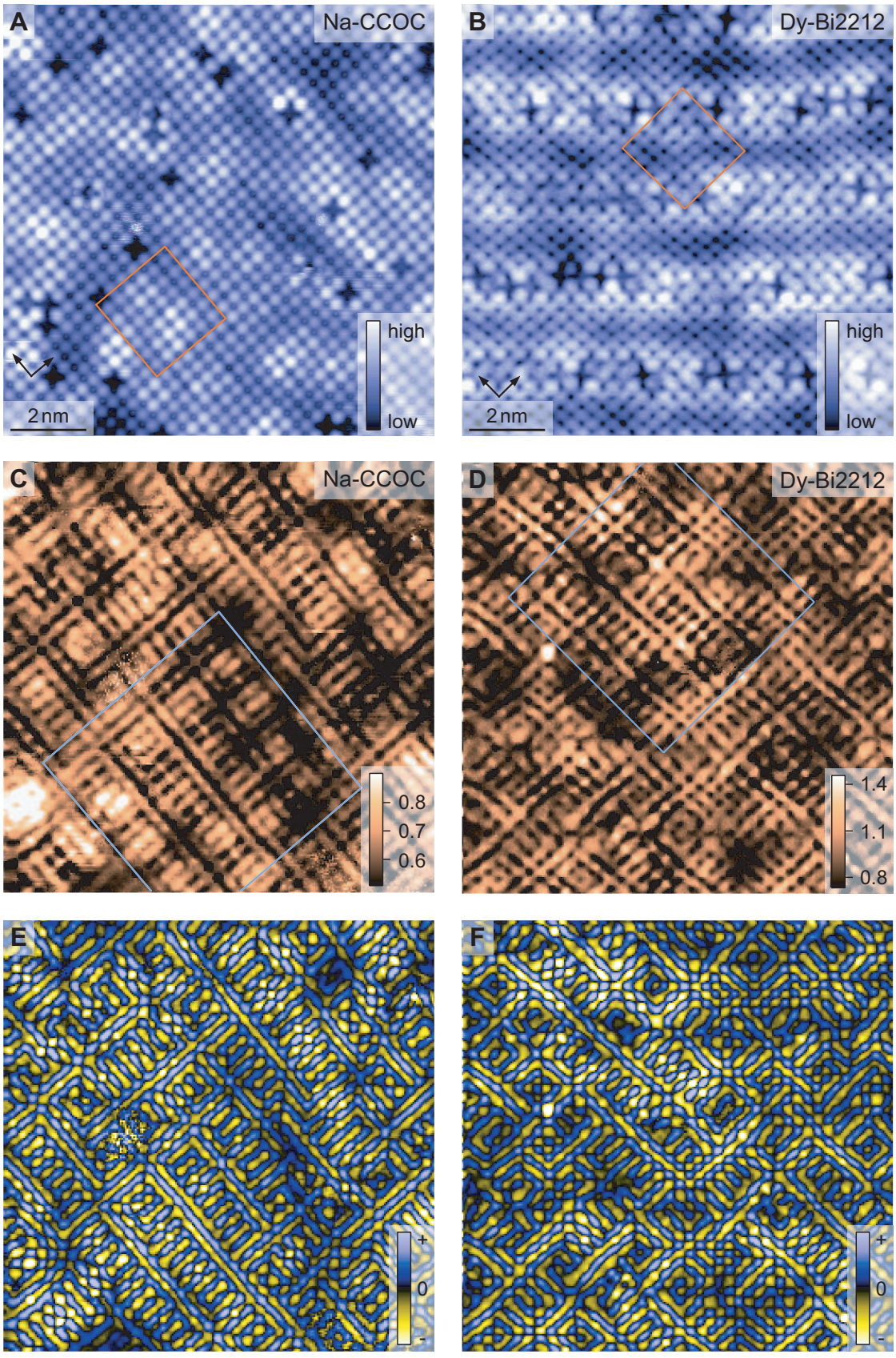
A
Na-CCOC
high
low
2 nm
B
Dy-Bi2212
high
low
2 nm
C
Na-CCOC
0.8
0.7
0.6
D
Dy-Bi2212
1.4
1.1
0.8
E
+
0
-
F
+
0
-

layer with the topograph. Because the Cu sites lie below the Cl atom in NaCCOC and below the Bi atom in BSCCO, the topograph can act as a grid marking the locations of Cu atoms in the CuO_2 plane.

In Figures 5.3(C,D), a single layer (image) of the corresponding $R(\vec{r}, E)$ quantity is presented, with E=150mV. These images are in the same fields of view as the topographs above them. The two R map images appear strikingly similar at first glance. First, there are long regions (10-20 lattice sites long) of both bright and dark lines in both images. These lines have no preferred direction, but lie on the sample surface along one of the two atomic lattice directions with roughly equal probability. The lines do not extend forever, however, but terminate in some local disorder or perhaps another line. Therefore, we claim that the R map demonstrates no long-range spatial order, though locally (from roughly 5-20 lattice sites) some features are unidirectional. On the other hand, autocorrelation analysis does indicate short-range ($\sim 4a_0 \times 4a_0$) periodic correlations. Due to the lack of long-range order and the locations of the bright and dark lines previously mentioned, there is a loss of both translational and 90 deg-rotational (C_4) invariance in the real space electronic structure at the $4a_0$ scale.

Upon closer inspection of the R maps in Figures 5.3(C,D), we note that there exists detail in the R map finer than that in the topographs themselves. To bring these features out more clearly, we take the Laplacian of the R map, $\nabla^2_{\vec{r}} R(\vec{r})$, which in Figures 5.3(E,F) reveals spatial curvature. The "lines" previously mentioned may be more apparent in the Laplacian image. In addition, the atomic (Cu) sites found in the topograph images appear to be connected by yellow regions with a certain pattern. I claim that several of these yellow connections, each of length a_0, stack themselves like rungs on a ladder in various locations on the sample surface. Further, the "lines" previously mentioned appear to play the role of the

ladder supports. Evidently, there are many of these "ladders", or "nanodomains", scattered throughout the sample surface, each seemingly randomly located and oriented. The domains have one long length ($\sim 5-25a_0$) extending along a Cu-O direction, and the width of the domains is $4a_0$ extending along the orthogonal Cu-O axis direction. Hence, the domains are unidirectional on a short length scale, but exhibit no long-range ($\sim> 25a_0$) characteristic. This is again evidence of both C_4 symmetry and translational symmetry breaking by the electronic structure at the sub-nm scale.

5.4 Real-Space Structure of a Nanodomain

To view these domain regions in closer detail, we show R maps in Figures 5.4(A,D), which are higher-resolution images of a few domains which happen to lie next to each other on the sample surface. The R maps have both been oriented such that the Cu-O directions are parallel to the axes of the image, with the length of the domain placed vertically. Note again the strong similarity in structure between NaCCOC and BSCCO. Dark vertical lines are exactly $4a_0$ apart and act as separators between domain regions. (Dark areas in R maps indicate areas of high tunneling asymmetry, and bright areas indicate areas of low tunneling asymmetry.) The domain regions extend along the majority of the image length from top to bottom in both materials.

Zooming in even closer to a part of one of these domains, we observe many finer details of the internal structure of a domain on the atomic scale. Figure 5.4(B) is a cutout of a domain existing in NaCCOC denoted as a blue box in Figure 5.4(A), and Figure 5.4(E) is the corresponding cutout of a domain existing in BSCCO denoted as a blue box in Figure 5.4(D). Lattice sites, found from the topographs (measured simultaneously) in Figures 5.4(C,F), are marked in Figures 5.4(B,E)

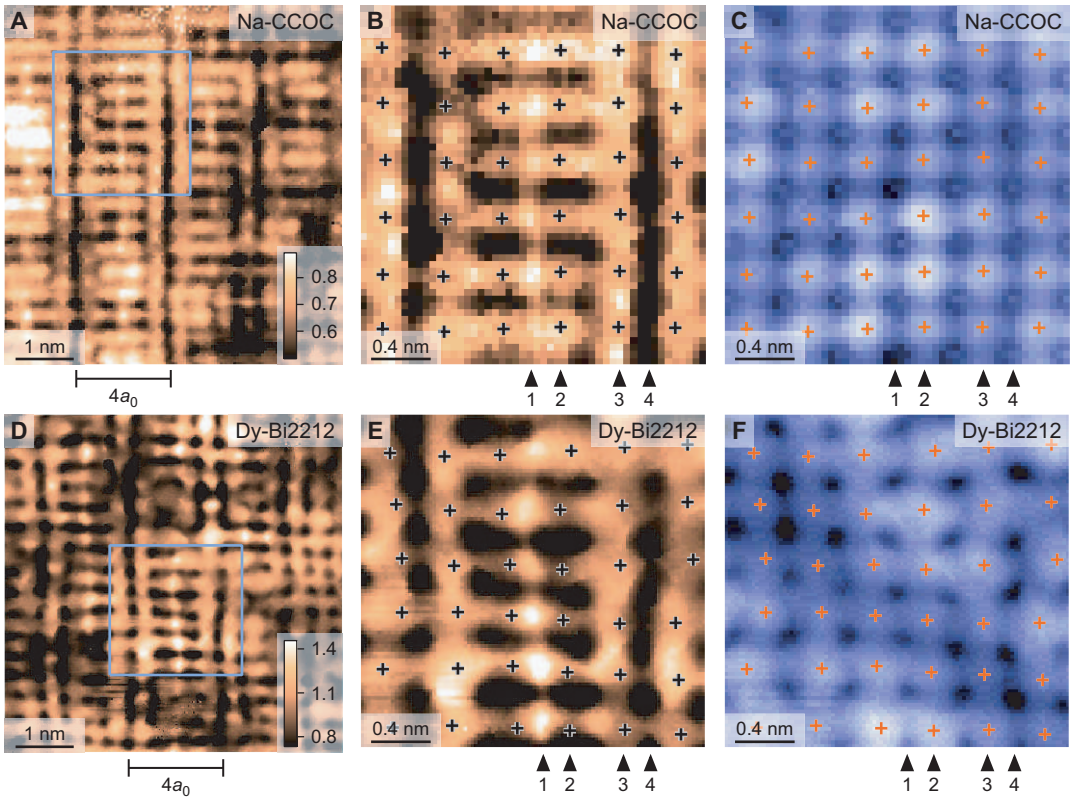

Figure 5.4: Zoom-In of the Features of a Single Domain. (**A**,**D**) R maps of NaCCOC and BSCCO, respectively. The fields of view are the subset of the R maps in Figure 5.3(C,D) indicated by the blue boxes. The energy of asymmetric calculation is again 150mV. The fields of view are (A) 5.0nm×5.3nm, and (B) 5.0nm×5.0nm. The smaller blue boxes in (A,D) share identical fields of view with the areas of (B,C,D,F). (**B**,**E**) A higher-resolution R map within equivalent domains (blue boxes of (A,D)) from NaCCOC and BSCCO, respectively. The locations of the Cu atoms are shown as black crosses. (**C**,**F**) Constant-current topographic images taken simultaneously with (B,E), respectively. Imaging conditions are (C) 50pA at 600mV and (F) 50pA at 150mV. The markers show atomic locations, used also in (B,E). The fields of view of (B,E) are shown in 5.3(A,B) as orange boxes.

so that one can see the contrast in R relative to atomic locations. One initially striking feature of these figures is the vertical line of high R weight occurring in the middle of both domains (denoted as line 1 in both Figures 5.4(B,E)). Because the adjacent lattice sites on either side of this line represent Cu atoms, the bright spots comprising line 1 are O site locations. Indeed, there appears to be R weight

connecting the two adjacent Cu atoms through the central O site to form a Cu-O-Cu object, or bond. These Cu-O-Cu objects seem to form the "rungs" in the aforementioned "ladder" analogy. I claim (and will demonstrate shortly) that the internal structure of the domain object is symmetric about the central line of O sites (line 1), such that the two lines of Cu sites adjacent to line 1 are equivalent, the next two lines outward from the middle are equivalent, and so on. Another way to say this is that the domain has mirror symmetry about the central line of O sites (line 1). There is, in fact, an O site between each Cu site. (Look again at Figure 5.1(A) to see this.) Hence, Cu-O-Cu bonds also exist vertically along line 2 in Figures 5.4(B,E). However, in this case, the O sites exihibit very low R. This is in contrast to the O sites with high R in the central vertical line. Thus, we see a major difference in the magnitude of R atop O sites for the vertical Cu-O-Cu bonds in line 2 versus the horizontal "rung" Cu-O-Cu bonds in line 1. This observation is despite the fact that both two of these Cu-O-Cu (one horizontal and one vertical) may share a common Cu site.

Line 3 in both materials shows fairly high R on both the Cu and the O sites inside it. The Cu atoms in line 3 form horizontal Cu-O-Cu bonds with the O sites in line 4. (The remaining Cu site in the horizontal Cu-O-Cu object is on the neighboring domain.) For these horizontal Cu-O-Cu bonds, the R weight on the O sites is uniformly low. These unidirectional domains, along with the internal spatial structure heretofore described, are found in all R maps taken in a range of $\sim 110 - 180mV$ in NaCCOC and $\sim 80 - 180mV$ in BSCCO. In both materials, they are virtually identical in structure. Further, they are distributed randomly among the two Cu-O directions with equal probability, and they lie commensurate with the square lattice in the CuO_2 plane at random locations.

It is important to note that although all O atoms are in crystallographically

equivalent states, the observations noted above indicate electronically inequivalent states at different O sites, depending on their particular location within a domain. Thus, while the domains themselves exhibit no long-range order, there are repeatable, short-range relationships between neighboring Cu and O sites.

5.5 Spectra within $4a_0$-wide Electronic Domains

We may also measure dI/dV spectra among the atomic-scale locations within the domains. This serves as a method of showing the energy dependence of the spectral weight associated with each point in real space making up the domains, but perhaps more importantly, it serves as a direct comparison between different locations within a domain. This may reveal common features at particular energies between two particular points, and may also show explicitly when two different points are electronically equivalent.

Although, as explained earlier in Section 1.3.5, dI/dV images are contaminated with the setpoint effect, individual dI/dV spectra are not. (Spectra do vary with setpoint bias, but the change is proportional to the setpoint. For point spectra, then, Equation 1.24 holds.) More importantly, dI/dV spectra can point out energies at which significant features or changes occur in the electronic structure. Figure 5.5(A) shows again a schematic representation of the CuO_2 plane. This cartoon may be used in place of Figures 5.4(C,F) for better illustration of the locations, relative to Cu and O sites in the 2D plane, at which individual spectra are measured. Spectra are measured along lines 1 through 4 in Figure 5.5(A), which are the same lines as in the Figures 5.4(C,F), but on different nanodomains. Nine spectra (labeled a-i) per line are presented for lines 1 through 4. In the case of lines 2 and 3, Each set of nine spectra begins on a Cu site and ends $4a_0$, or 4 Cu sites, from the initial Cu site. Spectra alternate between Cu and O sites to bring

Figure 5.5: Linecuts Along One Unidirectional Domain Object. (**A**) Positions along the CuO_2 plane relative to O and Cu orbitals where the spectra in (B) are measured. The field of view for the measurements is identical to that of the topograph in Figure 5.4(C,F). Spectra are measured in 1D along equivalent lines labeled 1, 2, 3, and 4 in both domains of 5.4(B,E). (**B**) Differential conductance spectra taken along parallel lines through equivalent domains in NaCCOC and BSCCO. All spectra were taken using identical junction conditions, 200pA at 200mV. Locations of the lines, relative to the domains, are also indicated in 5.4(B,C,E,F) with arrows.

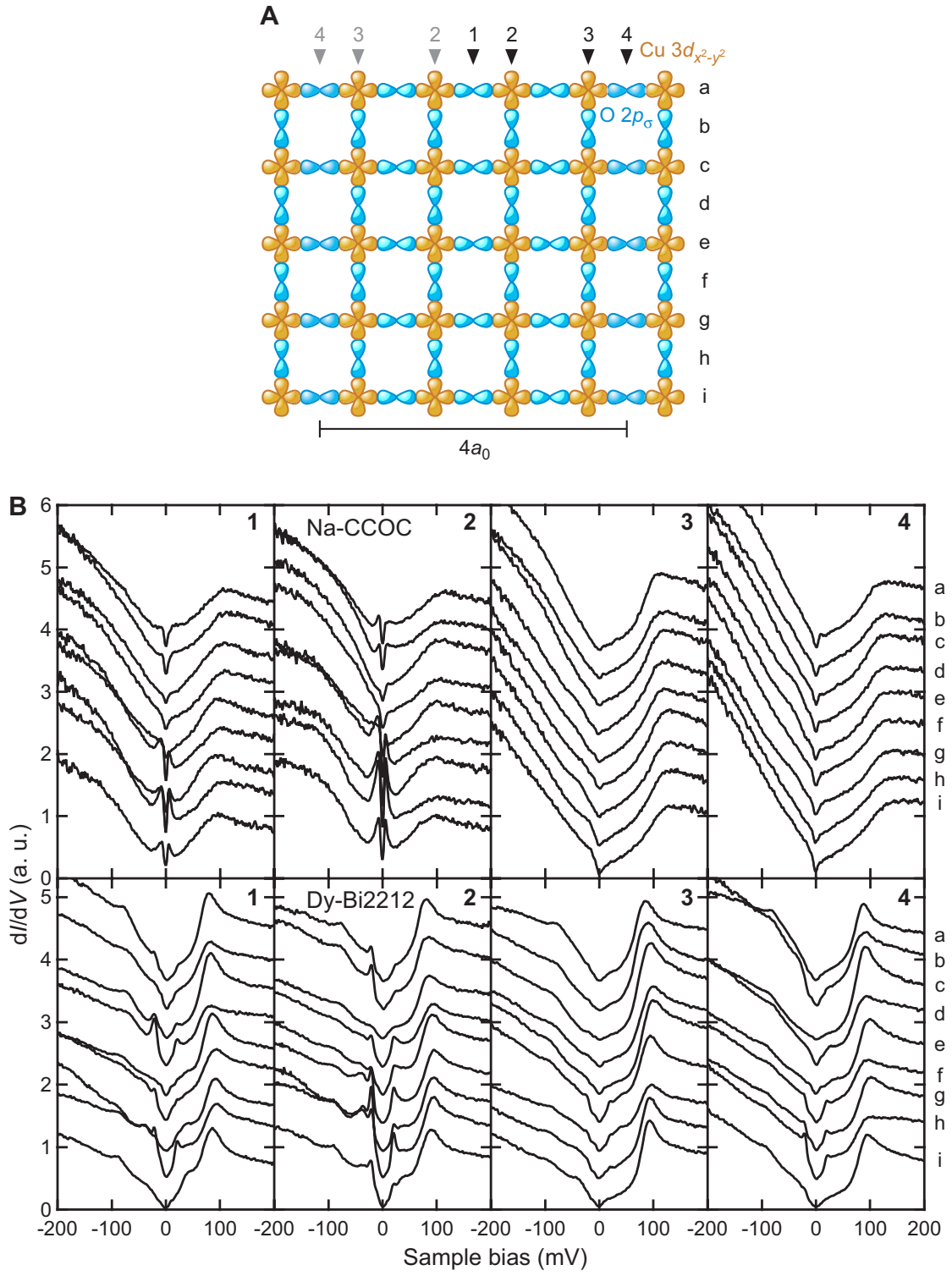
A
4
3
2
1
2
3
4
Cu 3$d_{x^2-y^2}$
O 2p_σ
a
b
c
d
e
f
g
h
i
4a_0
B
Na-CCOC
Dy-Bi2212
1
2
3
4
dI/dV (a. u.)
Sample bias (mV)
-200
-100
0
100
200

the total number of spectra measured to 9 (5 Cu and 4 O sites). In the case of lines 1 and 4, each set of nine spectra begins on an O site and ends $4a_0$, or 4 O sites, from the initial O site. Spectra alternate between O and empty sites to bring the total number of spectra measured to 9 (5 O and 4 empty sites).

In both materials studied, we found much commonality between spectral line evolutions. Line 1 displays a low (minimal) tunneling asymmetry but clear low-energy features. (The features manifest themselves at $\sim 10mV$ in NaCCOC and $\sim 20mV$ in BSCCO.) Tunneling asymmtery in line 2 fluctuates with more strength than Line 3 shows higher tunneling asymmetry than either line 1 or 2, and line 4 shows the highest tunneling asymmetry, with weak low-energy features present. All spectra show a clear, vanishing dI/dV as $|E| \rightarrow 0$. All spectra also show large features around +100mV and -100mV, although the feature on the negative side is drown out due to the large spectral asymmetry for several of the measured lines. The low-energy feature shapes, consisting of dips with visible peaks in lines 1 and 2 but dips with shoulders in lines 3 and 4, may be somehow related to the superconductivity of the samples, as might also be the difference in low-energy feature widths between the two different samples, since T_C for the samples is different.

Note that, if the domain objects are truly 1D over a short distance scale, the spectra for each line should not differ much for the duration of the line. This is generally what we observe. Further, as one should expect from the real-space patterns observed in Figures 5.4(B,E), measured spectra along any two lines symmetric about the central vertical line (line 1) are virtually identical. In addition, the spectra labeled a,c,e,g, and i should appear slightly different than the spectra labeled b,d,f, and h because the lattice locations differ between the two sets. This can be seen in the waterfall plots in Figure 5.5(B): spectra appear in "pairs" which

indicate this interlacing of the two sets of spectra. This is especially evident at high negative energies.

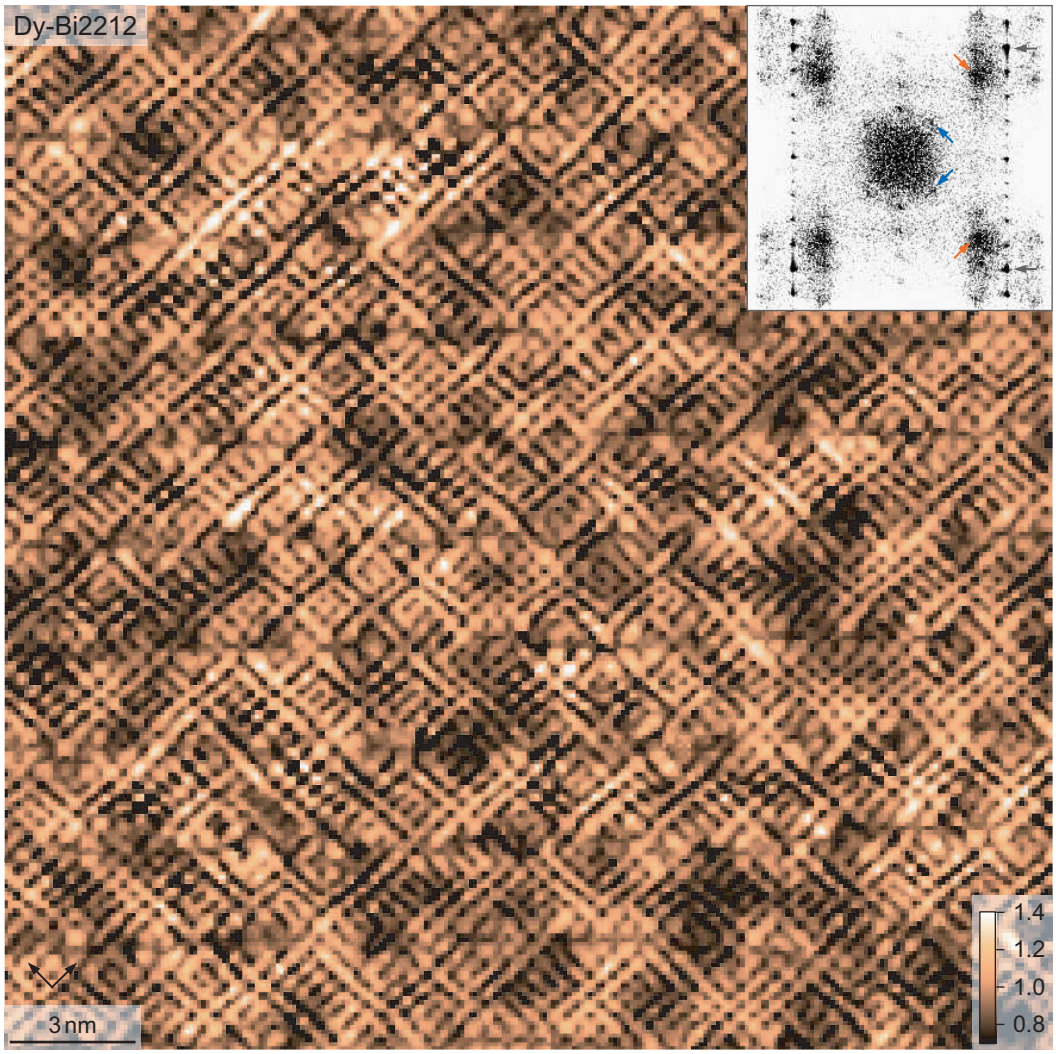

Figure 5.6: A Large R-Map. The map is $25nm^2$, and there is no apparent long range order. Instead, domain objects are readily apparent with no preferred orientation direction, created by arranged Cu-O-Cu bonds on a short ($\sim 5 - 25a_0$) length scale. The Cu-O bond directions are shown as pairs of orthogonal black arrows. (**Inset**) The Fourier transform of the large R-map. Orange arrows show the predominant peaks which occur at $\vec{q} \sim (\frac{3}{4},0)$ and $(0,\frac{3}{4})$ in units of $\frac{2\pi}{a_0}$. Weaker peaks, indicated with blue arrows, $\vec{q} \sim (\frac{1}{4},0)$ and $(0,\frac{1}{4})$. Atomic peaks $\vec{q} \sim (1,0)$ and $(0,1)$ are shown by black arrows.

To demonstrate the ubiquitousness of these domains in a large field of view

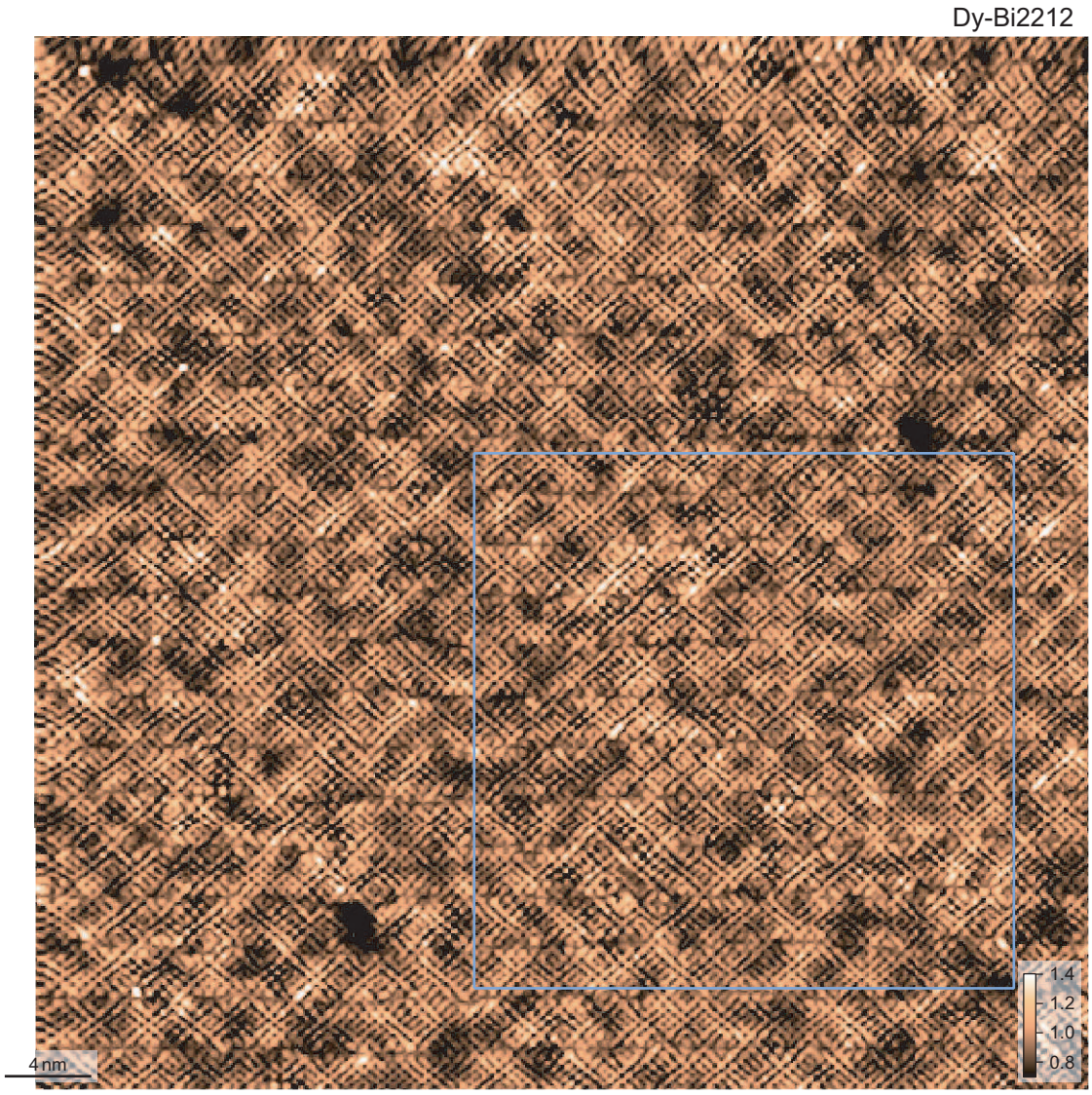

Figure 5.7: A 50nm R map taken at E=150mV. Domains are scattered about the surface in random locations and with equal probability of aligning along either of the two Cu-O directions. The inset is the Fourier transform of the R map, showing strong (3/4,0) and (0,3/4) components (in units of $2\pi/a_0$). The blue box shows is the field of view for Figure 5.6.

as well as re-emphasize the lack of long-range order in the tunneling asymmetry maps, I show Figure 5.6. These images are taken in a $25nm^2$ and a $50nm^2$ field of view, respectively, and while domains are scattered randomly over the surface, no domain stretches for longer than $\sim 25a_0$. Figure 5.7 is a superset of the former figure, and shows the domain order over an even larger length scale in real space. The Fourier transform (inset of Figure 5.6) of these images reveals a strong wavevector component at $\vec{q} = (3/4, 0)$ and, symmetrically through 90 deg rotations, $\vec{q} = (0, 3/4)$ (in units of $2\pi/a_0$). This is somewhat of a surprise, since these "3/4" peaks are even stronger than the "1/4" peaks, wavevector components $\vec{q} = (1/4, 0)$ and $\vec{q} = (0, 1/4)$, which are expected to be prominent because of the $4a_0$ wide domain patterns. It is likely that the strong "3/4" peaks exist due to the fact that each of the three maxima (O site and two Cu sites) contribute from within a single $4a_0$-wide domain, and not because of any superposition of "1/4" and atomic (lattice) wavevector peaks.

5.6 Conclusions on This Chapter

We find very similar spatial structure in the asymmetric R map in two samples, NaCCOC (p=0.12) and BSCCO (T_C=45K), which both have CuO_2 planes but otherwise have no common elements. The two compounds further different in the size of the unit cell, the number of blocking layers between CuO_2 planes, and the presence of a lattice reconstruction, or supermodulation, in the case of BSCCO. Because of these facts, we disregard any material-specific explanations of the observed phenomena, and we attribute the strikingly common characteristics of the tunneling asymmetry map to the electronic structure inherent in the CuO_2 plane, which is the common feature in all cuprates which is thought to be a necessary to produce high-T_C superconductivity. We also believe it is unlikely that indi-

vidual dopant atoms are the direct cause of the effects and patterns presented in this section of the dissertation, because, at a doping level of around ~ 0.12, there is only one dopant atom per ~ 20 Cu-O-Cu bond, and in addition, single dopant atoms occur in quite different locations in the unit cells of NaCCOC and BSCCO. Moreover, a coincidental creation of virtually identical, unidirectional, $4a_0$-wide domains in both materials due to random single dopant impurities seems extremely unlikely. We do not see a disordered array of dopant impurities; instead, we see a much more ordered (on $\sim 5 - 25a_0$ length scales) configuration which we have strong impetus to believe is a direct measure of electronic degrees of freedom of quantum mechanical states in the systems. The major atomic-scale constituent of this structured electronic state is the Cu-O-Cu bond, many of which are sandwiched between "ladder supports" to form these domains.

One possible explanation for these domains is a bond-centered electronic glass, in which the domains themselves play the role of patches, or clusters, making up the amorphous glass. Such a glassy state may be universal among, and fundamental to the electronic structure of, all underdoped cuprates, and could help explain why no long-range charge or spin-ordered states have yet been detected in the intermediate regime between the antiferromagnetic Mott insulator and the d-wave superconducting phases.

Because domains found in tunneling asymmetry experiments appear generally as $4a_0$-wide, quasi-1D objects, with lengths typically several times longer than the width, it is relevant to ask the question whether or not these objects are segments of, or are somehow related to, a charge or spin-ordered "stripe" phase in the cuprates. Many neutron scattering experiments find long-range order in one Cu-O direction and $4a_0$ periodicity in the orthogonal direction, therefore prompting proposals of static stripe models involving individual spin and charge constituents

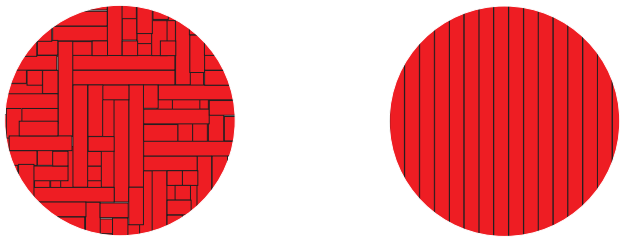

Figure 5.8: (**Left**) A schematic snapshot of the domain glass as observed in R map images. Domains (width $4a_0$) are scattered in random orientations on the surface, but along no preferred Cu-O direction. Domain lengths are nonuniform and are finite ($\sim 5 - 25a_0$). (**Right**) A schematic of a canonical stripe model in which the $4a_0$-wide objects extend without bound in one preferred direction.

in real space. In addition, resonant X-ray scattering probes reveal $4a_0$ periodicity of hole density present on the oxygen sites in the compound LSCO. However, the canonical stripe formulation requires the wavelength associated with the long dimension of the "stripe" object to be (essentially) infinite and the short dimension to be $4a_0$ wide; that is, there is long-range order in both directions. Our data, in contrast, show neither a long-range order in either of the two Cu-O directions, nor a long-range symmetry breaking due to "stripes" flowing in one preferred Cu-O direction (see Figure 5.8). On the other hand, the $4a_0$-wide nature of our domain objects and their long $\sim 5 - 25a_0$ lengths may indicate a stripe order of some kind, perhaps eluding to a modified stripe model for the electronic structure, such as a "disordered stripe" or "glassy stripe" theory.

One possible explanation for the difference between the LSCO and LBCO samples and the NaCCOC and BSCCO samples could be the fact that for former materials' unique crystal symmetry and commensuration around $p = \frac{1}{8}$ result in a dominant electronic order which forces the domains in those particular samples to take on the quintessential long-range, static character. This could be inves-

tigated directly through additional STM experiments, now that we understand how to measure, analyze, and think about these types of tunneling asymmetry experiment.

As described earlier, variations in tunneling asymmetry imply, as a plausible hypothesis, spatial variations in the ratio of electron injection probability to electron extraction probability. This conjecture advances the real possibility that tunneling asymmetry maps are images related to local variations of election occupancy probability, This is even more possible at much higher energies, such as those in which chemistry and charge begin to dominate ($\sim 1V$), implying that a map of local charge variation could be realized through use of tunneling asymmetry techniques.

Finally, it is also important to remember that these electronic phenomena are present simultaneously with the d-wave superconductivity inherent in appropriately doped cuprate compounds. More precisely, the patterns reported in this dissertation must necessary coexist (at least) spatially with the effects of the superconductivity, but the latter is likely found at much lower energies than that at which the domain patterns exist. Further, d-wave superconductivity in the cuprates manifests itself as delocalized pairs of (electron) quasiparticles, whereas these spatial domain patterns are clearly static and localized in excited states. Yet, with increased doping, the latter state is gradually and smoothly converted into the former. These ideas should remain in the reader's mind in the next chapter.

BIBLIOGRAPHY

[1] P. W. Anderson and N. P. Ong. Theory of asymmetric tunneling in the cuprate superconductors. *Journal of Physics and Chemistry of Solids*, 67:1, 2006.

[2] T. Hanaguri, C. Lupien, Y. Kohsaka, D.-H. Lee, M. Azuma, M. Takano, H. Takagi, and J. C. Davis. A 'checkerboard' electronic crystal state in lightly hole-doped $Ca_{2-x}Na_xCuO_2Cl_2$. *Nature*, 430:1001–1005, 2004.

[3] Y. Kohsaka, C. Taylor, K. Fujita, A. Schmidt, C. Lupien, T. Hanaguri, M. Azuma, M. Takano, H. Eisaki, H. Takagi, S. Uchida, and J. C. Davis. An intrinsic bond-centered electronic glass with unidirectional domains in underdoped cuprates. *Science*, 315:1380, 2007.

[4] J. Lee, K. Fujita, K. McElroy, J. A. Slezak, M. Wang, Y. Aiura, H. Bando, M. Ishikado, T. Masui, J.-X. Zhu, A. V. Balatsky, H. Eisaki, S. Uchida, and J. C. Davis. Interplay of electronlattice interactions and superconductivity in $Bi_2Sr_2CaCu_2O_{8+\delta}$. *Nature*, 442:546–550, 2006.

[5] K. McElroy, D.-H. Lee, J. E. Hoffman, K. M. Lang, J. Lee, E. W. Hudson, H. Eisaki, S. Uchida, and J. C. Davis. Coincidence of checkerboard charge order and antinodal state decoherence in strongly underdoped superconducting $Bi_2Sr_2CaCu_2O_{8+\delta}$. *Physical Review Letters*, 94(19):197005, 2005.

Chapter 6
Bogoliubov Quasiparticle Interference Shows Energetic Phase Separation

It is believed that the pseudogap regime (discussed in Section 3.8) is the intermediary crossover existence between the Mott insulator, with well-defined order in real-space, and the $\vec{k}$-space eigenstates, or Bogoliubov quasiparticles, formed upon the emergence of high-T_C superconductivity. Because quasiparticle interference (QPI) analysis techniques provide a means to measure the Bogoliubov quasiparticle states in real-space and $\vec{k}$-space simultaneously, it is plausible to consider a series of directed experiments to test these theoretical ideas.

6.1 $Z(\vec{r}, E)$ and Antisymmetry Clarity

Similarly to the discussion in Section 5.2, $Z(\vec{r}, E)$ is a good tool for exposing antisymmetric features. First, as also noted with $R(\vec{r}, E)$, Z is a setpoint-independent quantity, which means that calculating it eliminates the artifact in measurements introduced due to different choices of setpoint bias and/or current.

In addition, features which are symmetric about the Fermi energy (E_F) will be removed in calculating (energy-symmetric) ratio maps. Simply put, the division operation of the ratio map results in low values where the values of energy-symmetric layers are roughly equivalent, and high values where there is disparity between the two layers. In particular, the low-energy checkerboard[10] which exists in both NaCCOC and BSCCO is all but removed in $Z(\vec{r}, E)$, allowing weaker quasiparticle interference patterns to be seen without obstructions.

In fact, the Z ratio attenuates symmetric signals so well that weaker asymmetric signals in $|DFT[Z(\vec{r}, E)]|$ (Discrete Fourier Transform; see Appendix A), or

$\left|\tilde{Z}(\vec{q}, E)\right|$, are enhanced,[9] both numerically and visually. Calculating this quantity brings forth quasiparticle interference due to scattering in much more vividly than in $|DFT(g)|$. At first thought, one may expect Bogoliubov QPI peaks to also be attenuated by the division operation, if the empty states and filled states were in same spatial phase. However, A.V. Balatsky[7] points out that, due to particle-hole mixing of Bogoliubov quasiparticles, this is not the case.

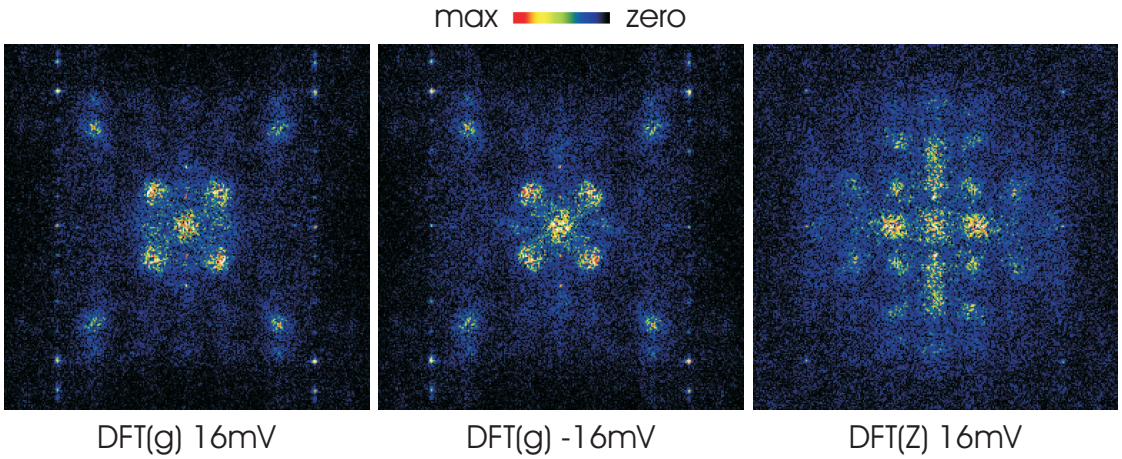

Figure 6.1: Comparison of Fourier Transforms of dI/dV to those of Z. The first two images show both the positive and negative energy layer of $|DFT(g)|$ for $|E| = 16mV$. The last image on the right shows the corresponding $|E| = 16mV$ layer for $|DFT(Z)|$. The difference is quite dramatic: Calculating $|DFT(Z)|$ in lieu of $|DFT(g)|$ brings out the quasiparticle interference quite vividly. The same color scale is used for all three images.

As can be seen in Figure 6.1, the difference between the Fourier transform of g and that of Z is significant. For any particular energy, the quantity $|DFT(Z)|$ brings out the quasiparticle interference much more vividly than $|DFT(g)|$ does. Hence, it makes sense to use Z as a vehicle to locate quasiparticle interference peaks.

6.2 Theory: Octet Model

The best-known, simplest, (and practically speaking, the most experimentally verified) model for understanding quasiparticle interference due to scattering in the cuprate superconductors is the octet model.[15, 23] The model has its origins in trying to understand the connection between numerical band structure computations and Fourier transform scanning tunneling spectroscopy experiments.[23]

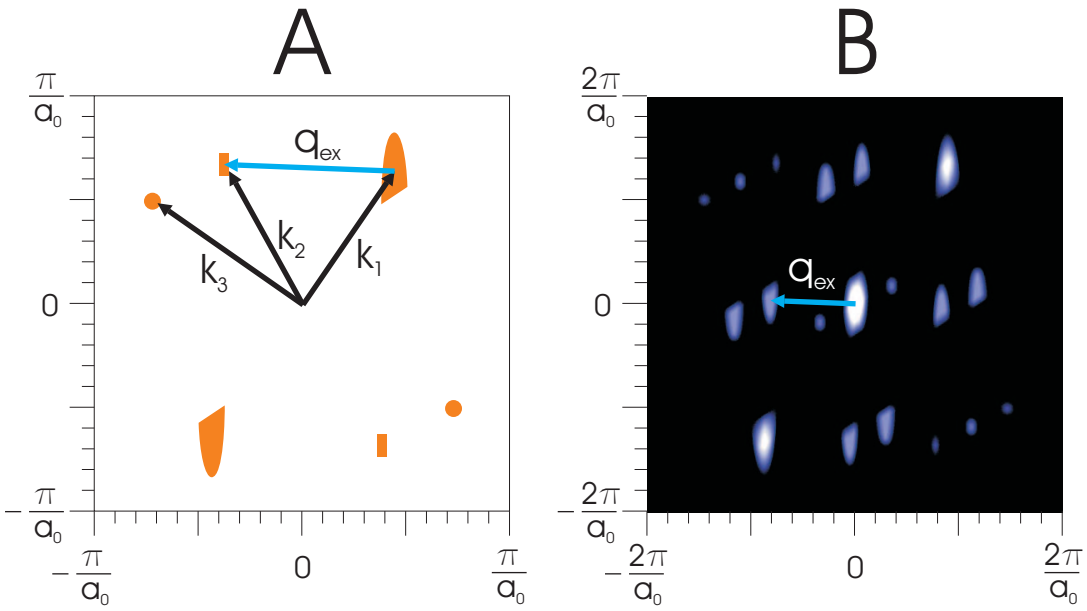

Figure 6.2: (**A**) A faux band structure for a particular chosen energy in k-space. k_i vectors exist technically for all continuous points in the space, but only certain ones (near areas with high spectral weight) are labeled. One scattering vector $\vec{q}_{ex}$ denotes coherent scattering from one the state with index $\vec{k}_1$ to the state with index $\vec{k}_2$. (**B**) Autocorrelation of band structure image in (A). This gives all possible scattering vectors $\vec{q}_i$ weighted due to possible scattering interactions from states in (A).

In basic terminology, one first assumes that quasiparticle scattering is possible, via a variety of mechanisms, to scatter between available quasiparticle states at any particular energy. In general, any quasiparticle should be able to scatter

from any one well-defined state in quasimomentum-space, or $\vec{k}$-space, to any other state. However, the available states themselves are governed by the electronic band structure, Coulomb interactions, hopping integrals, spin-spin interactions, Pauli exchange physics, or any number of other mechanisms depending on the Hamiltonian used in theoretical physical models. Thus, some states in $\vec{k}$-space have a high quantum mechanical probability of being occupied, some states have much lower probability, and some have none. The distribution of these probabilities can be seen in a 2D-image of $\vec{k}$-space at one particular energy. Brighter regions in such an image show $\vec{k}$ values which have a higher probability of being occupied by quasiparticles than darker regions. One simple (arbitrarily drawn) example is shown in Figure 6.2(A). The vectors extend from the center of the image, which is the origin ($\vec{k} = 0$), and they denote several different states in $\vec{k}$-space (e.g. $k_1, k_2, \ldots, k_N$). Technically, there are infinitely many such $\vec{k_i}$ vectors pointing to all the points in the continuous space defined by $\vec{k} \in [-\frac{\pi}{a_0} \rightarrow +\frac{\pi}{a_0}, -\frac{\pi}{a_0} \rightarrow +\frac{\pi}{a_0}]$.

In general, the scattering that will occur will be the net effect, or sum, of all quantum mechanical states (defined by $\vec{k}$ and the energy E) scattering into all *other* possible states in $\vec{k}$-space. Each one of these scattering events, of which there are also technically infinitely many, may be denoted by an vector from the initial state to the final state. These vectors are typically labeled $\vec{q}_{ij}$, and I label one example of such a vector $\vec{q}_{ex}$ in Figure 6.2(A) (blue arrow). The most general way to compute these $\vec{q}_{ij}$ vectors is simply to take the k-space image and cross correlate spatially it with itself, or autocorrelate it. The correlation function shows where two peaks in two different images interfere with each other. By (mental) analogy, it does this by overlaying one of the images on the other one, for every position $\vec{k}$, and calculating a value which quantifies how well the images match with each other at that particular $\vec{k}$. As an example, the autocorrelation of the band structure shown

in figure 6.2(A) is shown in Figure 6.2(B). Such a method is rigorous but numerical (not analytical) in nature, and the results may be complicated and prohibitively difficult to deconvolve.

Now, suppose that there are only a few locations in $\vec{k}$-space for which energy eigenstates exist, but where the local dispersion is relatively low (i.e. low $\nabla_{\vec{k}} E(\vec{k})$). The quasiparticle density of states at energy E is proportional to $\left|\nabla_{\vec{k}} E(\vec{k})\right|^{-1}$:[14]

$$n_s(\epsilon) \propto \oint_{E(\vec{k})=\epsilon} \frac{d\vec{k}}{\left|\nabla_{\vec{k}} E(\vec{k})\right|} \tag{6.1}$$

and hence, the largest contributions to the spectral density will occur at these few, shallowly dispersive locations. In such a case, the number of coherent, well-defined state locations which one could label with a definite $\vec{k}_i$ vector is few. In turn, the number of scattering vectors $\vec{q}_{ij}$ may also be few (but, of course, more numerous than the $\vec{k}_i$), since any one state may scatter into any other. Then, it may be relatively easy to define a simple mathematical model for finding the $\vec{q}_{ij}$ vectors from the k_i vectors analytically, without the need to use autocorrelations or other processing. In effect, one should be able to find a mapping F such that $\vec{q}_{ij} = F_{ij}(\vec{k}_1, \vec{k}_2, \ldots, \vec{k}_N)$. This is the role the octet model plays.

Of course, in real experiments, one does not know the $\vec{k}_1, \vec{k}_2, \ldots, \vec{k}_N$ vectors for the band structure; they are the unknowns to be determined. Instead, measured peaks in the 2D Fourier transforms of the density of states are assumed to be due to scattering from some objects (impurities, lattice vacancies, dopant atoms, vortices, gap disorder,[17] step edge boundaries, etc). With that assumption, the measured peaks found are then simply the $\vec{q}_{ij}$ vectors of scattering. It should be noted that, as described in Section 4.1.3, we do not technically have direct access to the local density of states in STM measurements. However, we may use a variety of other quantities in its stead, such as the Fourier transform of dI/dV, Z, d(lnI)/d(lnV), and so on. In this dissertation, I use the Fourier transform of Z to obtain all $\vec{q}_{ij}$

vectors, for the reasons discussed in Section 6.1.

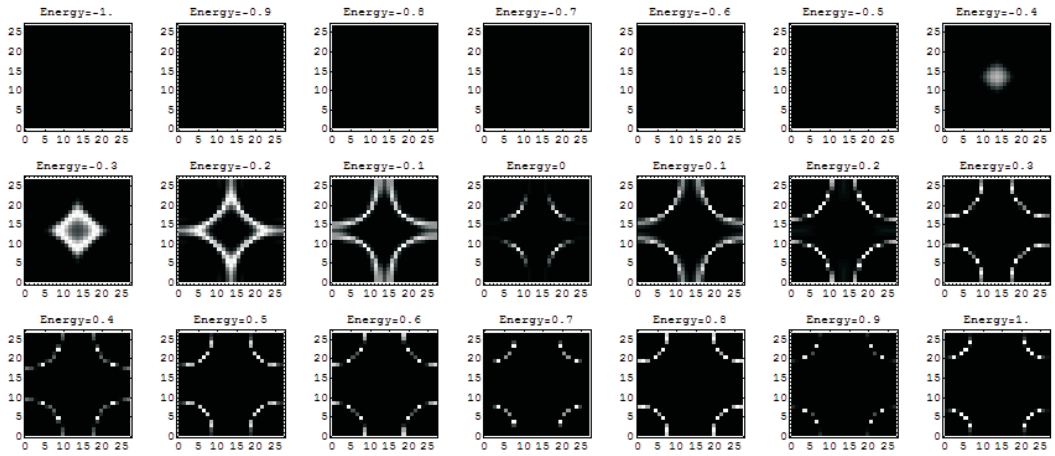

Figure 6.3: Density of States of a D-Wave Superconductor Via Bogoliubov-de Gennes. This figure represents the spectral weight of the density of states at various energies (in eV) calculated numerically on a real-space 26x26 grid with a Hamiltonian solver. Tight-binding and mean-field approximations are applied. There is a single non-magnetic impurity as a background potential. Nearest neighbor hopping parameter $t = 0.300$, next-nearest neighbor parameter $t' = -0.4t$, chemical potential $\mu = -1.18t$, and particle/antiparticle coupling $\Delta = 25meV$. This calculation was performed by the author.

Of course, this complicates matters, because instead of a mapping from F from k-space to q-space, one needs a sort of inverse mapping F^{-1} from q-space to k-space. In our case, the inverse mapping is specified by the octet model, which basically asserts that there are only 8 relevant peaks in the density of states of the cuprates for a particular energy range. This is a reasonable assumption, since known information about the cuprate band structure in quasimomentum space, as measured with ARPES, show gapped antinodal regions around (π,0), but "Fermi arcs" in the nodal (π,π) direction.[5, 6] In addition, tight binding theories give gapped nodes for a d-wave superconducting order parameter (see Figure 6.3), showing 4 "bananas", with the weakest dispersion in the calculated k-space band structure occurring at either end of each "banana".[15] This gives 2 strong points per

"banana", or a total of 8 points. Armed with the octet model, one may then find the inverse mapping F^{-1} through the use of a few simple algebraic manipulations.

6.2.1 Scattering and the Octet Model

The inverse mapping F^{-1} discussed in Section 6.2 is overdetermined, meaning that using a variety of combinations of $\vec{q}_{ij}$ vectors, one can find a particular vector $\vec{k}_j$. This may seem like a problem at first, but it can actually be used to our advantage because different combinations can be used as redundant checks to verify and give support to the $\vec{k}_j$ value we want to determine. If the values are too far apart, it can also be a metric for qualifying either the quality of the measured data or the validity of the octet model itself.

In general, a quasiparticle may scatter from any one state $\vec{k}_i$ to any other state $\vec{k}_j$, defining a set of $\vec{q}_{ij}$ vectors as follows.

$$\vec{q}_{ij} = \vec{k}_i - \vec{k}_j \tag{6.2}$$

Both i and j run over all possible states, which are, in general, infinitely many. However, for the octet model, there are only 8 possible states, so we label them states 0-7, and $i, j \in 0 \ldots 7$. This brings the number of possible $\vec{q}_{ij}$ vectors to 64 for the octet model, but using symmetry considerations, we will see that many of these vectors are simply related to the others, or may even be redundant.

6.2.2 Various Symmetries: Rotational and Algebraic

The octet model contains many symmetries. In declaring any particular symmetry (thereby reducing the total number of $\vec{q}_i$ vectors in consideration), an assumption is made. Each assumption should be carefully weighed and accepted as reasonable.

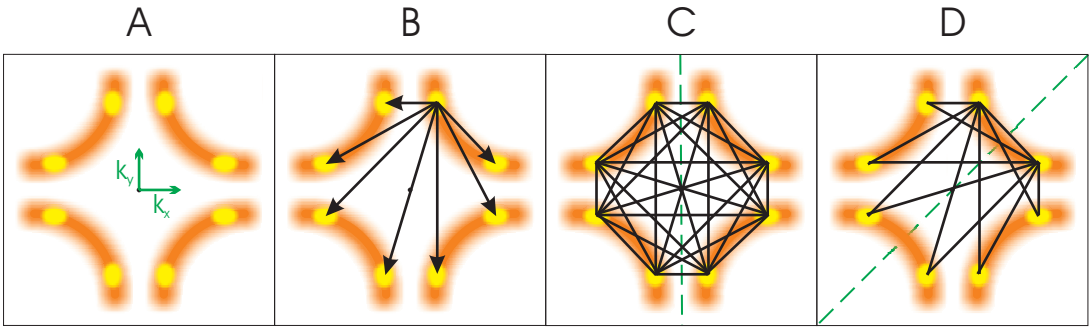

Figure 6.4: Various Symmetries in Octet Model

For each of the 8 points represented schematically in Figure 6.4(A), there can be scattering to any other point, for a total of 64 scattering possibilities. Since $\vec{q}$=0 represents self-scattering and is not so interesting with regard to the band structure, we eliminate it from consideration, leaving only 7 scattering possibilites per scattering origin point. (All 7 scattering possibilities from just one k_i point are shown in Figure 6.4(B).) Thus, we then have total 56 possible scattering possibilities.

The first symmetry is inversion, that scattering from state A to state B is the same as scattering from state B to state A. This symmetry is assumed for two reasons: 1.) Quasimomentum space is 2-fold rotationally symmetric about the origin, so scattering from $\vec{k}_A$ to $\vec{k}_B$ automatically implies scattering from $\vec{k}_B$ to $\vec{k}_A$. This is a consequence of the fact that the lattice (and the Fourier transform) cannot distinguish between directions under 180 deg rotations. 2.) For any two particular band structure points, $\vec{k}_A$ and $\vec{k}_B$, scattering is equally likely to occur from $\vec{k}_A$ to $\vec{k}_B$ as from $\vec{k}_B$ to $\vec{k}_A$. Unless there is an exotic[24] reason to believe that detailed balance is not satisfied for elastic quasiparticle scattering in the cuprates, it seems reasonable to assume it is true. The net consequence of 1.) and 2.) is that for every $\vec{q}_i$ there will be a mirror $\vec{q}_i$ 180 deg from it, and both of these peaks will

be essentially doubled in intensity from a case in which detailed balance somehow could not occur. This symmetry reduces the number of vectors to consider to $28 = 56/2 = 7+6+5+4+3+2+1+0$. All 28 are shown in Figure 6.4(C), where, with inversion symmetry assumed, each line represents a double arrow to indicate bi-directional scattering. (The arrows are omitted for simplicity.)

The remaining symmetries appeal to the fact that we may enforce the inherent symmetries of the band structure of the d-wave superconducting gapped tight-binding model. While it is not required that the real data follow any particular model, I will a posteriori claim that we see no breaking of any of the following two symmetries in our data. Furthermore, we will see later in this chapter many examples of how quasiparticle scattering fits very well with these symmetry assumptions.

One such model-dependent symmetry is horizontal (or vertical) mirror symmetry. That is, if one flips $\vec{k}$-space horizontally about the $\vec{k}_x = 0$ line (shown in dashed green in Figure 6.4(C)), there are several vectors which will then lie on top of one another. This is similarly true for vertical mirror flips. If we assume such a mirror symmetry, as is the case with a BdG d-wave order theory, then we may eliminate redundant vectors (ones which overlap in the mirror operation). Because Fourier space is 2-fold rotationally symmetric about the origin, it should be pointed out that once mirror symmetry is assumed in one direction (horizontal or vertical), then the other mirror symmetry is equivalently automatically assumed. This is because we have already assumed inversion symmetry, and the mirror operation introduces more redundancies due to inversion. Hence, we arrive at Figure 6.4(D), which has 13 unique vectors after assuming mirror symmetry.

The final symmetry is to assume that behavior in the $\vec{k}_x$ direction is equivalent to behavior in the $\vec{k}_y$ direction. That is, the lattice is 4-fold isotropic, and there

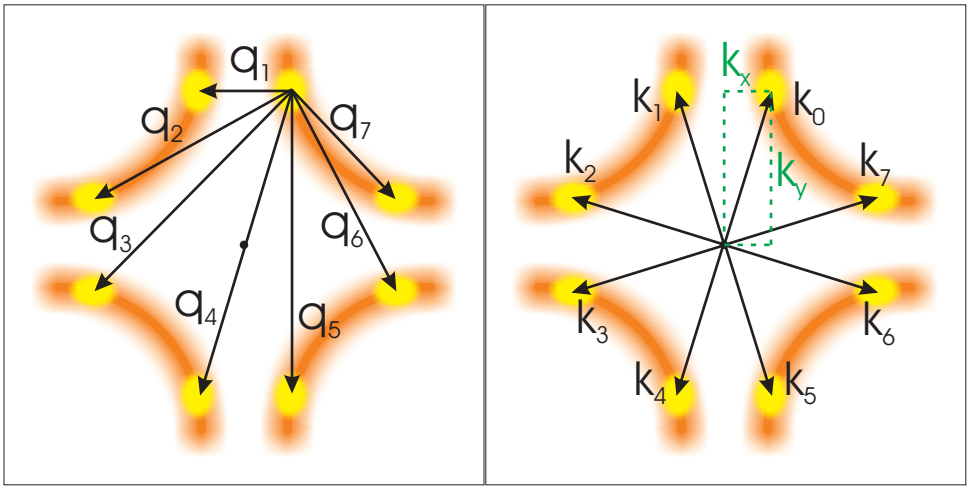

Figure 6.5: (**Left**) The 7 remaining independent q_i vectors after all symmetries are considered. This set of vectors is equivalent to the set of vectors scattering from one single k-space point, as shown in 6.4(B). The q_i labels are canonical. (**Right**) Definition of origin in $\vec{k}$-space results in k_x and k_y as shown. Note that $\vec{k}_1 = k_x\hat{k_x} + k_y\hat{k_y}$, and in addition, the other 7 $\vec{k}_i$ are also simply related to k_x and k_y, due to octet model symmetries.

is no preferred direction in our particular Hamiltonian. This need not necessarily be the case; for example, the "bananas" in the band structure of Figure 6.4 could be elongated in either the $\vec{k}_x$ or the $\vec{k}_y$ direction relative to the other while still obeying all of the symmetries mentioned thus far. However, many Hamiltonian formulations make this assumption, and in the data, we see no anisotropic effects in our quasiparticle interference data which would seem to call for a model preferring one direction over the other. 4-fold isotropic symmetry is equivalent to a diagonal mirror symmetry, or a fold about the line $\vec{k}_x = \vec{k}_y$ as indicated in Figure 6.4(D) (dashed green). Performing this operation reduces the number of scattering vectors from 13 to only 7, due to the additional redundancies. In fact, the 7 remaining vectors are none other than Figure 6.4(B), the original schematic for all possible scatterings (except self-scattering) from a single $\vec{k}_i$. With the symmetries mentioned in this section, we need only consider these 7 $\vec{q}_i$ scattering vectors, which

are given the canonical labels $\vec{q_1}, \vec{q_2}, \ldots, \vec{q_7}$. These labels are shown in Figure 6.5.

6.3 Scattering Fit Methods: Pre-Processing

To improve upon raw data sets before extracting quasiparticle interference peaks, a few minor processing steps are performed before scattering vectors are extracted. It should be emphasized, however, that these modifications change the data only very subtly overall. Several steps are performed to "straighten out" the data, and there are also steps which decrease noise by exploiting the symmetries earlier described.

6.3.1 Processing Before $\vec{q_i}$ Vector Extraction

Although the atomic peaks in Fourier transforms are very close to forming a 4-fold square shape, it is possible that there exists some misalignment. We can correct the problem with the following procedure.

6.3.1.1 Rotate, Skew, and Stretch

Shear piezo drift or slight temperature fluctuations, among other minor effects, can contribute subtly to the imperfection of a lattice represented in Fourier space. Although ideally lattice sites appear as 4 bright peaks (2 pairs of 2-fold symmetric peaks about the origin) in the DFT of the topograph, these peaks do not necessarily form the corners of a perfect square. (It should be noted, however, that any deviations from a perfect square are rarely noticeable by eye.)

In general, lattice locations could appear as in Figure 6.6(A), although once again the deviations are greatly exaggerated for pedagogical clarity. We may perform several basic operations to correct the shape made by the atomic peaks. If

we perform these same operations on $|Z(\vec{q}, E)|$ (or any other quantity of interest), we can eliminate any deviations from the square lattice.

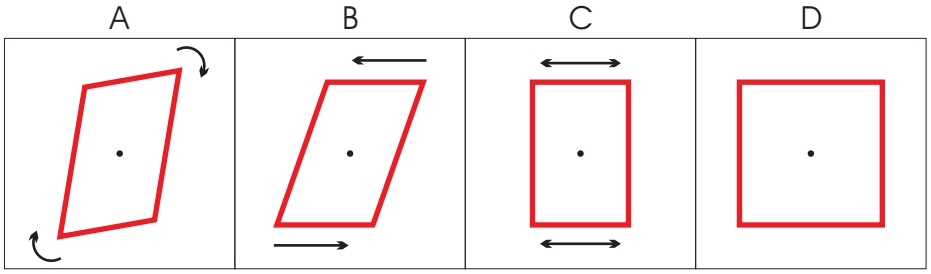

Figure 6.6: (**A**) A schematic representation of a miscalibrated Fourier map. Atomic (lattice) peaks are represented by the corners of the parallelogram. The miscalibration is exaggerated. Arrows indicate rotation operation to be performed. (**B**) After rotation operation. Arrow indicate skew operation to be performed. (**C**) After skew operation. Arrows indicate stretching operation to be performed. (**D**) Symmetrized, square, Fourier data set after stretching operation.

To do this, we first perform a rotation as indicated in Figure 6.6(A), forcing the parallelogram to be parallel with the image axis, as in Figure 6.6(B). Next, we perform a shear operation, symmetrically around the origin, and result in a rectangle as in Figure 6.6(C). Finally, stretching operation will change the rectangle into a square, Figure 6.6(D).

As an example, the final result of performing this operation on one data set from UD45-BSCCO is shown in Figure 6.7(B). Notice that it is not much different from the unprocessed version in Figure 6.7(A); however, we now know that the sample features, angles, and atomic locations are all spaced evenly. This sets the stage for fair comparison between extracted scattering vectors.

6.3.2 Folding

Because we assumed horizontal/vertical mirror symmetry and 4-fold isotropic symmetry in Section 6.2.2, we may overlap, or "fold", our Fourier data onto itself, using

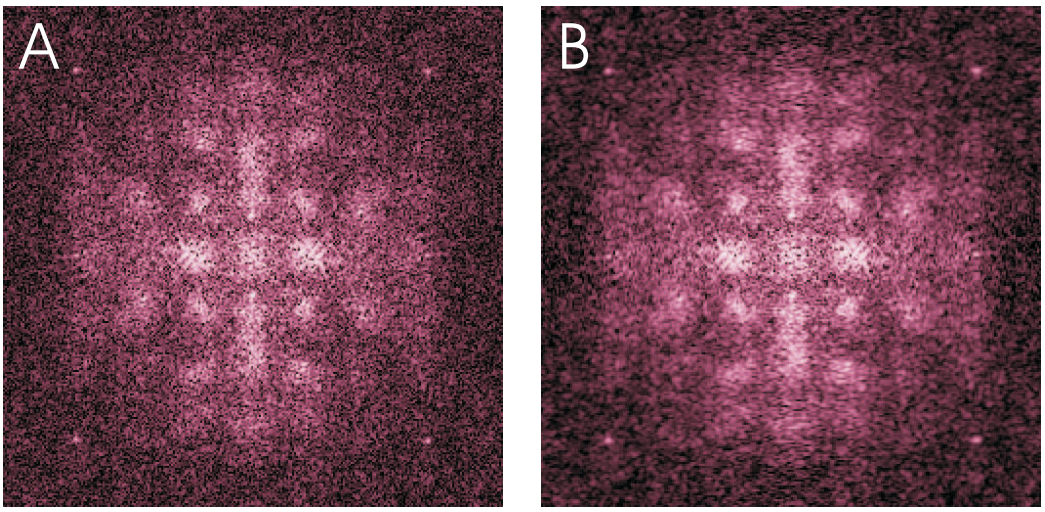

Figure 6.7: (**A**) Raw $\tilde{Z}(\vec{q}, E = 16mV)$. (**B**) $\tilde{Z}(\vec{q}, E = 16mV)$ after rotation, skew, and stretch operations described. The data quality is such that the image is hardly changed after the operations. Most of the data sets analyzed change only subtly with these symmetrization operations.

a mirror symmetry operation. The purpose of this procedure is to enhance S/N even further. In this dissertation, the quasiparticle interference data is folded horizontally (or, equivalently, vertically). However, it is not folded diagonally, although 4-fold isotropic symmetry is assumed when certain $\vec{q}_i$ vectors are used to construct $\vec{k}_x$ and $\vec{k}_y$ (see Section 6.5.2).

6.4 BSCCO Samples Used In Analyses

All fits performed on BSCCO were done in an automated fashion using a customized software package written by me. The data from about one dozen different samples were examined in formulating the ideas and conclusions present here; however; I will concentrate on four particular samples, each with independent doping levels, due to the simple fact that they are of the best quality for the types of analysis to be done here.

In general for all data sets, q_1 and q_7 are the strongest peaks overall in the

Table 6.1: BSCCO Samples Used to Determine Quasiparticle Scattering. DS = Dy Substitution, IO = Interstitial Oxygen. T_C is in Kelvin. p is the doping reported to us by the sample grower, inferred based upon the weighted results of several different probes, including magnetic susceptability (T_C), resistivity/hall coefficient, optical conductivity, mean gap values (STM), and Fermi surface volume (ARPES). p_P is the calibrated[19] doping value for equivalent T_C and with T_C^{max}=92K. $\overline{\Delta}$ is the average value of the sample gap measured from hundreds of thousands of energy-dependent STS curves.

BSCCO Samples Used to Determine Quasiparticle Scattering					
Doping Method	T_C	p	p^P	$\overline{\Delta}$	Underdoped?
DS/IO	20	0.06	0.0627	99	Yes
DS/IO	45	0.08	0.0814	85	Yes
IO	74	0.14	0.111	48	Yes
IO	89	0.19	0.180	33	No

energy ranges of interest, followed by q_5 for the higher energy ranges, then q_2 and q_6, and finally q_3 and q_4, which are rarely discernable if at all.

6.5 Octet Model Algebra and Fitting Methods

Here I discuss how scattering vectors are fit, and what mathematical relationships in the octet model are exploited in order to arrive at high spectral weight points in $\vec{k}$-space.

6.5.1 $\vec{q}$ vector Methods

All $\vec{q}_i$ vectors are fitted automatically with a computer algorithm written by the author. See Figure 6.8 for a schematic of the locations of the typical locations of the peaks in $\vec{q}$-space. The odd numbered vectors, $\vec{q}_1$, $\vec{q}_3$, $\vec{q}_5$, and $\vec{q}_7$, were found by extracting a 1D linecut from $\left|\tilde{Z}(\vec{q},E)\right|$ and locating the peak. An example 1D extraction linecut is shown in Figure 6.9. Peaks were chosen within a particular window around a "guess" point. The guess point is equal to the peak location of

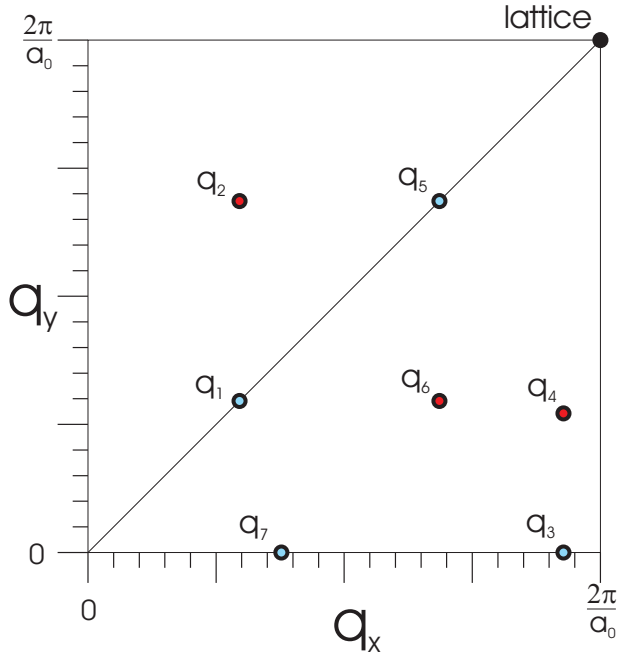

Figure 6.8: Schematic of Typical Scattering Vector Locations. The peak centers colored in blue are fit using a 1D Gaussian linecut, and the peaks colored in red are fit using a 2D Gaussian grid. The atomic (lattice) peak is shown in **black**.

the previously fitted energy. For the first point, a best guess is used for the guess point based upon expected values for the particular $\vec{q}_i$ in question. The image showing the same fitted vector in $\vec{q}$-space is shown in Figure 6.10.

To choose peaks, a 1D Gaussian function with linear background was used to fit the locations of the peaks *within the chosen window only*. The Gaussian takes the form

$$Ae^{-\frac{1}{2}(\frac{x-x_0}{\sigma})^2} + Bx + C \tag{6.3}$$

where A, x_0, σ, B, and C are the fit parameters. The fitted $\vec{q}$ vector is the centroid (x_0) of the Gaussian function.

The even numbered vectors, $\vec{q}_2$, $\vec{q}_4$, and $\vec{q}_6$, are found by directly fitting a 2D

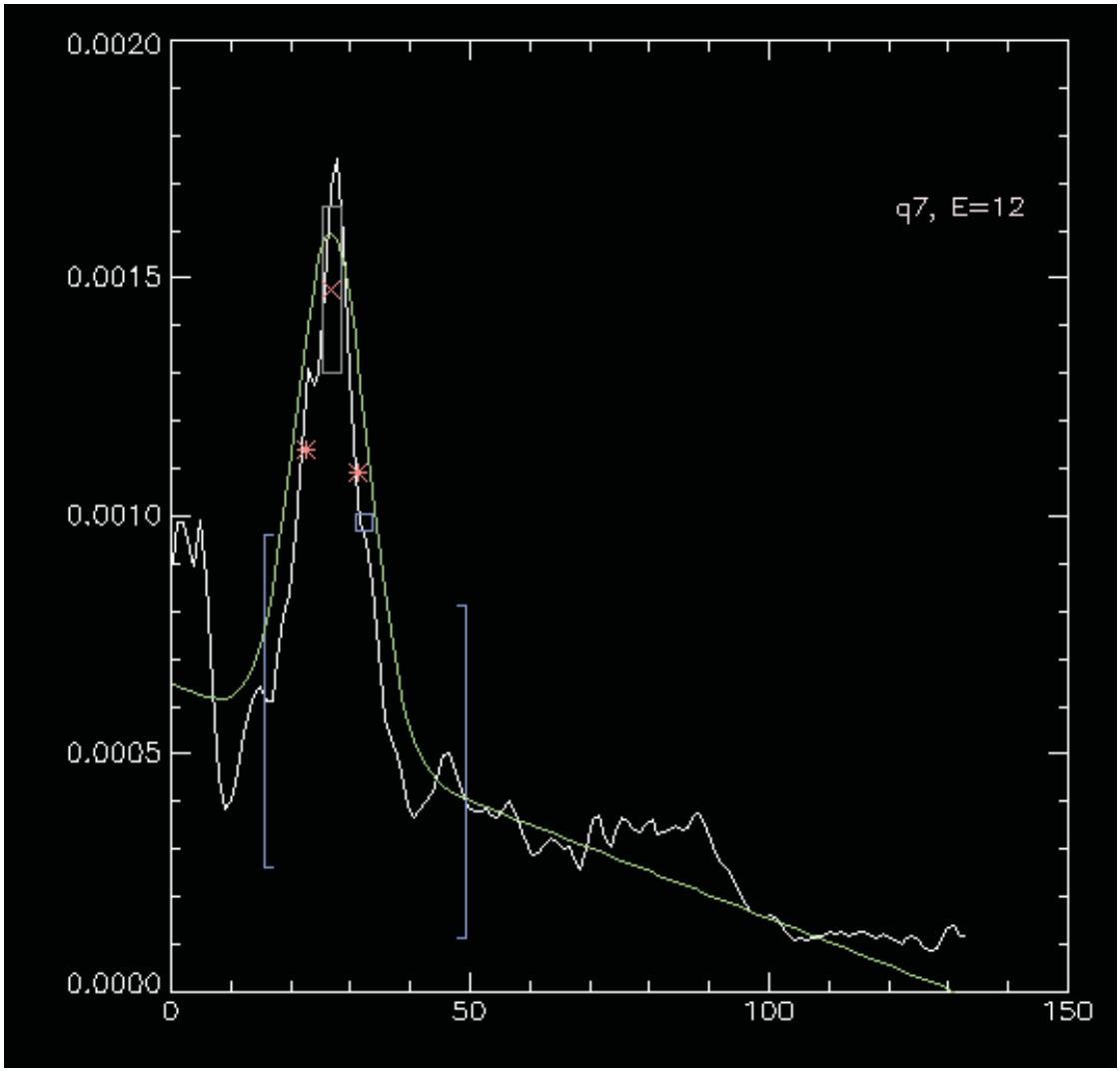

Figure 6.9: Example of Fitted $\vec{q}$ Using a 1D Linecut. (**Left**) 1D Linecut Plot. The "guess point" is marked as a blue square (□), and the bounding guess window around it is shown as tall, blue, left ([) and right (]) square brackets. The centroid of the Gaussian, which is the fitted location of the $\vec{q}$ vector, is displayed as a red x (×), and the $1-\sigma$ standard deviations are marked on either side of the centroid as red asterisks (∗). The Gaussian itself is displayed in green (-), and the error on the $\vec{q}$ vector fit is displayed as tall, gray, left ([) and right (]) square brackets.

Gaussian on $\left|\tilde{Z}(\vec{q},E)\right|$ at a guess point. The 2D Gaussian is

$$Ae^{-\frac{1}{2}[(\frac{x-x_0}{\sigma_x})^2+(\frac{y-y_0}{\sigma_y})^2]}+C \tag{6.4}$$

where A, x_0, σ_x, y_0, σ_y, and C are the fit parameters. The fit is allowed to

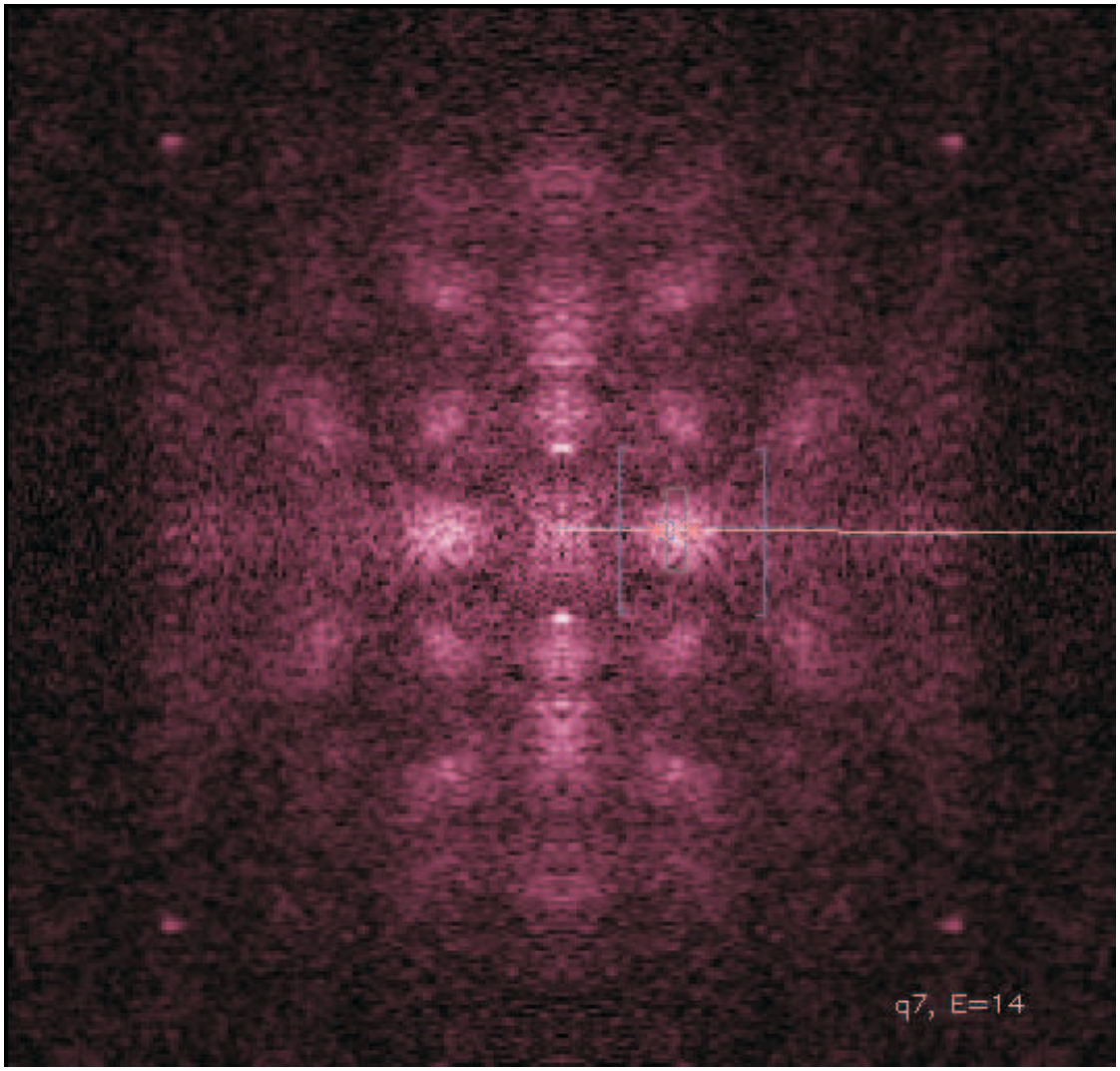

Figure 6.10: 2D Image Associated with Fitted $\vec{q}$ Using a 1D Linecut. Corresponding quasiparticle interference image from which the linecut is extracted. The colors and shapes of the icons are the same as in Figure6.9.

tilt at any angle which the data dictates, with spreads given by σ_x and σ_y. The centroid is given by the coordinate (x_0,y_0).

Points are excluded from the $\vec{q}$ fit plots as soon as the fits begin to fail. They usually fail because the the peaks gradually lose their signal and fall down into the measurement noise. There is significance to this behavior which will be discussed in later sections.

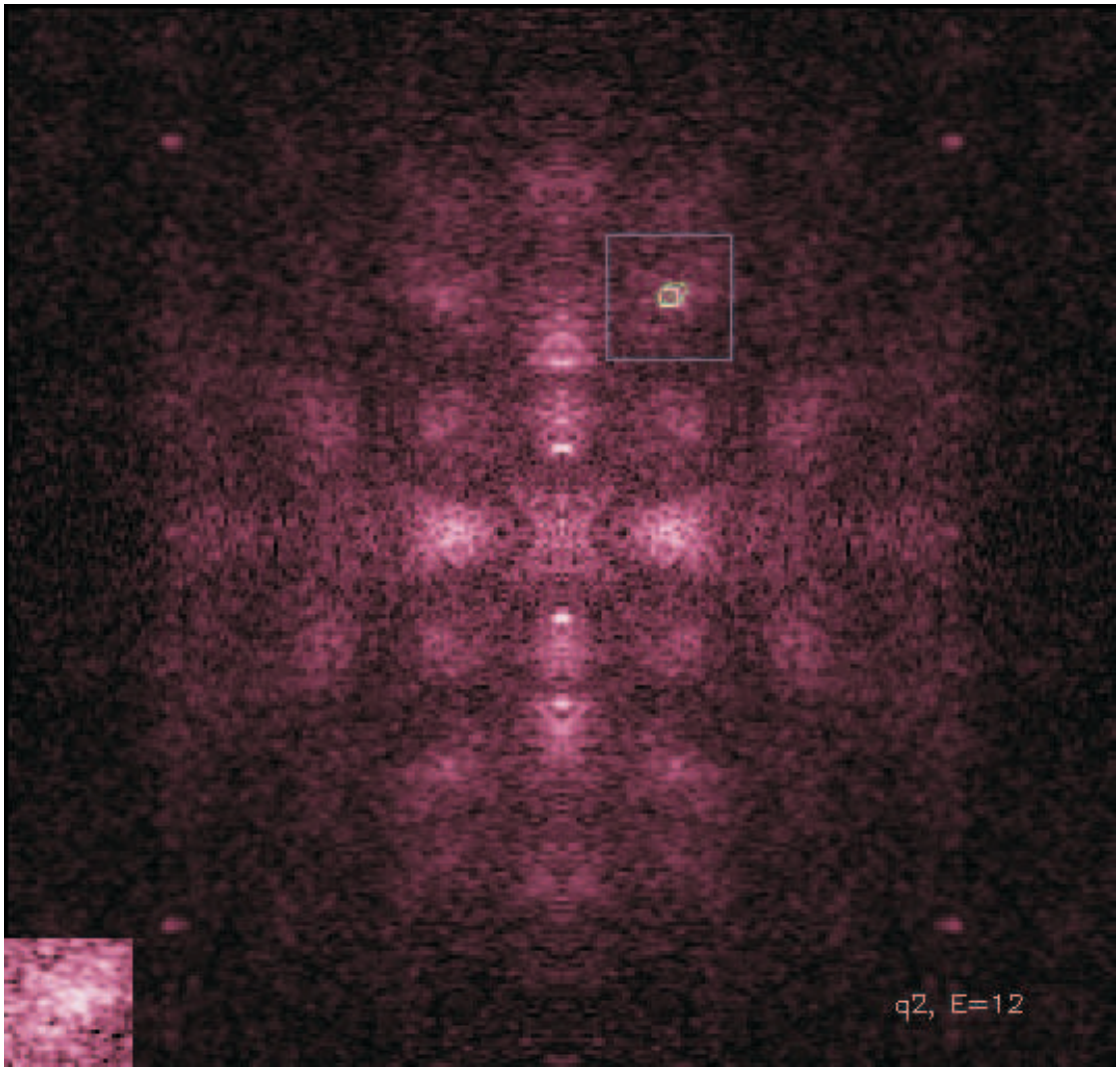

Figure 6.11: Example of Fitted $\vec{q}$ Using a 2D Gaussian. The "guess point" is marked as a white square (■), and the bounding guess window around it is shown as large blue box (□). The centroid of the Gaussian, which is the fitted location of the $\vec{q}$ vector, is displayed as a green x (×). There are two $1-\sigma$ standard deviations, σ_x and σ_y, one for each orthogonal direction. The spread of the Gaussian is indicated by a green oval (O) whose tilt angle and size is dependent on the best fit to the data for σ_x and σ_y. (**Inset**) A rescaled version of the peak found inside the blue box.

6.5.2 $\vec{k}$ vector Methods and Algebra

Once the $\vec{q}_i$ are known (for each energy), we may use octet model algebra as well as known symmetries (Section 6.2.2) to determine k_x and k_y, as shown in Figure

6.5. Multiple combinations of the $\vec{q}_i$ can give k_x and k_y algebraically; however, many of these combinations are redundant due the symmetries discussed. Also, in practice, there are a very large (perhaps infinite) number of ways to use the 7 equations specified in Section 6.2.1 to find k_x and k_y. Finding combinations which are more complicated than the minimal set of relationships among q_i vectors serves no purpose, though, since more complicated relationships are not mathematically independent of the minimal set.

I now discuss various minimal combinations of $\vec{q}_i$ vectors, one at a time. It turns out (shown below) that, mathematically, $\vec{q}_2$, $\vec{q}_4$, and $\vec{q}_6$ each independently determine a k_x and k_y pair completely. Hence, each one of those vectors constitutes a combination itself, and there is no need to combine them with any other vector. This leaves $\vec{q}_1$, $\vec{q}_3$, $\vec{q}_5$, and $\vec{q}_7$ as possible vectors to use with others among the same group to make combinations. In addition, and unfortunately, I find vectors $\vec{q}_3$ and $\vec{q}_4$ to be prohibitively weak in my investigations. For those two particular vectors, the S/N is not enough to be able to make a definitive statement about their placement. Therefore, we are left with only 5 combinations, which are described below.

Recall from figure 6.5 that

$$\vec{k}_0 = k_x\hat{k_x} + k_y\hat{k_y} \tag{6.5}$$

I will select various equations from the set in Figure 6.2, with $j = 0$ to represent the reduced set of $\vec{q}_i$ vectors in Figure 6.5 (or, equivalently, scattering from just one initial $\vec{k}$-space point $\vec{k}_0$). I label $\vec{k}$-space points in a counter-clockwise fashion starting from $\vec{k}_0$.

6.5.2.1 $\vec{q}_1$ and $\vec{q}_7$ Combination

$$\vec{q}_1 = \vec{k}_1 - \vec{k}_0 = \begin{pmatrix} -k_x \\ k_y \end{pmatrix} - \begin{pmatrix} k_x \\ k_y \end{pmatrix} = \begin{pmatrix} -2k_x \\ 0 \end{pmatrix} \tag{6.6}$$

$$\therefore k_x = -\frac{q_{1x}}{2} \tag{6.7}$$

$$\vec{q}_7 = \vec{k}_7 - \vec{k}_0 = \begin{pmatrix} k_y \\ k_x \end{pmatrix} - \begin{pmatrix} k_x \\ k_y \end{pmatrix} = \begin{pmatrix} k_y - k_x \\ k_x - k_y \end{pmatrix} \tag{6.8}$$

$$\therefore k_y = q_{7x} + k_x \tag{6.9}$$

Notice that diagonal mirror symmetry (Section 6.2.2 is implicitly assumed in this relating $\vec{q}_1$ and $\vec{q}_7$ in this manner.

6.5.2.2 $\vec{q}_1$ and $\vec{q}_5$ Combination

k_x is determined from Equation 6.7.

$$\vec{q}_5 = \vec{k}_5 - \vec{k}_0 = \begin{pmatrix} k_x \\ -k_y \end{pmatrix} - \begin{pmatrix} k_x \\ k_y \end{pmatrix} = \begin{pmatrix} 0 \\ -2k_y \end{pmatrix} \tag{6.10}$$

$$\therefore k_y = -\frac{q_{5y}}{2} \tag{6.11}$$

6.5.2.3 $\vec{q}_5$ and $\vec{q}_7$ Combination

k_y is determined from Equation 6.11 and k_x is determined by inverting Equation 6.9 to read

$$\therefore k_x = k_y - q_{7x} \tag{6.12}$$

6.5.2.4 $\vec{q}_2$ Alone

$$\vec{q}_2 = \vec{k}_2 - \vec{k}_0 = \begin{pmatrix} -k_y \\ k_x \end{pmatrix} - \begin{pmatrix} k_x \\ k_y \end{pmatrix} = \begin{pmatrix} -k_y - k_x \\ k_x - k_y \end{pmatrix} \tag{6.13}$$

Solving these two simultaneous equations results in

$$k_x = \frac{q_{2y} - q_{2x}}{2} \tag{6.14}$$

and

$$k_y = -\frac{q_{2y} + q_{2x}}{2} \tag{6.15}$$

6.5.2.5 $\vec{q}_6$ Alone

In a similar manner as above, I find from $\vec{q}_6$ alone

$$k_x = -\frac{q_{6x} + q_{6y}}{2} \tag{6.16}$$

and

$$k_y = \frac{q_{6x} - q_{6y}}{2} \tag{6.17}$$

6.5.3 E vs. θ_k

For each k_x/k_y pair found for a particular $\vec{q}$ combination, a point appears on the Fermi surface in $\vec{k}$-space (see Figure 6.12). Each point determines a unique angle in $\vec{k}$-space defined as θ_k. Another way (and a quite insightful one) to display the measured dispersion is by plotting E versus θ_k. Such plots are discussed in Section 6.6.3 for the actual data.

6.6 Fit Results

Results of $\vec{q}_i$ fit points and the quantities calculated from them are given here.

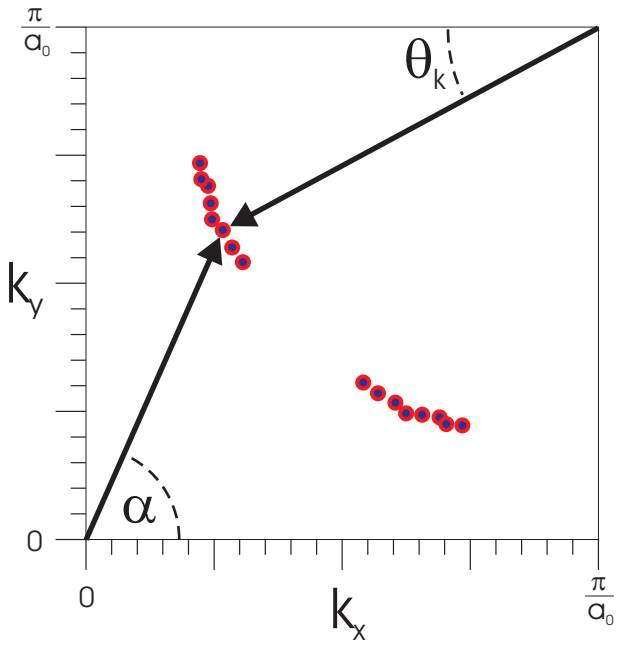

Figure 6.12: Schematic of $\vec{k}$-space. Several determined k_x and k_y points, for different energies, are plotted as an example. θ_k angle is defined as indicated.

6.6.1 $\vec{q}_i$ Scattering Vector Fits

Scattering vector fits are shown in Figure 6.13 for several dopings. The curves connecting each fitted point are the so-called "loci of scattering" which are used as an internal consistency check for the $E(\theta_k)$ model fit (shown in Section 6.6.3).

6.6.2 $\vec{k}_i$ Fermi Surface Fits

Using the points found in $\vec{q}$-space, I then determine corresponding points in $\vec{k}$-space using the $\vec{q}_i$ vector combinations previously discussed. All practical combinations are used in the fits, but none for which the $\vec{q}$ vector fit failed. Quarter-circles are fit to the resulting Fermi arcs for an initial parameterization of the dispersion. The centers of the quarter-circles are constrained to the line $k_y = k_x$, but can otherwise move freely, and the radii are unconstrained.

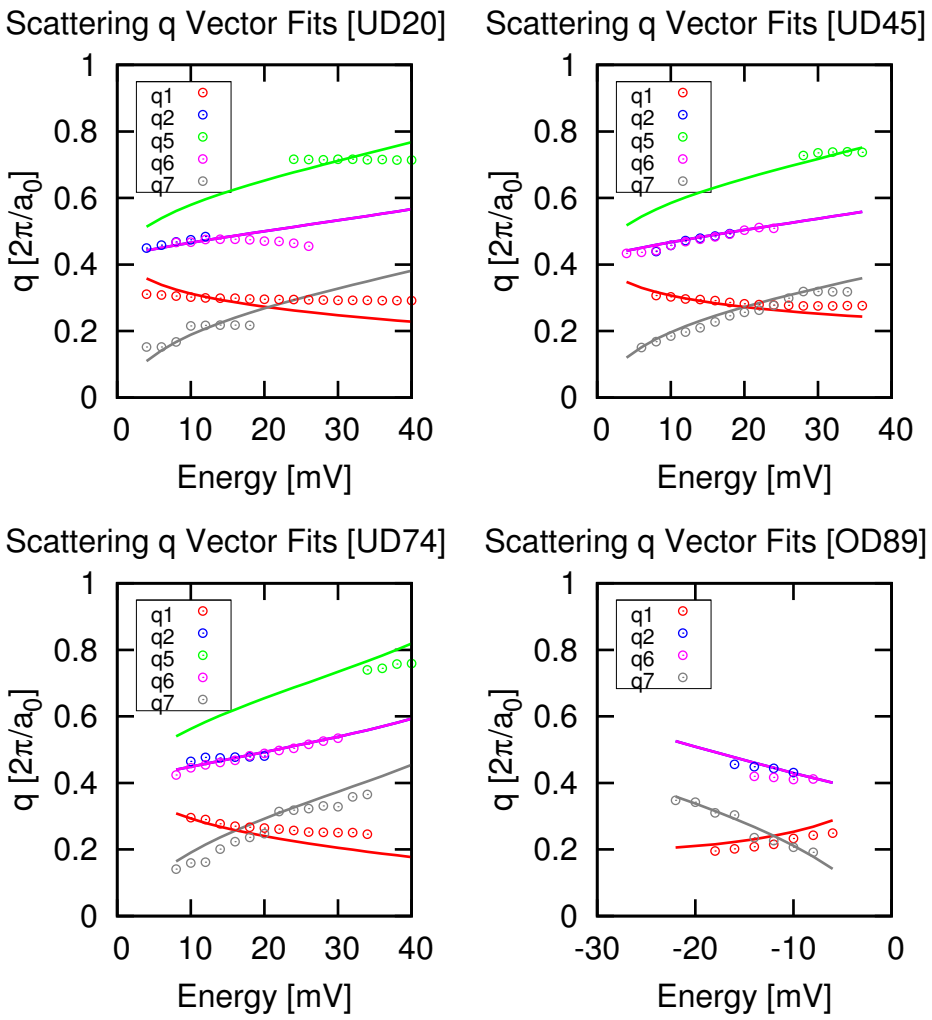

Figure 6.13: Scattering Vectors ($\vec{q}_i$) Fits from $\tilde{Z}(\vec{q}, E)$. (**Top Left**) UD20, (**Top-Right**) UD45, (**Bottom-Left**) UD74, (**Bottom-Right**) OD89. Lines represent the 'loci of scattering' which is an internal consistency check to see how well the final formulation, the overall E vs. θ_k fit (see Figure 6.16), mimics the original scattering vectors.

6.6.3 E vs. Θ_k

Plots of the dispersion $E(\theta_k)$ of UD45 BSCCO are shown in Figure 6.15 for all relevant combinations of scattering vectors. The statistically averaged plots are shown in Figure 6.16 for each of the BSCCO samples. These were created in a similar manner as the statistically averaged plots in $\vec{k}$-space, with the horizontal error

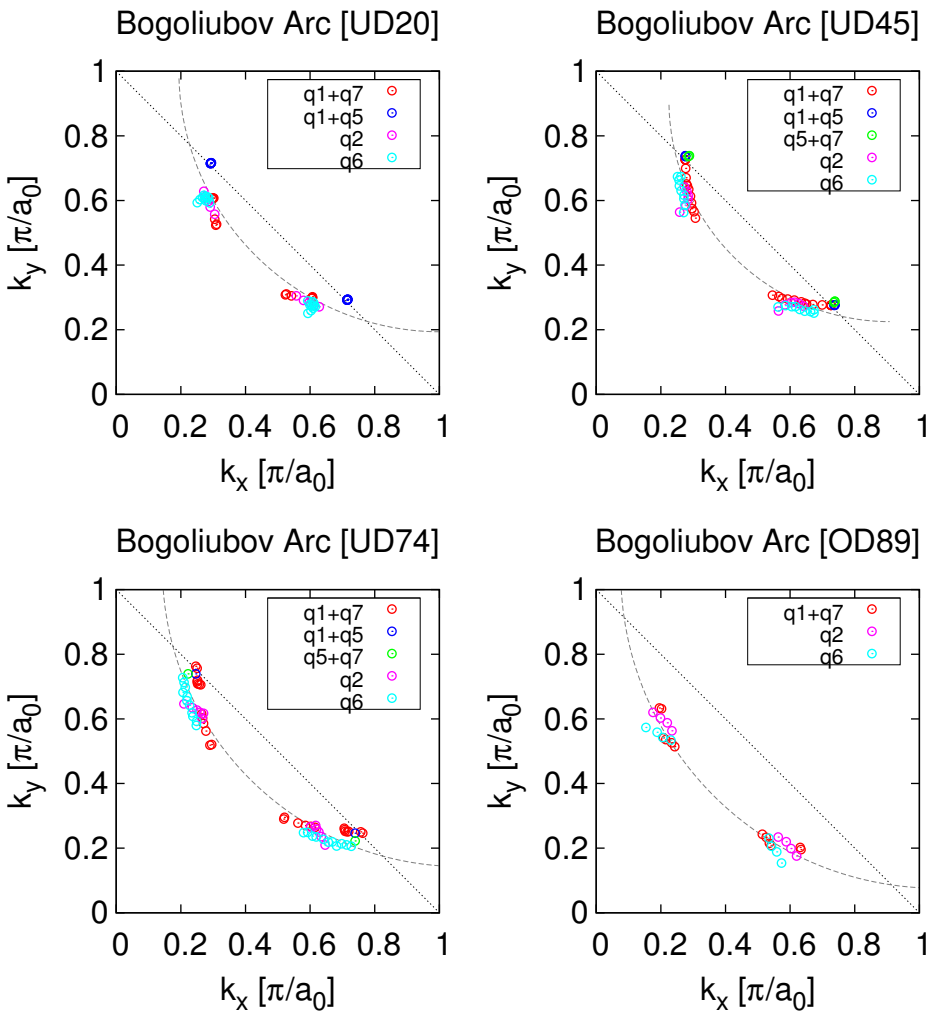

Figure 6.14: Fermi Surface Fits in $\vec{k}$-space for Relevant $\vec{q}_i$ Combinations and All Dopings. (**Top Left**) UD20, (**Top-Right**) UD45, (**Bottom-Left**) UD74, (**Bottom-Right**) OD89. The points are fit to a quarter-circle with a center offset to fit the data optimally. The radii and centers of these quarter-circles are as follows: **UD20**, Radius=0.808, center=(1.002,1.002); **UD45**, Radius=0.684, center=(0.909,0.909); **UD74**, Radius=0.923, center=(1.067,1.067); **OD89**, Radius=0.979, center=(1.055,1.055)

bars representing the standard deviations of θ_k based upon different combinations of scattering vectors.

To go further, we may identify a model which we believe will explain the type of dispersion we see. The $d_{x^2-y^2}$ symmetry is chosen as a model for the cuprates be-

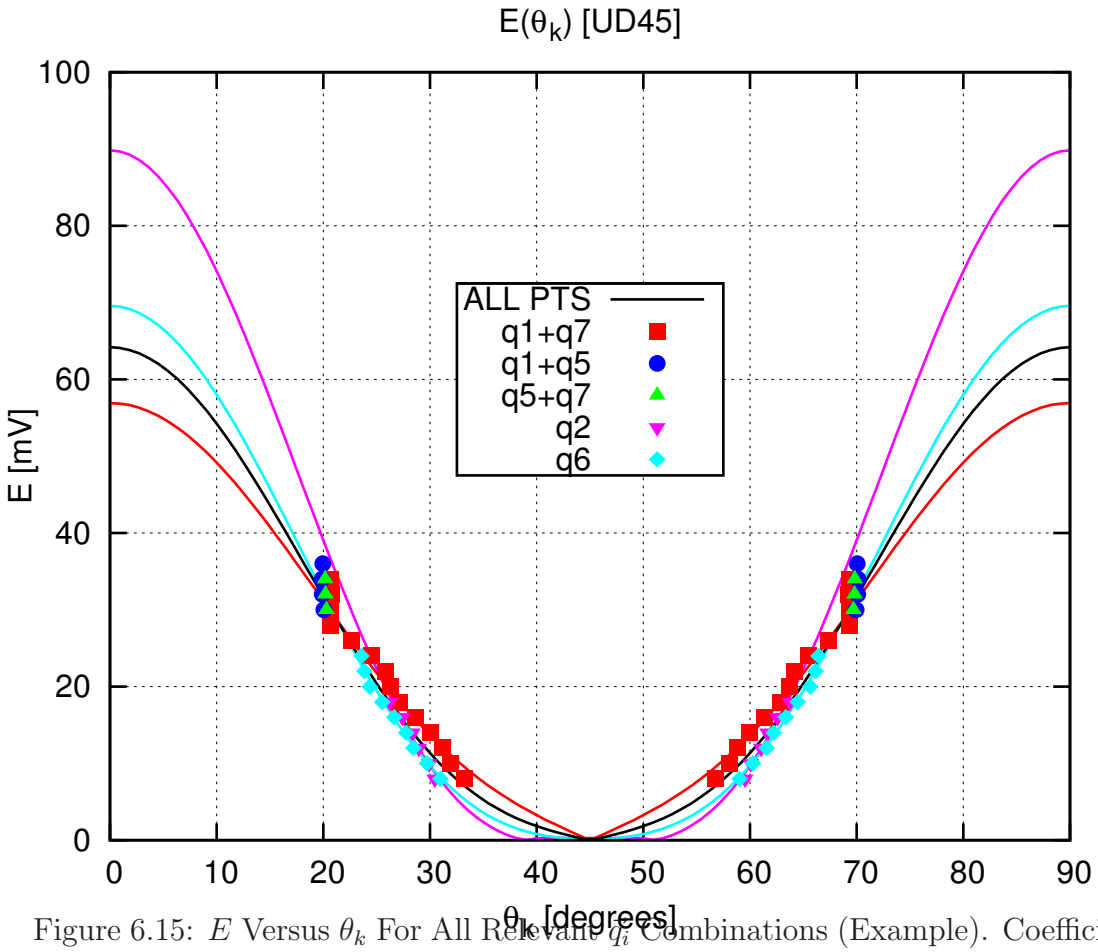

Figure 6.15: E Versus θ_k For All Relevant q_i Combinations (Example). Coefficient fits for Equation 6.21 are as follows: **q1&q7**, Δ=56.9, A=0.827, B=0.173; **q2**, Δ=89.8, A=0.738, B=0.262; **q6**, Δ=69.6, A=0.760, B=0.240; **ALL PTS**, Δ=64.2, A=0.785, B=0.215

cause they are a d-wave superconductors (see Section 3.6), and the order parameter (Δ_k) is anisotropic,[22] as follows:

$$\Delta_k = \Delta_0'(k_x^2 - k_y^2) = \Delta_0'|\vec{k}|(cos^2(\alpha) - sin^2(\alpha)) \equiv \Delta_0 cos(2\alpha) \tag{6.18}$$

where $\alpha \equiv tan^{-1}(\frac{ky}{kx})$.

The last expression is also the form which the angular dependence of solutions to the Schrodinger Equation takes for $l = 2$ and $m = \pm 2$.[8] (The relevant spherical harmonics are $Y_{l=2}^{m=\pm 2}$.) However, this expression is but one way to satisfy $d_{x^2-y^2}$ symmetry. The next-highest harmonic of $cos(2\alpha)$ which satisfies the d-wave symmetry is $cos(6\alpha)$ (see Figure 6.17). This harmonic can be shown to be related to next-nearest neighbor hopping in a tight-binding model.[4] If we allow this

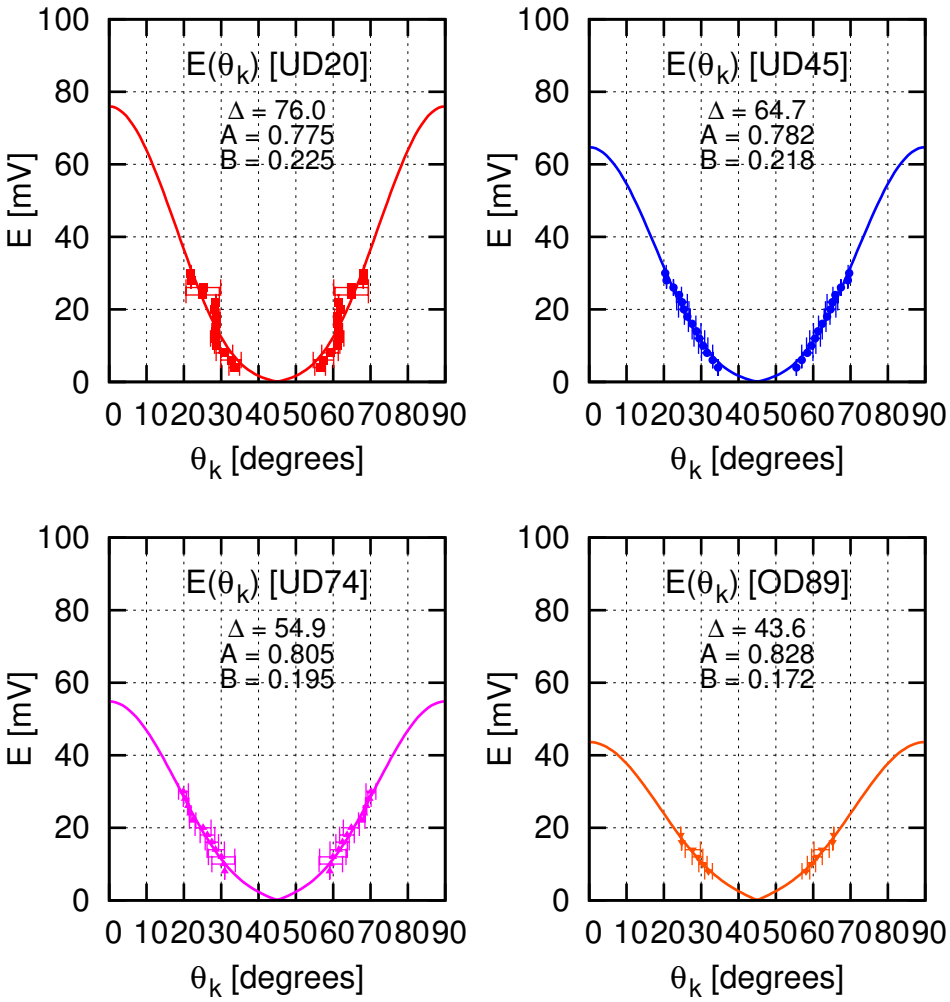

Figure 6.16: (**Top Left**) UD20, (**Top-Right**) UD45, (**Bottom-Left**) UD74, (**Bottom-Right**) OD89. Energies > 30mV are omitted from the fits. Coefficients fit to Equation 6.21 are given.

higher-order Fourier term to be included in the order parameter function, we have

$$\Delta(\alpha) = \Delta_{max}(Acos(2\alpha) + Bcos(6\alpha)) \tag{6.19}$$

where I require $A + B = 1$ so that the maximum value of the order parameter is properly normalized.[4]

Instead of the angle α, however, we elect to use the angle θ_k, defined in Figure

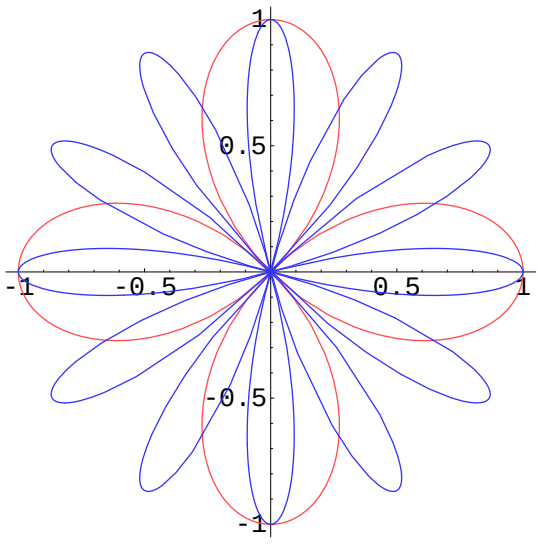

Figure 6.17: Simplest Orbital Harmonics Satisfying D-Wave Symmetry. The expression $cos(2\alpha)$ (red) is a simple $d_{x^2-y^2}$ formulation, and $cos(6\alpha)$ (blue) is the next highest order term in the Fourier expansion which also satisfies the d-wave symmetry.

6.12 and equal to

$$tan(\theta_k) = \frac{1 - k_y}{1 - k_x} \tag{6.20}$$

in our analyses. There are several reasons for this choice. First, the convention to use the $\left(\frac{\pi}{a_0}, \frac{\pi}{a_0}\right)$ point as the origin of the vector pointing to Fermi surface points is established by ARPES studies[4] and prior STM studies.[15] The origin of the vector constituting this angle, $\left(\frac{\pi}{a_0}, \frac{\pi}{a_0}\right)$, is commonly referred to as the center of the "hole-pocket", which is the "hole-like" region which the Fermi arc would surround if it were connected with a circular shape in the extended Brillouin zone. Second, θ_k serves as a good parameterization for the data because the band structure approximates a quarter-circle with the $\left(\frac{\pi}{a_0}, \frac{\pi}{a_0}\right)$ point (or a nearby point) as its center. This being the case, we write

$$\Delta(\theta_k) = \Delta_{max} \left| Acos(2\theta_k) + Bcos(6\theta_k) \right| \tag{6.21}$$

where we plot the magnitude of Equation 6.19, which we must do because

negative energy values are not defined for tunneling asymmetry maps anyway. Equation 6.21 represents a d-wave angular dependence centered at the hole-pocket.

It is clear from this formulation that $\Delta(\theta_k \rightarrow 0) = \Delta_{max}$. If one then asks what the behavior of Δ_{max} is with doping, we can see that it increases as doping is decreased.

6.7 QPI vs. p for all relevant dopings

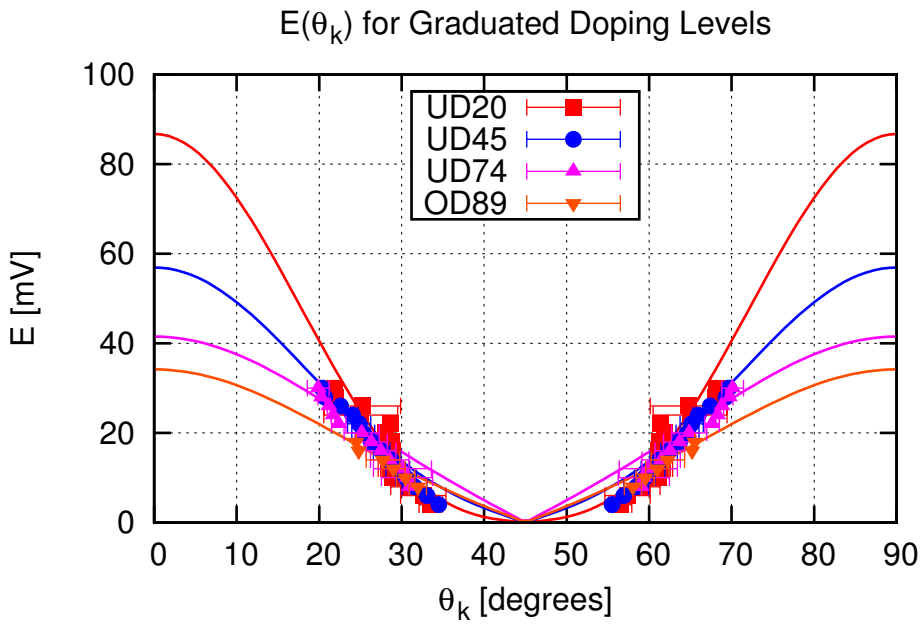

Figure 6.18: $E(\theta_k)$ for Graduated Doping Levels. Band structure spectral weight peaks versus Θ_k for energy range bearing detectable quasiparticle interference. Several BSCCO Samples at various dopings are shown.

In Figure 6.18, it is very apparent that decreased doping results in increased Δ_{max}. This eludes to the possibility that Δ_{max} may be important to qualifying the underdoped (pseudogap) phases. The nature of the argument based upon the order parameter in the previous section, upon which Equation 6.21 is obtained, along with the striking fact in Figure 6.18 that each doping produces a different

$\Delta(\theta_k \rightarrow 0)$, suggests that Δ_{max} may be a measure of the magnitude order parameter, or perhaps of the doping. Because only the quasiparticle states of a d-wave superconductor could exhibit this internally consistent and particle-hole symmetric set of interference wavevectors ($\vec{q}_i$), there is strong motivation to believe that the gap determined by these investigations is the superconducting energy gap.

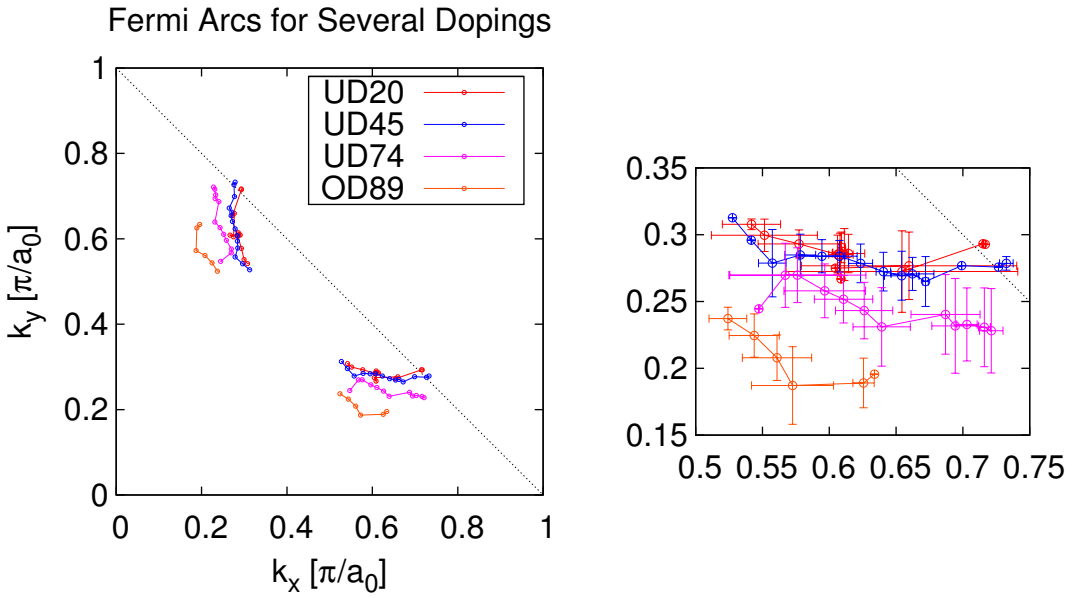

Figure 6.19: $\vec{k}$-space locations of High Dispersion Fermi Surface Points determined via quasiparticle scattering. Each point is the statistical average of all $\vec{k}$ points for one particular energy. (**Inset**) A zoomed-in version of the lower half of $\vec{k}$-space points. The bidirectional error bars shown are the standard deviations propagated from the $\vec{q}_i$.

Statistically determined points in $\vec{k}$-space are show in Figure 6.19. Each point represents the statistical average of each point found at a particular energy using various combinations of $\vec{q}_i$. Error bars come from the standard deviation of number of $\vec{k}_i$ points for any given energy. Notice that, as T_C (and hence doping) decreases, so does the size of the Fermi arcs. Notice also that the arcs tend to have a definite point of termination in each case, rather than ending in a disordered array of

random points. I will return to both these observations shortly.

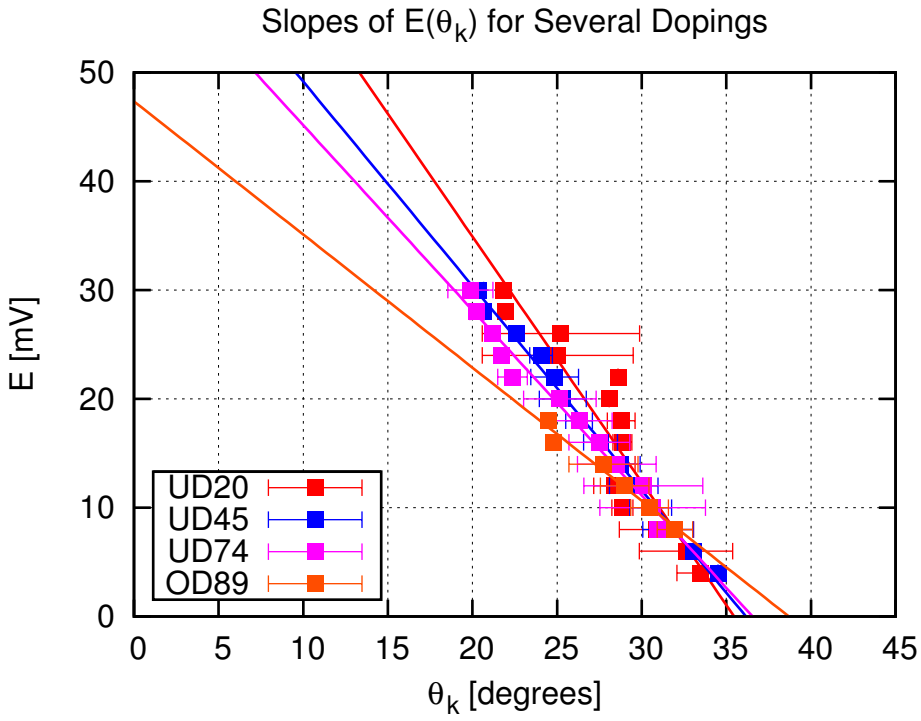

Figure 6.20: Slopes of $E(\theta_k)$ for Several Dopings. A simple best fit line to the $E(\theta_k)$ demonstrates decreased slope with increased doping.

It is also possible to fit a line to the dispersive points in the $E(\theta_k)$ plots. This is shown in Figure 6.20, which demonstrates that the slopes of the lines increase as doping is decreased, in a similar manner as Δ_{max}.

6.8 Comparing D-Wave Fit Gap Values to Average Spectra Gap

Average gap values may be obtained via point spectra in a manner discussed in Section 3.7.1. One may compare the extrapolated fit values shown in Figure 6.18 to these average spectra gaps to see how well they match. This comparison is

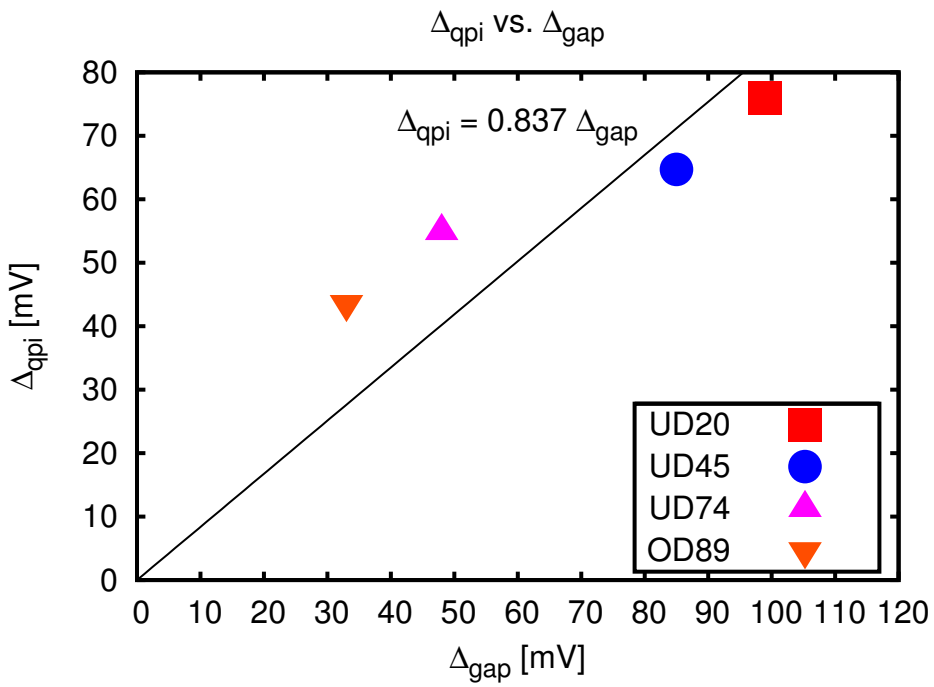

Figure 6.21: Comparison of Fit Magnitudes to Average Gaps from Spectra. Although simple proportionality between the two values is not apparent, the best fit line shows good correlation between the two parameters (The reduced χ^2 is 7.6, which corresponds to a 94.4% probability confidence for the fit.

shown in Figure 6.21.

As is evident from the fit, there does not appear to be a simple proportionality relationship between Δ_{qpi} and Δ_{gap}. However, there is a clear correlation between the two parameters: as Δ_{qpi} increases, so does Δ_{gap}. Moreover, the best fit line has a relatively low deviation from the points themselves; χ^2 is 7.6, which corresponds to a 94.4% confidence probability for the line fit. This may indicate that $\Delta_(\theta_k \rightarrow 0)$ could be a yet undetermined measure of the order parameter.

Further, it is instructive to compare the gaps calculated using the d-wave angular fit to the doping levels of each sample. Figure 6.22 shows the fit magnitude (Δ_{qpi}) for various doping levels. The comparison is suggestive of some correlation

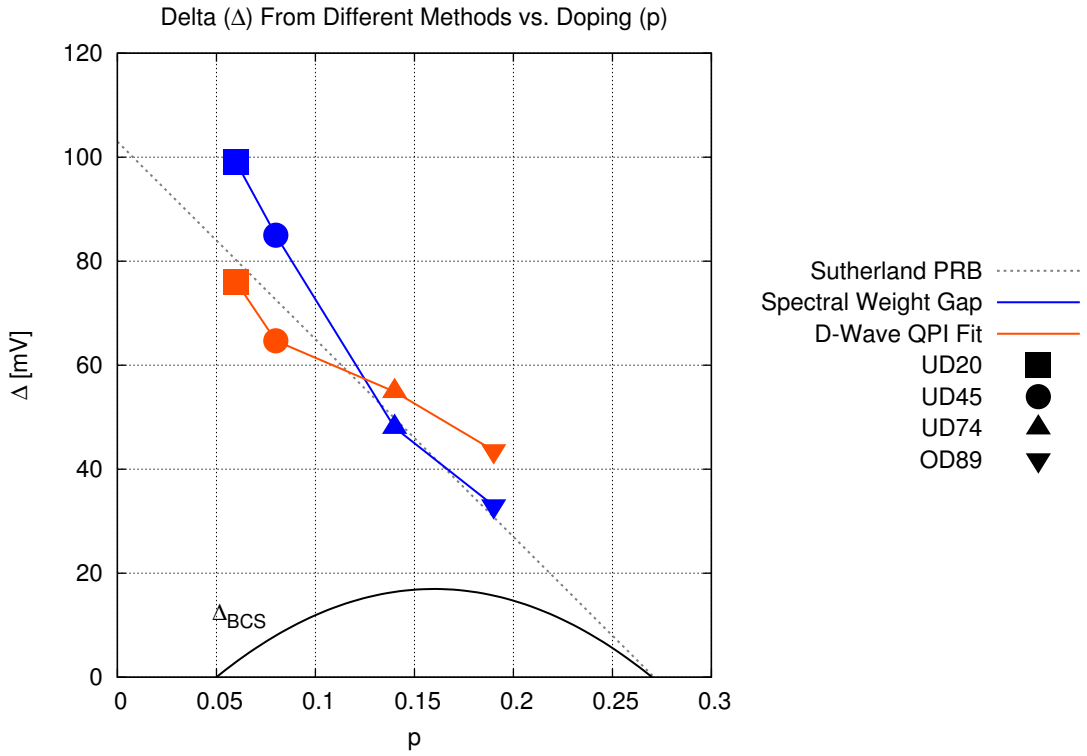

Figure 6.22: Higher Energy Scale Parameter For Several Dopings. Δ_{qpi} and Δ_{gap} are plotted as a function of p. In addition, the fit line from Sutherland, et. al. is included as a guide to the eye. The doping levels (p) are the weighted values as in Table 6.1. The spectral gap values are also given in that table.

between Δ_{qpi} and heat transport measurements from Sutherland, et. al.[20] More recently, Hüfner,[12] et. al. describe additional correlations from various probes which also are consistent with the two energy scale/gap picture (see Figure 6.23).

6.9 Termination Energies

At some energy around 30mV in BSCCO, the quasiparticle scattering peaks $\vec{q}$ fade away into the background noise. However, a few peaks, $\vec{q}_1$ and $\vec{q}_5$, exist indefinitely above 30mV. These peaks are given the names $\vec{q}_1^*$ and $\vec{q}_5^*$ when they have entered into their nondispersive state above 30mV. The other peaks which

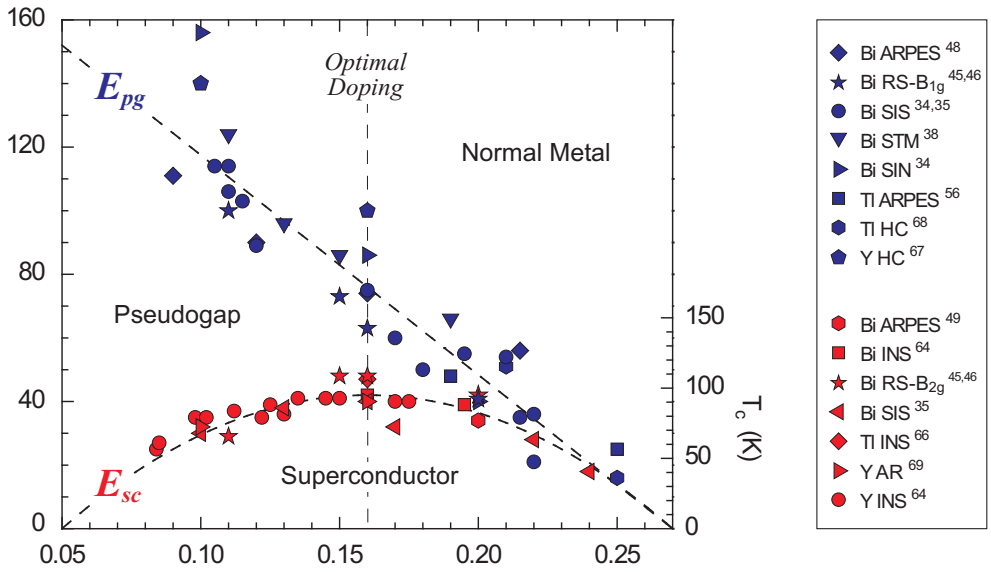

Figure 6.23: Pseudogap and Superconducting Gaps Measured With Various Probes.[12]

fade away tend to do so within just a few mV of each other, making it possible to define a "termination energy" at which the quasiparticle peaks are no longer a significant feature in Fourier space.

Do the quasiparticle interference patterns in Fourier space disappear because the scattering ceases around the termination energy, or instead, do the quasiparticles themselves fade away, eventually disappearing somewhere near the termination energy? According to rigorous spectral analyses,[2] scattering clearly remains in effect even beyond termination energy. Thus, it is reasonable to assume some kind of transition from the lower-energy (10-30mV) state in which quasiparticles are quite vivid to the higher-energy (¿30mV) state in which quasiparticles are virtually absent.

As indicated in Figure 6.19, quasiparticle scattering peaks reach a limit due to

weakening of intensity at a location which appears to be very close to the line

$$k_y = 1 - k_x \tag{6.22}$$

(Although in Figure 6.19 the OD89 sample may not appear to extend entirely to the zone face, this is because that data set was not optimized for higher-energy quasiparticle interference studies, and my conservative analysis of the termination energies finds a minimal set of $\vec{k}$-space points. Future investigations[13] may reveal more complete information about the termination of the QPI in optimally doped cuprates. Further, though there are fewer points, the quarter-circle fits to the OD89 data are still consistent with the doping evolutions expected in Figures 6.14 and 6.25.)

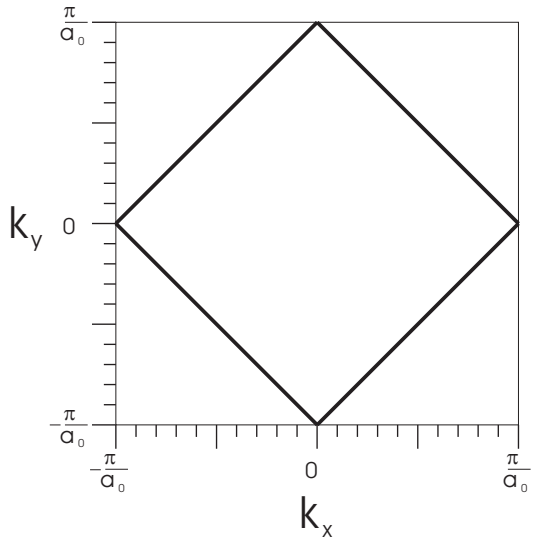

Figure 6.24: $\sqrt{2} \times \sqrt{2}$ Boundary. The outer square is the first Brillouin zone, and the solid black line, half the area of the first Brillouin zone, denotes the $\sqrt{2} \times \sqrt{2}$ boundary. This boundary is also the same as that of the antiferromagnetic Brillouin zone reconstruction.

The boundary (see Figure 6.24) is exactly half the size of the first canonical Brillouin zone, with a boundary (face) lying halfway between the Γ point ($k_x, k_y =$

0) and the $(\pm\frac{\pi}{a_0}, \pm\frac{\pi}{a_0})$ points. This zone has area $\sqrt{2} \times \sqrt{2}$, in units of a lattice constant (a_0).

The observation that QPI peaks appear to extinguish at the $\sqrt{2} \times \sqrt{2}$ boundary implies several possibilities, since this boundary may be related to key physical aspects of the system. First and foremost, the line in Equation 6.22 denotes the boundary between the first and second antiferromagnetic Brillouin zone reconstructions. However, the underdoped samples in this study are not antiferromagnets, implying that there may be another explanation for the $\sqrt{2}\times\sqrt{2}$ boundary instead of antiferromagnetic zone reconstruction.

Second, the $1 - k_x$ line could indicate a "folding" of k-space over that line via which Umklapp[3] scattering may occur. However, this point of view seems to imply that peaks should be enhanced or increased in number due to the scattering mechanism, instead of disappearing when the quasiparticle dispersion crosses over the line.

6.10 Luttinger/Dzyaloshinskii Area Calculations

In a Fermi liquid, in general, one should be able to count all quasiparticles inside the (canonically closed) Fermi Surface, and the total particle occupation should be a measure of the carrier concentration of the noninteracting Fermi Sea. It is not obvious that this phenomenology extends to interacting electrons; however, in 1960, Luttinger presented his theorem which states that the volume enclosed by the Fermi Surface is in fact preserved in the case of electron-electron interactions. However, in the case of the cuprates, it is not clear whether the theorem would still apply for many reasons, but the most obvious of which is that the Fermi surface is not closed in any conspicuous way. Nevertheless, Oshikawa in 2000 extended Luttinger's theorem non-perturbatively to systems with dimension greater than

1.[18] In addition, Dzyaloshinskii proposes a "line of zeros" as an analogy to the better known singularity "holes" which produce a summation of energy singularities and thus the density of states and Fermi surface. If this "line of zeros" could correspond to the $\sqrt{2} \times \sqrt{2}$ area boundary found in these studies, it could form the basis of a different kind of truncated counting scheme: The area between the Fermi arc and this line of zeros could be the critical area to study, an idea which is motivated also by the fact that states near the $\left(\frac{\pi}{a_0}, \frac{\pi}{a_0}\right)$ appear to be missing.

If this is the case, then the area between the $1-k_x$ line of the $\sqrt{2}\times\sqrt{2}$ boundary and the Fermi arc may be of significance. If I parameterize the function $f_1(k_x)$ to represent the $\sqrt{2} \times \sqrt{2}$ boundary and $f_2(k_x)$ to be the calculated Fermi arc, then the area can be calculated via

$$Area = \int_{k_{xA}}^{k_{xB}} \Big[f_1(k_x) - f_2(k_x) \Big] dk_x \tag{6.23}$$

where k_{xA} and k_{xB} are the two points of intersection of the f_1 and f_2 curves. Further, the parameterization of the $\sqrt{2} \times \sqrt{2}$ box is always

$$f_1(k_x) = 1 - k_x \tag{6.24}$$

The function $f_2(k_x)$ may be parameterized in a number of ways. I used two different methods to do this. The first method fits a quarter-circle to the Fermi arc. The center of the circle is allowed to roam until a best fit is found, but it is constrained to the line $k_y = k_x$. The radius of the circle also varies until a best fit is found. Thus, in this case,

$$f_2(k_x; k_{x0}, k_{y0}, R) = k_{y0} - \sqrt{R^2 - (k_x - k_{x0})^2} \tag{6.25}$$

where $k_{x0} = k_{y0}$ is the center of the quarter-circle, and R is its radius. With these choices, the fits for the areas are shown in Figure 6.25. As expected, the area increases with increased doping.

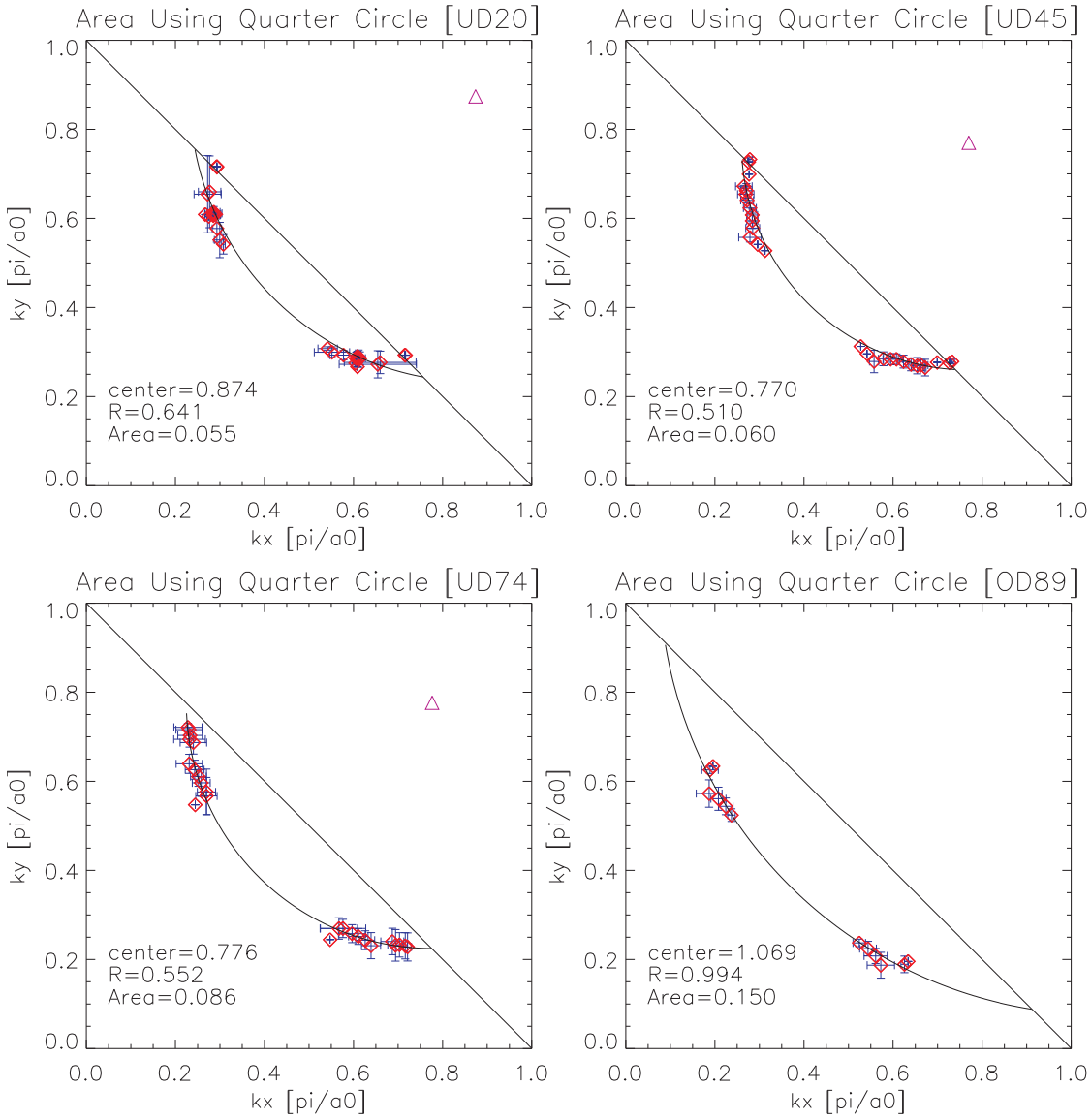

Figure 6.25: Calculated Area Between 1-$\vec{k}_x$ line and Fermi Surface Fit. $\vec{k}-space$ points are fit to a quarter-circle as in Figure 6.14. The radius (R) and the center of the quarter-circle are indicated on each plot.

A second, perhaps more physically-motivated parameterization for the Fermi arcs is to use a Norman band structure calculation.[16] Parameters for this calculation were fit by a colleague.[1] The only difference between band structure functionals between samples is a variation in the chemical potential, or μ, which is a best fit to the data. With this parameterization used for f_2, I calculate the

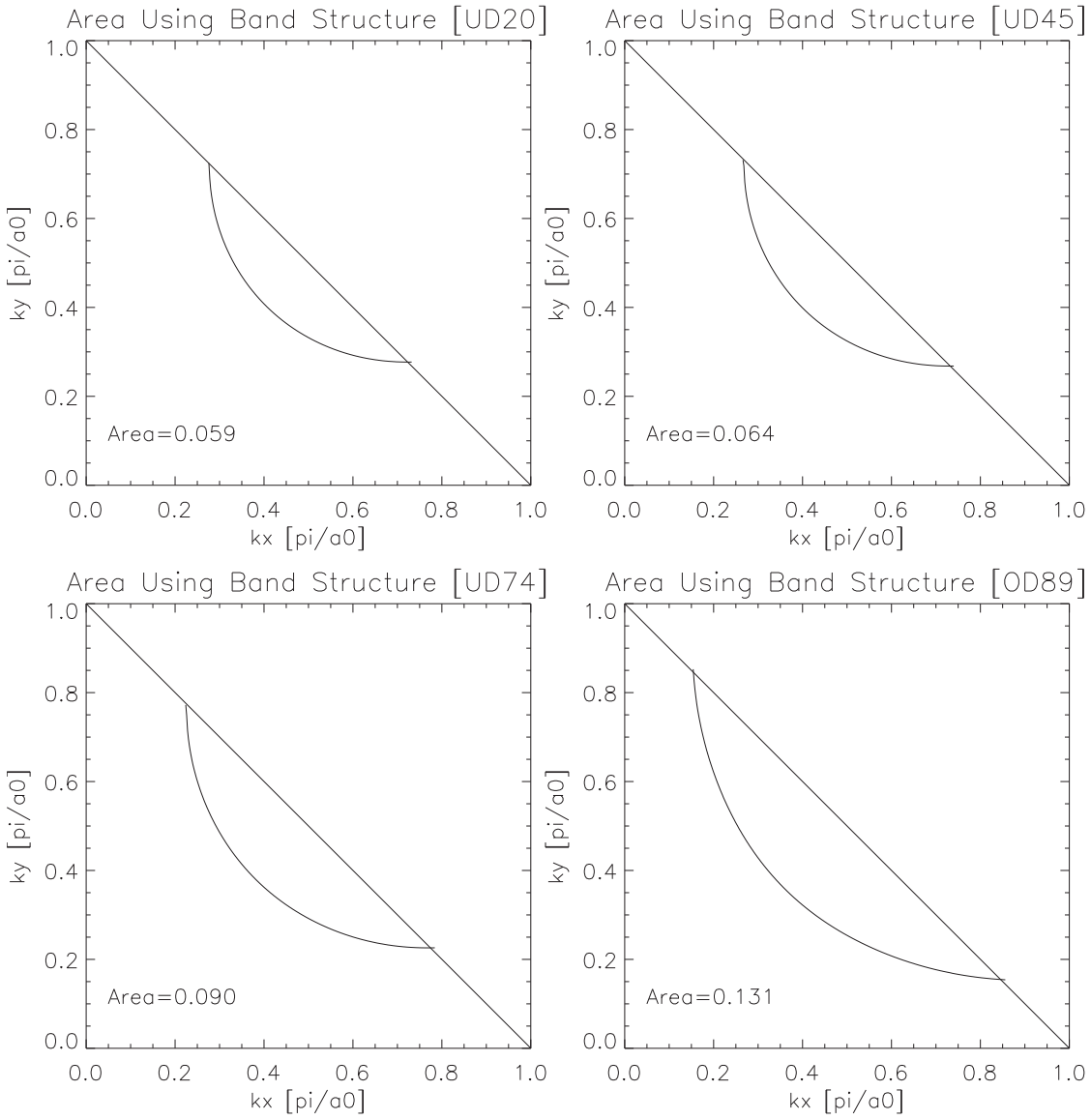

Figure 6.26: Calculated Area Between 1-$\vec{k}_x$ line and Parameterized Norman Band Structure. The band structure is assumed to be of the Norman[16] formulation with only the chemical potential (μ) and doping (p) varying between samples. The fit parameters, including the coefficients of the formulation and the chemical potentials, come from a colleague.[1]

areas shown in Figure 6.26. Again, the area increases with doping level.

In Table 6.2, the areas for these two parameterizations of the Fermi arc are given opposite the doping levels for each sample. The two different parameteri-

Table 6.2: Calculated Areas Between $1-\vec{k}_x$ and the Fermi Arc for Several Dopings. p and p^P are doping values as specified in Table 6.1. Areas found via both the quarter-circle method (Area^C) and the band structure method (Area^B) are given.

Calculated Areas Between $1-\vec{k}_x$ and the Fermi Surface						
Sample	p	p^P	Area^C	2×Area^C	Area^B	2×Area^B
UD20	0.06	0.0627	0.055	0.110	0.059	0.118
UD45	0.08	0.0814	0.060	0.120	0.064	0.128
UD74	0.14	0.111	0.086	0.172	0.090	0.180
OD89	0.19	0.180	0.150	0.300	0.131	0.262

zations give very similar results, which is a good consistency check. According to Luttinger's theorem, each area is multiplied by 2 for spin to arrive at the doping level. As one can see, there is some correlation between the area and the doping fraction, although admittedly the relationship is not extremely obvious. Further investigations will explore these area and doping relationships in greater detail.

6.11 Conclusions On This Chapter

It is clear that quasiparticle interference reveals different dispersive characteristics for different doping levels in the high-T_C cuprate superconductors. These behavioral changes in electronic quasiparticle dispersion are both self-consistent and quantifiable, and they extend broadly from (at least somewhat) overdoped to extremely underdoped levels. Through use of the octet model and known evidence from ARPES, the dispersion reveals the Fermi arcs, or bananas, which grow outwardly in size with increased doping. In addition, it is possible to fit a d-wave order parameter formulation with fundamental and first allowed harmonic to a scattering angle plot, and this constitutes at least a qualitative measure of the gap magnitude. In addition, the slopes of these plots reveal the evolution of the order parameter as well from overdoped to very underdoped. The Fermi arcs are

conspicuously extinguished near the $\sqrt{2}\times\sqrt{2}$ zone boundary, and area calculations reveal a gradual evolution with doping. All these demonstrations constitute a new, more rigorous, and more quantifiable method of probing the electronic structure of these correlated electronic systems.

As the Fermi arcs are extinguished, the quasiparticle spectral weight shifts to only two non-dispersive peaks, q_1^* and q_5^*, which then form a domain glass at higher energies which is well-defined in real-space (see Chapter 5). This implies a significant change from states well-defined in $\vec{k}$-space (Bogoliubov quasiparticles) to states well-defined in real-space (local electronic order). These different sets of states are separated in energy around 30mV, which thus constitutes an energy scale of some significance.

QPI theory rests on the ability of quasiparticles to scatter elastically between all possible electronic configurations. Because QPI analysis techniques work for underdoped samples, and because independent numerical scattering analyses[2] reveal decreased scattering as doping is increased from the pseudogap to the optimally doped regimes, it is reasonable to consider a gradual quasiparticle transition in this broad doping range. In light of prior studies on the pseudogap regime as previously discussed in Chapter 3, there are a variety of probes which also give a delineation in the transition into the pseudogap regime, including magnetic susceptibility, heat capacity, and in-plane transport. However, it is the spectrum of excited states itself which may be the key identifier of pseudogap physics. To name a few precedents, optical conductivity,[11] as well as STM itself, have given rich results which heuristically quantify the pseudogap phase transition.

In addition, when studying underdoped samples, ARPES studies[21] report an energy gap at the antinodal region of $\vec{k}$-space (directed toward $(\pm\frac{\pi}{a_0},0)$ or $(0,\pm\frac{\pi}{a_0})$) which remains intact through the phase transition to the superconducting state.

In contrast, the nodal region (directed toward $(\pm\frac{\pi}{a_0}, \pm\frac{\pi}{a_0})$)) exhibits the banana-shaped Fermi arcs previously described in this dissertation. Here, an anisotropic d-wave gap exists below T_C, and opens upon traversal of the temperature phase transition. The surprising fact is that this nodal gap seems to be smoothly connected to the omnipresent antinodal gap at their common point in $\vec{k}$-space, an effect which has now been reinforced by this research.

As demonstrated in this chapter, there is clear energy separation in the electronic structure between these two states, and additionally, two regions in $\vec{k}$-space which seem closely associated. As doping is decreased (approaching the Mott insulator), the distinction between these two states becomes more pronounced[12] because the separation between the quasiparticle excitation energies, and correspondingly their $\vec{k}$-space spectral weight, increases (see Figure 6.23). As indicated in the figure, as this energy separation (gap) approaches 100meV, T_C simultaneously approaches zero. Although this fact has thus far been unexplained (not withholding explanations based upon superfluid density decay), this behavior can be explained as a consequence of the superconductivity simply giving way to the antiferromagnetic state as the system becomes more susceptible to Mott physics with decreased hole doping.

One well-known early proposal by Anderson, namely a resonating valence-bond theory, may provide insight into why this gradual usurping of the Mott insulator state occurs as doping increases. In this representation, it is proposed that repulsive electron-electron interactions in a single non-degenerate band, such as one given by the Hubbard model, could be the origin of high-T_C superconductivity. Coulomb interactions (energy scale U) prevent double occupancy of a Cu orbital while the superexchange mechanism (energy scale J) produces antiferromagnetic quantum mechanical exchange interactions. When the Mott insulator is then doped, in-

creasing p, electron pairs of singlets, still with this binding exchange energy J, persist, but the "effective" J diminishes gradually to zero. There were, however, obstacles to the acceptance of this picture. First, it was not clear how such a simple model could represent the dramatic anisotropy observed in the electronic structure in $\vec{k}$-space. Second, nanoscale effects in real-space such as lattice coupling, phase separation, and self-organization remained unaddressed. All of these phenomena are important as doping tends towards zero. However, new computational models and techniques involving the Hubbard or more sophisticated models may provide numerical solutions to these issues. They show definite energy segregation in $\vec{k}$-space, a line of zeros in $\vec{k}$-space, and a counting of delocalized states, all of which have been discussed in Section 6.10.

From the evidence presented in this dissertation, then, it seems apparent that in the underdoped/pseudogap region of the phase diagram, there exist simultaneous states defined either well in $\vec{k}$- or well in and $\vec{r}$ space, but not both. These states are energetically separated at an energy for each doping level which corresponds to the location in $\vec{k}$-space in which the quasiparticle dispersion ceases, the $\sqrt{2} \times \sqrt{2}$ zone boundary. In addition, the maximum contrast in $\vec{r}$-space occurs at the pseudogap energy scale.[13] These facts hint strongly that, as energy increases, states change from coherently well-defined in $\vec{k}$-space to well-defined in $\vec{r}$-space. If so, the real-space images of domain patterns consisting of Cu-O-Cu bonds which emerge after the Bogoliubov particles have been usurped may be a direct measure of the pseudogap excitations, a finding which would be consistent with various prior theoretical proposals. In essence, the QPI and pseudogap energy scales, which appear to be one in the same for slightly overdoped samples, diverge and split into independent phases with decreased hole density, coexisting quantum mechanically despite being energetically separated.

BIBLIOGRAPHY

[1] J. W. Alldredge. private communication.

[2] J. W. Alldredge, J. Lee, K. McElroy, M. Wang, K. Fujita, Y. Kohsaka, C. Taylor, H. Eisaki, S. Uchida, P. J. Hirschfeld, and J. C. Davis. Evolution of the electronic excitation spectrum with strongly diminishing hole-density in superconducting $Bi_2Sr_2CaCu_2O_{8+\delta}$. *to be published*, 2008.

[3] N. W. Ashcroft and N. D. Mermin. *Solid State Physics*. Thomson Learning, Inc., 1976.

[4] K. H. Bennemann and J. B. Ketterson. *Physics of Superconductors*, volume II. Springer, Berlin, 2004.

[5] U. Chatterjee, M. Shi, A. Kaminski, A. Kanigel, H. M. Fretwell, K. Terashima, T. Takahashi, S. Rosenkranz, Z. Z. Li, H. Raffy, A. Santander-Syro, K. Kadowaki, M. R. Norman, M. Randeria, and J. C. Campuzano. Nondispersive fermi arcs and the absence of charge ordering in the pseudogap phase of $Bi_2Sr_2CaCu_2O_{8+\delta}$. *Physical Review Letters*, 96(10):107006, 2006.

[6] U. Chatterjee, M. Shi, A. Kaminski, A. Kanigel, H. M. Fretwell, K. Terashima, T. Takahashi, S. Rosenkranz, Z. Z. Li, H. Raffy, A. Santander-Syro, K. Kadowaki, M. Randeria, M. R. Norman, and J. C. Campuzano. Anomalous dispersion in the autocorrelation of angle-resolved photoemission spectra of high-temperature $Bi_2Sr_2CaCu_2O_{8+\delta}$ superconductors. *Physical Review B (Condensed Matter and Materials Physics)*, 76(1):012504, 2007.

[7] K. Fujita. Bogoliubov angle and visualization of particle-hole mixture in superconductors. *to be published*.

[8] D. J. Griffiths. *Introduction to Quantum Mechanics, 1st. ed.* Prentice Hall, Inc., Upper Saddle River, NJ 07458, 1995.

[9] T. Hanaguri. Effect of d-wave coherence factors on the quasi-particle interference in $Ca_{2-x}Na_xCuO_2Cl_2$ under magnetic fields. *to be published*.

[10] T. Hanaguri, C. Lupien, Y. Kohsaka, D.-H. Lee, M. Azuma, M. Takano, H. Takagi, and J. C. Davis. A 'checkerboard' electronic crystal state in lightly hole-doped $Ca_{2-x}Na_xCuO_2Cl_2$. *Nature*, 430:1001–1005, 2004.

[11] C. C. Homes, T. Timusk, R. Liang, D. A. Bonn, and W. N. Hardy. Optical

conductivity of c axis oriented $YBa_2Cu_3O_{6.70}$: Evidence for a pseudogap. *Phys. Rev. Lett.*, 71(10):1645–1648, Sep 1993.

[12] S. Huefner, M. A. Hossain, A. Damascelli, and G. A. Sawatzky. Two gaps make a high temperature superconductor, 2007.

[13] Y. Kohsaka, C. Taylor, P. Wahl, A. Schmidt, J. Lee, K. Fujita, J. Alldredge, J. Lee, K. McElroy, H. Eisaki, S. Uchida, D. H. Lee, and J. C. Davis. Quasiparticle extinction and progressive energy-segregation of momentum-space from real-space states in $Bi_2Sr_2CaCu_2O_{8+\delta}$. *to be published*, 2008.

[14] K. McElroy, D. H. Lee, J. E. Hoffman, K. M. Lang, E. W. Hudson, H. Eisaki, S. Uchida, J. Lee, and J. C. Davis. Homogenous nodal superconductivity coexisting with inhomogeneous charge order in strongly underdoped bi-2212, 2004.

[15] K. McElroy, R. Simmonds, J. Hoffman, D. Lee, J. Orenstein, H. Eisaki, S. Uchida, and J. Davis. Relating atomic-scale electronic phenomena to wave-like quasiparticle states in superconducting $Bi_2Sr_2CaCu_2O_{8+\delta}$. *Nature*, 422:592–596, 2003.

[16] M. R. Norman, A. Kanigel, M. Randeria, U. Chatterjee, and J. C. Campuzano. Modeling the fermi arc in underdoped cuprates. *Physical Review B (Condensed Matter and Materials Physics)*, 76(17):174501, 2007.

[17] T. S. Nunner, B. M. Andersen, A. Melikyan, and P. J. Hirschfeld. Dopant-modulated pair interaction in cuprate superconductors. *Physical Review Letters*, 95(17):177003, 2005.

[18] M. Oshikawa. Topological approach to luttinger's theorem and the fermi surface of a kondo lattice. *Phys. Rev. Lett.*, 84(15):3370–3373, Apr 2000.

[19] M. R. Presland, J. L. Tallon, R. G. Buckley, R. S. Liu, and N. E. Flower. General trends in oxygen stoichiometry effects on tc in bi and tl superconductors. *Physica C*, 176:95–105, 1991.

[20] M. Sutherland, D. G. Hawthorn, R. W. Hill, F. Ronning, S. Wakimoto, H. Zhang, C. Proust, E. Boaknin, C. Lupien, L. Taillefer, R. Liang, D. A. Bonn, W. N. Hardy, R. Gagnon, N. E. Hussey, T. Kimura, M. Nohara, and H. Takagi. Thermal conductivity across the phase diagram of cuprates: Low-energy quasiparticles and doping dependence of the superconducting gap. *Phys. Rev. B*, 67(17):174520, May 2003.

[21] K. Tanaka, W. S. Lee, D. H. Lu, A. Fujimori, T. Fujii, Risdiana, I. Terasaki, D. J. Scalapino, T. P. Devereaux, Z. Hussain, and Z.-X. Shen. Distinct fermi-momentum-dependent energy gaps in deeply underdoped bi2212. *Science*, 314(5807):1910–1913, 2006.

[22] M. Tinkham. *Introduction to Superconductivity, 2nd. ed.* Dover Publications, Inc., 31 East 2nd Street, Mineola, NY 11501, 2004.

[23] Q.-H. Wang and D.-H. Lee. Quasiparticle scattering interference in high-temperature superconductors. *Phys. Rev. B*, 67(2):020511, Jan 2003.

[24] H. W. Willemsen and K. E. Gray. Distribution function in nonequilibrium states of a superconductor. *Phys. Rev. Lett.*, 41(12):812–815, Sep 1978.

Chapter 7
Summary

In summary, investigation of tunneling asymmetry of the lightly-hole doped cuprate superconductors revealed a disordered glass of electronic domains. This structure consists of scattered, unidirectional objects that break translational and rotational symmetries. The internal structure of the domains consists of many Cu-O-Cu bonds stacked inside (up to $\sim 25a_0$) long lines, perpendicular to the Cu-O-Cu bonds, of bonded Cu sites. These features are ubiquitous in both NaCCOC and BSCCO, two underdoped cuprates sharing no common chemical properties except for the presence of at least one CuO_2 plane, at several doping levels.

Meanwhile, quasiparticle interference studies demonstrate dramatic and quantifiable dispersion at low (∼6-30mV) energies. Utilizing the octet model, one may map the $\vec{q}_i$ scattering vectors to the high spectral weight points which exist on the Fermi arcs in $\vec{k}$-space. The energies of each of these along the so-called $\vec{k}$-space "banana" points may be plotted versus the ARPES hole-pocket angle, revealing a gradually varying slope with doping evolution. Further, through a d-wave representation of azimuthal angle, it suggests a measure of the order parameter of the higher energy states. Because these states are well-defined not in $\vec{k}$-space but in $\vec{r}$-space, as evident from the studies performed via tunneling asymmetry, it is reasonable to conclude that there is energetic separation between well-defined eigenstates in $\vec{k}$-space and $\vec{r}$-space. Because the spectral gaps grow continuously from the optimally doped superconductor into the pseudogap regime, and because the higher-energy gap is associated with the domain glass, it is reasonable to consider the disordered patterns of the nanodomains to be visualizations of the pseudogap quasiparticle excitations.

Figure 7.1 and Figure 7.2 show these ideas schematically. In the first figure,

the spectrum at top shows two energy scales which are segregated in $\vec{k}$-space, one associated with Bogoliubov quasiparticle states (along the nodal direction), and one associated with the pseudogap excitations (along the antinodal direction). In the latter figure, the middle panel shows the energetic dispersion of the quasiparticle states with a d-wave fit at low energies, which is represented by the lower image of QPI. At the $\sqrt{2} \times \sqrt{2}$ interface, the states suffer an energetic transformation to physics in which the pseudogap, and additional scattering, dominate. This behavior is embodied by the real-space image of disordered electronic domains.

Figure 7.1: Relationship Between Energetic Shifts in Spectral Weight and States Located on Fermi Arcs. (**Top**) Schematic of the spectral density in underdoped cuprates. (**Bottom**) Representation of one quadrant of $\vec{k}$-space showing a Fermi arc. The spectrum and the Fermi arc are connected suggestively via arrows. Orange represents Bogoliubov quasiparticle states well-defined in $\vec{k}$-space, and violet represents electronic pseudogap excitations well-defined in $\vec{r}$-space. Gaps at lower energies correspond to the Bogoliubov states, and gaps at higher energies correspond to the electronic excitations of the pseudogap.

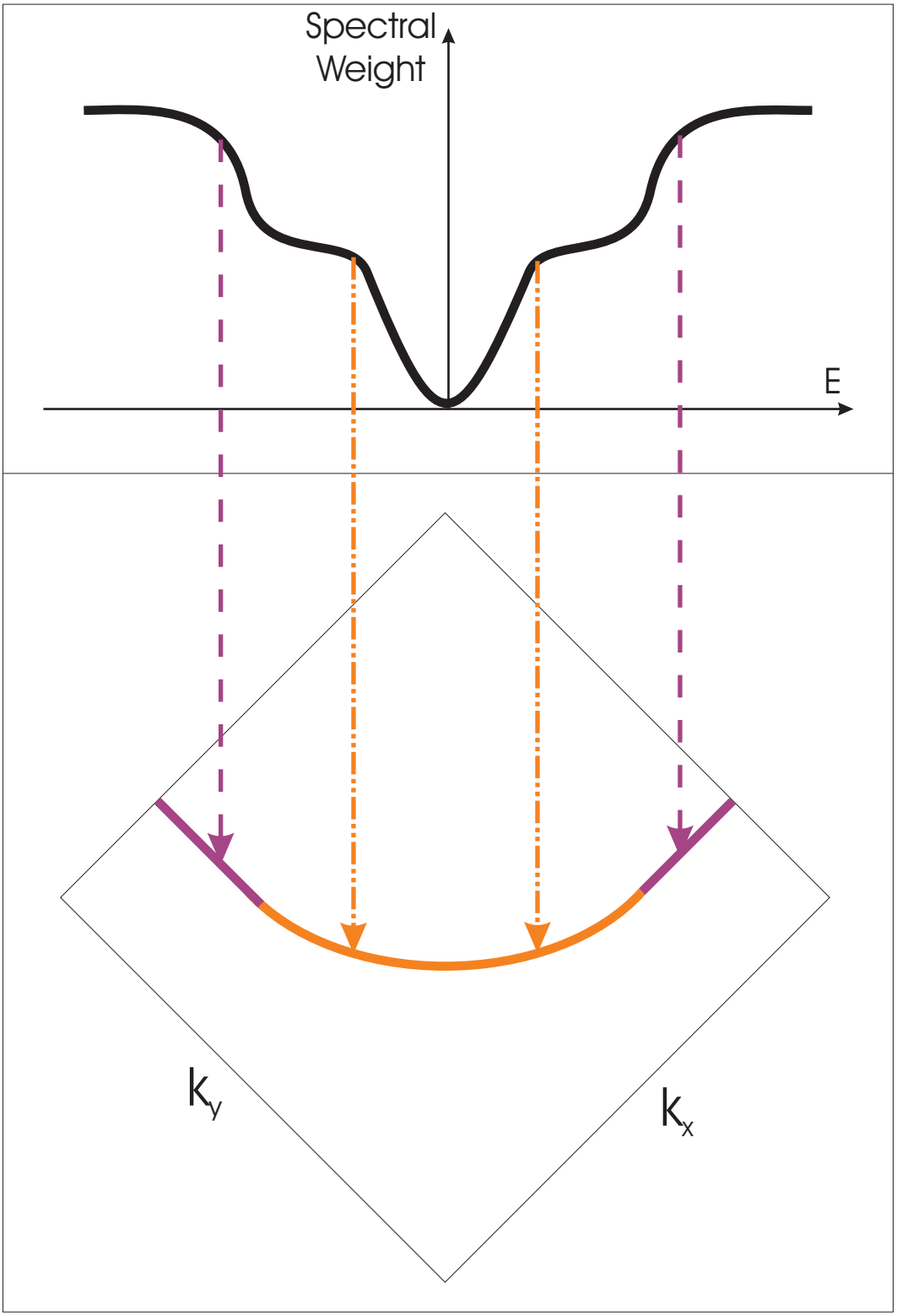
Spectral
Weight
E
k_y
k_x

Figure 7.2: Separation of States in $\vec{k}$-space and $\vec{r}$-space. The center panel shows a rendered cartoon of the low-energy Bogoliubov quasiparticle states smoothly connected to the higher-energy states of pseudogap-like excitations. An orange arrow indicates the correspondence of the octet scattering in $\vec{q}$-space with the coherent, d-wave state, and a violet arrow indicates the $\vec{r}$-space disordered electronic domain patterns, which correspond to the pseudogap excitations.

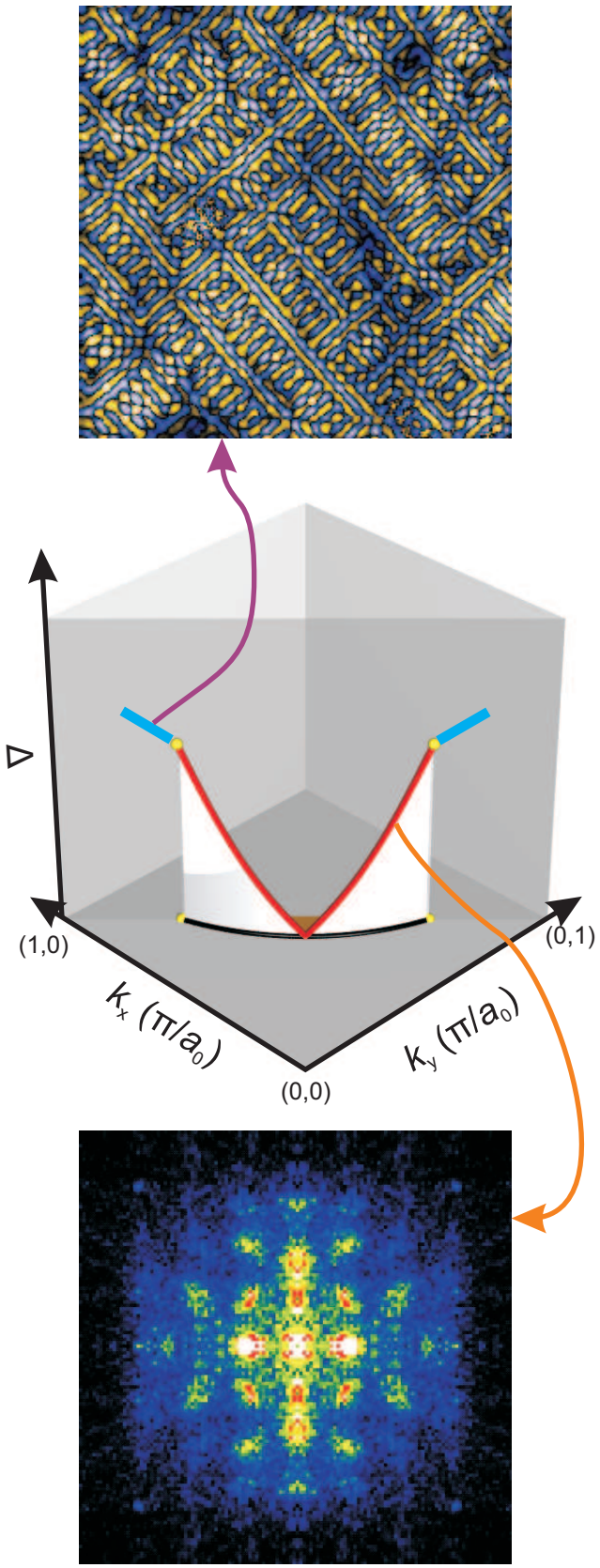
Δ
(1,0)
k_x (π/a_0)
(0,0)
k_y (π/a_0)
(0,1)

APPENDIX A

Discrete Fourier Transforms (DFT)

Discrete Fourier transforms in this dissertation are computed as follows

$$\tilde{f}(\vec{k}) = \frac{1}{MN} \sum_{x=0}^{M-1} \sum_{y=0}^{N-1} f(\vec{r}) e^{\frac{-j2\pi(k_x x)}{M}} e^{\frac{-j2\pi(k_y y)}{N}} \tag{A.1}$$

with $\vec{r} = x\hat{x} + y\hat{y}$ and $\vec{k} = k_x\hat{x} + k_y\hat{y}$. The output of the DFT is further masked with a quadratic window. Before the DFT is performed, the average value over the 2D images, or the 0^{th} order polynomial, is subtracted. This prevents both strong dwarfing of signals due to a large peak at $\vec{k} = 0$ as well as Fourier aliasing from the same point in k-space.

If $N = M$, then A.1 simplifies to

$$\tilde{f}(\vec{k}) = \frac{1}{N^2} \sum_{x=0}^{N-1} \sum_{y=0}^{N-1} f(\vec{r}) e^{\frac{-j2\pi(\vec{k}\cdot\vec{r})}{N}} \tag{A.2}$$

$N = M$ in all cases for the data sets in this dissertation, although there is no general restriction against $N \neq M$.

APPENDIX B

STM Head Assembly Instructions

B.1 STM Body Assembly Instructions

B.1.1 Ingredients Needed

- Commercial PI piezo stacks
- Samtec brass pins
    - 9 for walker
    - 6 for scanner/position sensor
    - 3 for tip and ground
- Samtec Connectors (probably already attached to fridge)
- Lakeshore small white low-temperature coax for pos. bal. signal
- Microdot coax connector/plug for above
- Consolidated bare copper wire (35 mils/20 BC) for front plate
- McMaster-Carr PTFE insulating sleeve tubing for front plate
- Formvar copper wire for walker (12 mils)
- Formvar copper wire for scanner (8 mils)
- Bare copper wire (4 and/or 5 mils) for Tip/GND signals
- Ruby ball (0.118 diameter)
- Machined Parts (according to drawings):
    - Macor STM body

- Macor top plate
- Titanium front STM body piece
- BeCu sample plate (probably already affixed to the fridge)
- Macor spacer piece
- Entire scanner assembly
  - Macor Scanner Holder Tube/Base (long)
  - Long Piezo Tube
  - Macor Small Tip Holder inside (and on top of) piezo tube
  - Ceramic Tube for tip holder
  - BeCu Tip Holder Tube (breaks easily)
  - Tips: Tungsten Tips from DI or PtIr Tips cut from wire
- Sapphire prism = Corundum beam
- Macor inserts for sapphire prism
- BeCu Spring plate
- Brass inner and outer position sensor plates
- Macor "walker stopper" plate on bottom
- Macor bottom stage/base

- Brass screws:
  - (4x) 3-48, 1/2 for BeCu press plate
  - (5x) 4-40, 1/2 for top plate
  - (3x) 0-80, 3/16 for affixing scanner assembly to corundum beam
  - (3x) 0-80, 3/16 to affix outer capacitance sensor electrode to base

- (4x) 4-40, 3/4 to connect macor body and macor base
- (4x) 8-32, 3/4 to hold STM base to cryostat

B.1.2 Tools Needed

- Piezo Jigs to set piezos in position
- Wiring Jig to hold wires as glue sets
- Pb/Sn solder (no flux)
- Nokorode flux for pins
- TorrSeal for piezos, wiring, and samtec pins
- Epotek H20E for gluing to piezo pins
- StripX for removing formvar
- Tweezers (all kinds: flat, pointy, etc.)
- Tweezer-sized scissors
- Gloves (clean, no powder)
- Tongue Depressors
- Kimwipes
- Toothpicks
- Wooden Mixing Rods
- Wooden Rods with Cotton Swabs on the end
- Glass Slides
- Acetone, IPA = Isopropyl Alcohol, Methanol
- Small scale (in tenths of an inch)

- Microscope
- Shrink Wrap for coax

B.1.3 Pre-Assembly Checklist

- Wear gloves through ALL these procedures.
- Gather ingredients: Parts listed in associated document STM2 v2 Head Ingredients
- Refer to Figure B.1 for the piezo wiring diagram. This is but one choice for wiring the STM head, but it worked well for us.

B.1.4 Check Assembly Alignment

- Put on gloves and have tweezers ready.
- Using screws which are intended for the macor top plate, affix jigs to the macor body, being sure not to use the top jigs on the bottom (and vice-versa). It will look incorrect if you do anyway, and it will be an obvious mistake.
- Place 4 piezos in proper orientation in the body (shiny side up), snuggling up nicely against the jigs.
- Place prism on top of piezos in the exact orientation you want it to be. (Do NOT consider it a rotatable object despite its symmetry. Find a way to mark its orientation if you havent already done so.) Once the prism is snug, use tweezers to push the piezos snugly against the jigs again. (They will have moved.)

- Place two piezos on top of the prism in the correct orientation (shiny side down). Place titanium front plate on top of these piezos carefully. (They will move no matter what you do.)
- Place ruby ball on top of front piece, and place spring plate on top of ruby ball. Grab 4 front plate screws and screw down the spring plate loosely. Use tweezers to adjust the location of the 2 front piezos and the rotation angle of the titanium piece. When amply satisfied (it wont be perfect), tighten screws. Tighten two left screws all the way and keep two right screws fairly loose for now. The inner guts of the STM should be immobile.
- Remove the jigs. Pick up the head and look at it from all angles. Note anything which has set wrong there can be a lot of things which are not quite right. In particular, each vertical piezo pair might not be collinear, and the piezos might not be located in the center of the prism face. (The latter is a problem because this causes a force imbalance and will wear the system more rapidly if not corrected.) There should be no gaps between the shiny piezo faces and the prism. (However, this can possibly be corrected when you actually glue it.) If there are gaps, deassemble the head and try assembly again.
- Screw the macor spacer piece and the macor top plate piece on. The circle in the spacer piece will act as a guide to the eye for helping to you determine whether or not the center axis of the prism lies in the exact same place as the center line of the STM head. If it doesnt, you may need to make a few adjustments to the head (like re-machine it or something).
- Once you have determined that everything looks aligned properly, disassemble the head. Assemble the head at least twice (for practice and also to verify your findings) without glue. When you are satisfied, continue.

B.1.5 Glue Samtec Pins to the Macor Body

- Two choices: You can put all 9 pins in 9 holes, grab a Samtec connector, attach the connector, push the pins as far as they will go into the connector, and then glue them down. Or you can do it by eye without the connector. I elected to do the latter because the alignment is not all that critical and I knew I could line them up well with my eye. This also allowed me to adjust the positions of the pins on the fly while the glue was drying. Your choice.
- Mix a batch of TorrSeal (use one line of glue and one line of hardener) with a tongue depressor. Turn the macor body upside down. Youll want to glue the pins closest to the center of the body first. Put the first pin in the first hole and put it about where you want it. Then pull it inward a bit. Grab several toothpicks and use one to get a small dab of glue. Glue the pin and macor body where the pin is just emerging from the macor body on the inside of the body (sort of like doing a solder joint). Then, push the pin back in to the right position. Add more glue to the bottom of the pin and macor body. (This will feel a bit like acrylic painting.)
- Do all 9 pins the same way. Once a couple have been glued, its easy to see where the others will go just by making them all coplanar. Glue the 6 scanner pins the same way, on the left side of the head. (The middle row is missing in that set.) Finally, glue the STM and ground pins on the top of the head in the same way. Let the head sit for 24 hours.

B.1.6 Prepare Piezos and Glue Wires to Piezos

- Using tweezer-sized scissors, cut off about half of the length of the leads protruding from each piezo until about 80 mils length remain. (This is to

save space for gluing wires.) There are 4 leads, and the two immediately above and below each other form a pair (electric contact). Use flat tweezers to pinch each pair of leads together, but leave enough slack in the lead so that the piezo can shear without interference. When you are happy with your pinching job, prepare a batch of H20E epoxy (1:1 ratio by mass) on a glass slide. For each pair, dab the surface of each lead with a tiny amount of glue, and pinch them together. They should stay pinched. Bake according to the Epotek H20E recipe. (I used the most conservative/longest baking time recipe, which is 90 minutes at 80?C.) Repeat for all piezos.

- In accordance with the wiring diagram (see Figure B.1), prepare wires using the wiring jig. You may protrude wires from the pads at the most convenient orthogonal angle possible (left, right, straight). The jig can handle all these directions. Use 12mil formvar copper wire. Make sure wires are much longer than needed at this stage. Prepare a wire by carefully applying StripX to the end of a long wire and letting it eat away the formvar for about 1 minute. Then wipe off the StripX with a Kimwipe. StripX is supposedly cancerous, so be careful not to inhale or touch it!

- Prepare a batch of H20E epoxy (1:1 ratio by mass) on a glass slide, and apply glue to pads after wires have been set in the jig. Make sure NONE of the glue splotches will set at an elevation higher than that of the shiny surfaces for each piezo! (This would cause the prism to touch the pad instead of the piezo foot.) Bake according to the Epotek H20E recipe. (I used the most conservative/longest baking time recipe, which is 90 minutes at 80?C.) Repeat for all piezos.

B.1.7 Assemble Walker with Glue

- Just as before when testing the head alignment, now well glue the piezos down. You do basically the same thing as before, only this time, apply the glue.
- Attach the jigs to the macor body again, and practice assembling the walker once or twice with the wires attached to the piezos. (Its more difficult, and the jigs get in the way.) When ready, glue:
- You will need 2 people to do this. One prepares batches of TorrSeal while the other assembles the STM. (TorrSeal gets relatively thick in about 20 mins, and you should have the glue mixer mix new glue every 5-10 minutes. The assembly took me about 30 minutes to complete.) Mix TorrSeal according to the instructions on the box: a line of glue and a line of hardener. Mix with a tongue depressor on a glass slide.
- You need to glue BOTH the underside of the piezo and the macor body itself at the position where the piezo will go. Apply a thin, but evenly distributed, amount of TorrSeal to the dull face of the piezo. Apply a thin, but uniform, amount of TorrSeal on the place where the piezo will rest snugly against its jig. When satisfied, press the two pieces together, pushing firmly down and against the jig with your finger. DO NOT get any glue on the shiny face of any piezo or the polished face of the sapphire beam. If you notice that you have done this at any point in the procedure, stop what you are doing immediately, grab a cotton+stick swab, douse it with IPA and wipe the affected areas until they are clean.
- Continue assembly until the 4 piezos are glued to the macor body. Check again for glue in dangerous areas. Place the prism in the proper orientation in the head. This might move the glued piezos. Even if it doesnt, grab

tweezers and once again push the piezos up against the jigs until they are snug and firm.

- Take the titanium front piece and flip it over to the flat side. You want to affix the two piezos for this piece each 0.100 from the ends. Grab a small scale so you can measure this distance. Apply glue to the dull sides of the piezos and the flat side of the titanium piece in the same manner as before and press down. Make sure the piezos are centered on the piece, are collinear, and are located 0.100 from the ends.
- Turn this piece over (the piezos will stick) and place it on top of the prism in the head. Make sure the wires are going roughly where you want them to go. Grab the ruby ball with tweezers and place it on the titanium piece. Grab the spring plate and place it on the ruby ball. Grab the press plate screws and put them all in loosely. Tighten the two right screws just enough so that the assembly will remain put. (Remember to tighten the left screws all the way and adjust the right screws loosely.)
- Look from the top of the head. Is the titanium piece straight up and down? Probably not: rotate it with your tweezers, making SURE that the front plate piezos dont change orientation relative to the front plate when you do. (If the front plate is too tight to rotate it, loosen the right spring plate screws a little bit so you can rotate.) When it looks good, tighten the screws down again. Look again from the top. Hopefully, all piezo stacks are collinear, located where they need to be vertically, and are in the center of each prism face, distributing the force evenly. If not, try to make adjustments if you can. Piezos are still mobile at this point.
- When everything looks good, tighten all spring plate screws all the way. Let the assembly sit on its side in air for 24 hours. (You can also bake it, but I

elected not to for a little bit more safety.)

B.1.8 Glue Patch Wires

- Some Wires cannot be glued until the piezos are set in place. These are patch wires, which are small wires connecting two piezos in short range, all for ground connections. There are 3 of these in the design.
- Open up the STM head by unscrewing the press plate and taking off the titanium piece.
- Cut the end of a wire (probably one end already glued to the piezo) to the appropriate, short length to get to the other piezo. Bend the wire up. CAREFULLY apply StripX to the end. (Dont touch anything else!) After 1 minute, remove StripX with a Kimwipe. Push the patch wire back down until it touches the piezo lead. (It may take some twisting.)
- Prepare H20E as before, and apply it to the piezo pad and wire, making sure not to let any glue harden above the elevation of every shiny piezo surface. Bake it at 80?C (modest temperature) for 90 minutes, according to the Epotek H20E instructions.

B.1.9 Tack Down Wires

- The trajectory for the wires is already set in the design specifications, but make sure you know where you want the wires to go in your mind. Then, one step at a time, prepare a batch of TorrSeal and glue down the wires in the proper trajectory. Make sure that there is plenty of space between the wires and the prism: its good to push the wires as close to the macor body as possible. Put TorrSeal down over, under, and around the wire where you

want it to stay. The first tack is strain relief for the wires glue joints to the piezo pads: make sure it is strong.

- Let each tack dry for a couple of hours before continuing to the next one.
- Eventually, all the wires in the body (5) will end up in a line near the walker connector. Make one last tack there.

B.1.10 Prepare Feedthrough Wires on Titanium Piece

- Cut a length of PTFE sleeving slightly longer than the width of the titanium piece. (Lets say about 20 mils on either side.) Cut a length of about 35 mil copper wire slightly longer than the PTFE tubing you cut. (The ends of the wire should stick out far enough to make a solder joint.) Make sure the wire will go in the tubing snugly. Prepare TorrSeal and apply along the length of the copper wire (not the ends). Slide the copper wire into the tubing, centered. Apply a good amount of TorrSeal to the bottom of the first groove in the titanium piece. Press the PTFE tube, centered, firmly down into the groove. (Be careful not to scratch the shiny sides of the piezos underneath!)
- Repeat the above process for the second groove.
- When the glue is reasonably dry (2 hours), grab the soldering iron set at about 500?F (and flux, if you want to use it). Cut the two piezo wires which require the feedthrough connections to an appropriate length. (Shorter is better, but dont stretch the wire too much.) StripX the ends of each wire, and solder them to the ends of the copper wire. (The PTFE could melt a bit, so dont heat the copper wire for too long.)
- Get a couple more long, 12 mil formvar wires. StripX one end of each. Solder them to the other end of the PTFE/copper wire feedthrough.

- Replace the titanium piece on the prism, and reattach the spring plate. You should now have 8 wires (5 from the macor body, 3 from the titanium front piece) coming down to the walker connector. Tack down the 3 from the front piece with TorrSeal.

B.1.11 Make Walker Wire Connections to Samtec Pins

- Make sure the pins and the area around it is all clean. (You can let the bottom part of the STM head wade in acetone, then in IPA, to clean it.)
- Apply NoKorode flux to each brass pin on the inside of the STM head. Cut the wires so that they are short enough to be manageable, but long enough to find each pin if need be. In accordance with the wiring diagram (see Figure B.1), bend each wire into a good trajectory to its intended pin, being careful not to disturb the trajectory of neighboring wires or straining the wire too much. Note the length of each wire needed to make it to its respective pin.
- In turn, lift up each wire and cut it at its intended length. StripX the end. Do the same for all wires. Grab some Pb/Sn (flux-free) solder and put some on the soldering iron set at about 500?F. Tin each brass pin, and tin the ends of the formvar wires. (Dont heat the formvar for a long time.)
- Bend each wire back to its intended position, getting it as close to the soldered pin as possible. In turn, touch the soldering iron to the pin/wire combination and let it melt. Check each connection by pulling on the wire fairly hard (for a 12 mil wire).
- When satisfied, wade Samtec pins in acetone and IPA again (in ultrasonicator) to clean up.
- Push the wires out of the way of the scanner assembly base, which will have

to come up and smack against your beautiful wiring job in order to halt. *cough* bad design *cough cough*

B.1.12 Add Scanner Assembly to the Head

- Once again, remove the spring plate, ruby ball, and bend up the titanium piece, which will hang in air using the wires you connected.
- Grab some 8 mil formvar copper wire and make 6 long wires, StripXing one end of each of them. Flux and tin each of the 6 brass Samtec pins as you did before with the walker pins. Tin each end of the copper wire. Solder the top 3 connector pins to 3 of your wires. Solder the other 3 wires to the corresponding pins on the scanner assembly corresponding to the bottom 3 connector pins. (One possible hazard here is that the outer conductor of capacitance sensor comes awfully close to the solder joints of the scanner assembly when the assembly is retracted fully. Keep this in mind when making your solder connections.)
- Insert the prism, and attach the titanium plate, ruby ball, and spring plate again. Insert the scanner assembly into the prism, attaching it to the prism with its intended screws. Bend and adjust all your wires to see what the best trajectory is. Remember that none of these wires should theoretically touch, and the scanner assembly moves several millimeters up and down in situ.
- When you have a good layout for the wires, cut them. Bend them up, StripX them, tin them, and bend them back down. Solder them to their appropriate pins on the scanner assembly and the connector. Finally, look at the layout of your wires and make sure none are touching or will touch. If you think they might, carefully pull and push the wires around with tweezers.

B.1.13 Attach Tip and Ground Wires

- Flux and tin the pins (posts) on the top of the STM head associated with the tip and ground wires. Grab some 4 mil bare copper wire and cut a length somewhat slack from each of the two pins to the STM tip assembly. (Remember it moves up and down several millimeters.) Under a microscope, solder one end of one of the wires to the tip post, and solder the other end to the BeCu tip holder. (This may take several tries.. but once stuck, it should stay firmly.)
- Prepare some H20E epoxy. Under the microscope, solder one end of the other wire to the ground post. Glue the other end to the ground shielding plane underneath the tip. Bake the entire head at 80?C degrees for 90 minutes. No, it wont ruin the scanner.

B.1.14 Assemble the Rest of the Head

- Using the 3 outer capacitance sensor screws, attach the outer conductor of the position sensor to the STM head base. Note where the position balance coax must go (in the groove on the underside of the STM base) and where it must be soldered to the collar of the outer conductor. Remove the outer conductor.
- Flux and tin the part of the outer conductor on the top part of its collar where it will connect to the coax. Prepare one end of a white LakeShore low-temperature coax with its corresponding coaxial connector/plug. (See the instructions on the manufacturers website.) Making sure youre leaving plenty of length to make it to the coax connector plate on the STM stage of the cryostat, cut the coax.

- Cut off about half an inch of the outer insulator, shielding, and inner insulator, leaving only the inner conductor exposed. Cut and slide a piece of shrink wrap over the coaxial cable. Solder this inner conductor of the coax to the outer conductor of the capacitance sensor. Find a heat gun and shrink the wrap over the exposed conducting parts.
- Alternatively to the above step, solder a hook made of some copper wire to the outer conductor before soldering the coax to the hook. This strengthens the part mechanically, and you may expose a shorter length of the inner conductor of the coax.
- Re-attach the outer conductor to the STM base using the 3 screws, but this time put the macor stopping plate on top of the outer conductor before screwing it down. DO NOT OVERIGHTEN the screws; the macor plate is very fragile!
- Push the new coax into its groove underneath the STM base. Make sure that there are no conducting pieces under the STM which could possibly touch experiment ground once the STM is attached to the fridge. Screw the macor body to the base using the 3 long screws.

B.1.15 Put the STM on the Fridge

- Making sure everything is clean, mount the head on the STM plate of the cryostat. Place the head and use the 4 screws to attach the head to the plate tightly. Slide the thermal block and connector, together as one piece, into each groove on each side of the STM. Youll have to screw and unscrew the block fastener a bit to get the block to go in all the way. Make sure the connectors are seated firmly. Grab the thermal connection screws and

washers and attach them firmly down onto the copper wire attached to each block.

- Attach the position sensor coax to the coax plate.
- Check capacitances and resistances for the walker and scanner.
- Put the spacer plate on between the STM head and the copper bias plate. Attach the top plate with 5 screws. Do walker test. If it passes, congrats.
- Remove the spacer and top plates and solder the tip and ground lines. (Harder than it looks be careful.)
- Replace the spacer plate and top plate. Try scanning on graphite.

B.2 Scanner Assembly Instructions

The following section was contributed by Andy Schmidt, a fellow graduate student and colleague.

B.2.1 Parts and Tools Needed

- Macor scanner holder made to match piezo tube length, usually 0.500.
- Macor tip holder
- Piezoelectric tube Purchased from EBL Products, Inc. Description: 0.125 OD x 0.020 Wall x 0.500 Length, Gold Electrodes, 4=90 Degree Quadrants on OD Vendor Quote #25-0294 Paul Stokes 860-290-3737
- Ceramic Tube This is sold by Omega Engineering, Inc. as Ceramic Thermocouple Insulators Pick the closest OD and ID to match. Usually OD 1/32, ID 0.020.

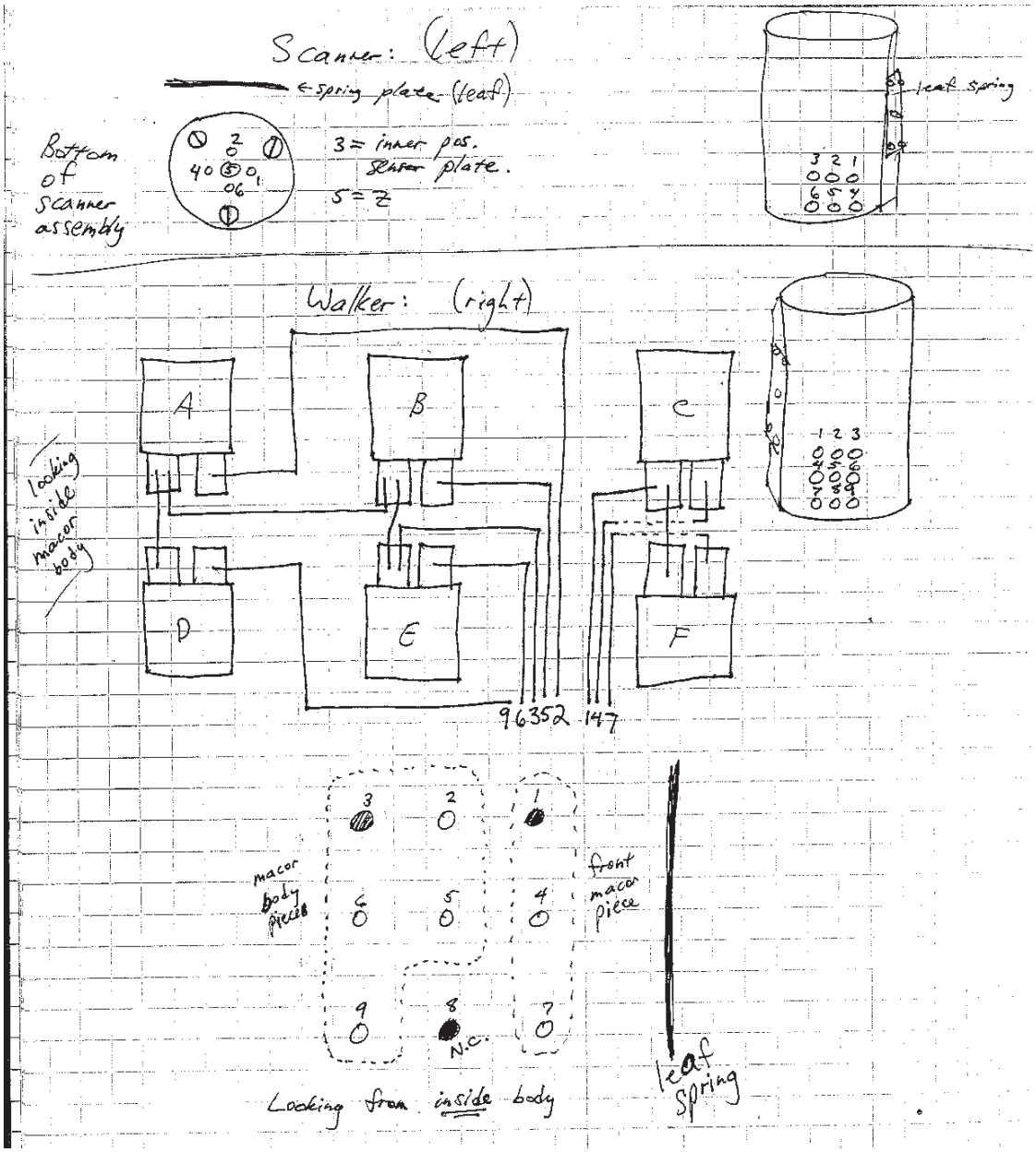

Figure B.1: STM Piezo Wiring Diagram. This is but one option, but it worked well for us.

- BeCu Tube ID is 0.0135, which is the diameter of bare copper wire that was a very snug fit inside tube. Hard to find; Davis group supply is from a sample Jenny Hoffman secured.
- #36 Bare Copper Wire for X-Y lines. Old STM2 scanner used larger wire
- #28 Bare Copper Wire for Z line
- Jhinhwan Lee Z line to piezo tube gluing jig
- Jhinhwan Lee piezo tube to scanner holder gluing jig
- Epotek H20E silver conducting epoxy
- Varian Torr Seal
- Ethanol Thin the Torr seal with this so its not so viscous. It doesnt take much ethanol to do this. Experiment with the mixture before gluing scanner parts.
- Connector pins for scanner base Jacob says these are homemade Mill-max in BeCu tube. The scanner holder I used already had them installed.

B.2.2 Assembly Steps

Note: All baking steps with copper were made in the vacuum oven under a nitrogen atmosphere with ¡1% oxygen, to prevent oxidizing the copper. When gluing copper with Torr Seal, cure as soon as possible since the uncured form corrodes the metal. EBL lists the Curie temperature of the piezo as 300C, but rather than tempt fate I did not bake the piezo above 80C.

- Install connector pins in the scanner holder base.
- Glue on Z wire into the inner surface of the piezo tube with conducting epoxy. Use Jhinhwans jig to do this. Bake.

- Glue the piezo tube onto the scanner holder. Bend the Z-line a bit before threading through the scanner holder so that the wire is not loose inside the holder. This prevents vibration problems at the tip. Make an even ring of Torr Seal/ethanol at the bottom of the tube. Dont use too much glue, as it will restrict the piezo motion. Put the piezo in the groove on the scanner holder and twirl the piezo in both directions. This twirling evenly spreads the glue around the groove and preserves the cylindrical symmetry, keeping the X-Y deflection the same. Place the macor tip holder unglued onto the top of the tube, and the place Jhinhwans jig over the whole thing. This jig is the key to gluing the piezo on straight. Bake.
- Glue the X-Y lines into the scanner holder grooves. Cut appropriate lengths of #36 bare copper wire and straighten as best as possible. Thread the wires through the holes in the base of the scanner holder. Secure the free ends at the top by taping them to the piezo tube with Teflon tape. The free ends at the bottom can be simply secured by bending them. When the ends are secured, the wire should stay inside the grooves unaided. Now apply Torr Seal/ethanol along the entire length of the grooves, but be careful not get the glue on the piezo tube. Bake. You should be able to glue all four wires at once.
- Glue the X-Y lines onto the piezo electrodes. Cut the wires at the top end to the appropriate length. I left these wires longer than everyone else does. Cut a thin strip of Teflon tape, and tape down the wires to the piezo tube so that the ends of the wires stick out from the tape. Make sure the wires are straight. Add a small dab of conducting epoxy to the wire ends. It doesnt take much since the Teflon tape is holding the wires flat against the electrodes. Bake. You should be able to glue all four wires at once.

- Solder or glue with conducting epoxy the X-Y-Z lines into/onto the appropriate connector pins. Check resistance of resulting connections, as well as X-Y scanner capacitances to Z.

- Build the tip holder. Cut a .130 - .150 length of ceramic tubing using the Dremel tool with a cut-off disk. It might take a few tries to get the Dremel to cut the tube without shattering it. Sand the ends flat. Cut a .150 -.170 length of BeCu tube. Take care not to crush the tube during the cutting process. I did this as follows: I shoved a 0.0135 diameter bare copper wire about 3 into the tube about. Using a fresh razor blade, I carefully cut the tube under the microscope. I cut lightly around the tube several times, going a bit deeper with each cut until the the BeCu tube was severed. This can be done without severing the copper wire thats been shoved inside. Now glue the BeCu inside the ceramic tubing with Torr Seal/ethanol. Leave enough space inside the bottom of the ceramic tube to plug it, and enough exposed BeCu at the top to attach the tip wire. Bake.

- Plug the bottom of the ceramic tube. A couple drawings indicate a small macor plug for this. As far as I know, this plug has never been made. Some people have made this plug from Torr Seal. When I tried Torr Seal, it leaked down into the BeCu tube and clogged it. So next I tried a very short piece of #26 bare copper wire. This kept the BeCu tube clear. However, the fit wasnt very good, being loose. I recommend the next person trying #24 wire (my ceramic tube ID was 0.020). Just make sure the copper is covered by Torr Seal to insulate the ground plane. Bake.

- Paint the ground plane in the sides and bottom of the ceramic tube. Use conducting epoxy for this. Hold the ceramic/BeCu tube assembly by doing the following. Cut 3 length of the .0135 wire that was used to keep the BeCu

from collapsing. Shove this wire into the top of the BeCu tube. Use a fine solder vise to hold the wire so that the ceramic/BeCu tube is inverted. Now paint on the conducting epoxy. I used a tooth pick to do this. Make sure to evenly spread the epoxy layer and that there are no holes in it. Be very careful not to bridge this ground plane to the BeCu tube. Place the solder vise/wire/tube into the oven and bake. When done, measure the resistance between several points on the epoxy layer. The resistance should not exceed 5 ohms.

- Glue the ceramic/BeCu tube into the macor tip holder. Put a fairly thick ring of Torr Seal/ethanol around the ceramic/BeCu tube up a bit from the bottom. Insert the tube into the tip holder so that a bit of conducting epoxy-coated ceramic tube is exposed. Enough needs to be exposed around the entire circumference so that there will be good electrical contact to the next part of the ground plane to be painted on. The tip holder needs to sit upright while the glue cures so that the tubes set as vertical as possible. I put the tip holder on top of the piezo tube/scanner holder, and then put the whole thing in the oven. A better way is to drill a hole of appropriate size into a brass or aluminum block, and use this to hold the tip holder vertically.
- Paint the ground plane onto the top of the macor tip holder. This should be done under the microscope. I used a fine (#36) copper wire wrapped around a toothpick to paint on the conducting epoxy. Bake. When cured, make sure the resistance between the conducting epoxy on the top and bottom of the tip holder is low. Mine was below six ohms all around.
- Glue the tip holder onto the scanner tube. Again, try to use as little glue as possible and spread evenly for the same reasons as in step 3. Use ethanol/Torr seal. Using the microscope and a fine wire wrapped around a toothpick, I

spread a thin, but not too thin layer of glue onto the top of the piezo. Since the glue looked uniform under the scope, I put the macor tip holder onto the tube without the twirling in step 3. Bake. To test the integrity of the joint, I lifted the whole assembly up by the macor tip holder. The joint did not fail.

- The scanner is now ready for an attempt to put it in the sapphire prism. The first attempt will likely fail due to the Torr seal used on the x-y scanner lines. Yuhki used a razor to scrape off the excess glue on my scanner; Jacob has used fine sandpaper.

Dont forget to test the resolution and S/N of spectroscopic mapping before attempting a serious experiment.

GLOSSARY

a_0	Lattice constant the shortest distance between two lattice sites, 97
ARPES	acronym for Angle Resolved Photoemission Spectrocopy. A particle accelerator technique which utilizes high-energy light sources to probe electronic states inside samples, 125
BSCCO	shorthand for $Bi_2Sr_{2-x}Dy_yCa_{1-y+x}Cu_2O_{8+\delta}$, 66
detailed balance	$P_{a\to b} = P_{b\to a}$ where P is probability, 126
DFT	acronym for Discrete Fourier Transform, 170
ECU	Electronic Control Unit, 27
mash	^{3}He/^{4}He mixture used in a dilution refrigerator, 33
Na-CCOC	shorthand for $Ca_{2-x}Na_xCuO_2Cl_2$, 67
PID	a Proportional/Integral/Derivative Feedback Controller, 27

S/N shorthand for signal-to-noise ratio. Quality experiments are characterized by a high S/N and better S/N implies less likelihood of errors due to noise., 130

spin-polarized Characteristic of an STM tip in which atoms/ions near the tip apex have a local net magnetic component due to spin. This can also refer to a ferromagnetic (bulk magnetized) tip. Spin-polarized tips are used to probe magnetic degrees of freedom, 96

STM Scanning tunneling microscope, or scanning tunneling microscopy. An extremely precise real space microscope able to resolve lengths to a fraction of a lattice constant on metallic or quasi-metallic surfaces, 1

supermodulation the incommensurate lattice reconstruction commonly observed in BSCCO which occurs due to the interruptions of nonstoichiometric oxygens near the BiO layer, 100